

NAVAL POSTGRADUATE SCHOOL MONTEREY, CALIFORNIA



19980102 126

THESIS

ELECTROMAGNETIC IMAGING OF AXISYMMETRIC SCATTERERS

by

Daniel J. Wawrzyniak

June 1997

Thesis Advisor:

Michael A. Morgan

Approved for public release; distribution is unlimited.

DTIC QUALITY INSPECTED 4

REPORT DOCUMENTATION PAGE			Form Approved OMB No. 0704-0188	
Public reporting burden for this collection of information is estimated to average 1 hour per response, including the time for reviewing instruction, searching existing data sources, gathering and maintaining the data needed, and completing and reviewing the collection of information. Send comments regarding this burden estimate or any other aspect of this collection of information, including suggestions for reducing this burden, to Washington Headquarters Services, Directorate for Information Operations and Reports, 1215 Jefferson Davis Highway, Suite 1204, Arlington, VA 22202-4302, and to the Office of Management and Budget, Paperwork Reduction Project (0704-0188) Washington DC 20503.				
1. AGENCY USE ONLY (Leave blank)	2. REPORT DATE June 1997	3. REPORT TYPE AND DATES COVERED Master's Thesis		
4. TITLE AND SUBTITLE: ELECTROMAGNETIC IMAGING OF AXISYMMETRIC SCATTERERS		5. FUNDING NUMBERS		
6. AUTHOR(S) Daniel J. Wawrzyniak				
7. PERFORMING ORGANIZATION NAME(S) AND ADDRESS(ES) Naval Postgraduate School Monterey CA 93943-5000		8. PERFORMING ORGANIZATION REPORT NUMBER		
9. SPONSORING/MONITORING AGENCY NAME(S) AND ADDRESS(ES)		10. SPONSORING/MONITORING AGENCY REPORT NUMBER		
11. SUPPLEMENTARY NOTES The views expressed in this thesis are those of the author and do not reflect the official policy or position of the Department of Defense or the U.S. Government.				
12a. DISTRIBUTION/AVAILABILITY STATEMENT Approved for public release; distribution is unlimited.			12b. DISTRIBUTION CODE	
<p>13. ABSTRACT (maximum 200 words)</p> <p>Radar cross-section is a key element of low-observability. In order to reduce the cross-section of a particular platform, it may be necessary to determine the induced source distribution on the platform which produces the scattered electromagnetic radiation. Determining the distribution may be possible using a probe to measure fields on or near the outer surface of the object. However, the act of measuring may indeed influence the currents being measured. An alternate method is to back-propagate measurements made at distances beyond the realm of strong influence on the parameters of interest to construct visualizations of the local on-surface radiation contributions. This has been demonstrated for the case of cylindrical geometry. The theory is extended in this thesis to axisymmetric bodies for the special case of rotationally symmetric fields.</p>				
14. SUBJECT TERMS *Back-propagation, axisymmetric scatterers, finite element method, FEM			15. NUMBER OF PAGES 111	
			16. PRICE CODE	
17. SECURITY CLASSIFICATION OF REPORT Unclassified	18. SECURITY CLASSIFICATION OF THIS PAGE Unclassified	19. SECURITY CLASSIFICATION OF ABSTRACT Unclassified	20. LIMITATION OF ABSTRACT UL	

Approved for public release; distribution is unlimited.

ELECTROMAGNETIC IMAGING OF AXISYMMETRIC SCATTERERS

Daniel J. Wawrzyniak
Major, United States Marine Corps
B.E.E., Villanova University, 1986

Submitted in partial fulfillment
of the requirements for the degree of

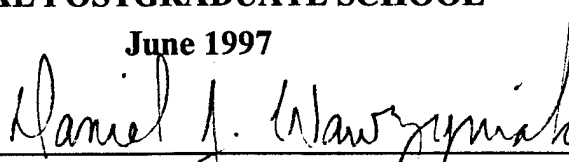
MASTER OF SCIENCE IN ELECTRICAL ENGINEERING

from the

NAVAL POSTGRADUATE SCHOOL

June 1997

Author:

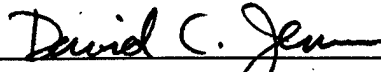


Daniel J. Wawrzyniak

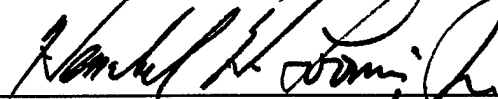
Approved by:



Michael A. Morgan, Thesis Advisor



David C. Jenn, Second Reader



Herschel H. Loomis, Jr., Chairman

Department of Electrical and Computer Engineering

ABSTRACT

Radar cross-section is a key element of low-observability. In order to reduce the cross-section of a particular platform, it may be necessary to determine the induced source distribution on the platform which produces the scattered electromagnetic radiation. Determining the distribution may be possible using a probe to measure fields on or near the outer surface of the object. However, the act of measuring may indeed influence the currents being measured. An alternate method is to back-propagate measurements made at distances beyond the realm of strong influence on the parameters of interest to construct visualizations of the local on-surface radiation contributions. This has been demonstrated for the case of cylindrical geometry. The theory is extended in this thesis to axisymmetric bodies for the special case of rotationally symmetric fields.

TABLE OF CONTENTS

I. INTRODUCTION	1
A. BACKGROUND.....	1
1. The Importance of Stealth.....	1
2. Goals of the Research.....	2
B. SOURCE IMAGING.....	3
1. Acoustics Work with Cylinders	3
2. Extension to Electromagnetics for Cylinder Geometry Case	4
3. Extension to General Non-separable Geometries Using Finite Element Methods....	4
II. GENERATION OF SCATTERED FIELD (MEASURED FIELD).....	7
A. BACKGROUND.....	7
B. SPECIALIZATION TO AXISYMMETRIC FIELD CASES	8
C. OFFSET DIPOLE TO GENERATE SURFACE CURRENT ON SPHERE.....	9
D. FIELD INTEGRATION FOR AXISYMMETRIC CURRENTS	14
E. CENTERED SPHERE INTEGRATION TEST CASES	21
III. BACK PROPAGATION OF SCATTERED FIELD (MEASURED FIELD).....	37
A. BACKGROUND.....	37
B. FINITE ELEMENT FORMULATION FOR AXISYMMETRIC FIELDS.....	37
C. FINITE ELEMENT METHOD LIMITATIONS	39
D. TRANSFER MATRIX FOR CENTERED SPHERE.....	57
IV. ANALYSIS OF RESULTS	71
A. THE INTEGRATION ALGORITHM.....	71
B. FINITE ELEMENT METHOD PROBLEMS.....	72
C. TRANSFER MATRIX	72
V. CONCLUSIONS.....	75
LIST OF REFERENCES.....	77
APPENDIX - MATLAB CODE	79
INITIAL DISTRIBUTION LIST	97

LIST OF FIGURES

Figure 1. Sphere (Meridian Plane) Surrounded by Finite Element Mesh	5
Figure 2. Cone (Meridian Plane) Surrounded by Finite Element Mesh	6
Figure 3. Axisymmetric Field Cases	8
Figure 4. Dipole in Vicinity of Metal Sphere	10
Figure 5. Axisymmetric Body of Revolution	15
Figure 6. Geometry for Explicit Integrations	17
Figure 7. Decomposition of Axisymmetric Body	18
Figure 8. Surface Current Variation Over One Ring	20
Figure 9. Integration Convergence: Case 1a	24
Figure 10. Integration Convergence: Case 1b	25
Figure 11. Integration Convergence: Case 2a	25
Figure 12. Integration Convergence: Case 2b	26
Figure 13. Magnitude Comparison: Case 1a	27
Figure 14. Phase Comparison: Case 1a	27
Figure 15. Magnitude Comparison: Case 1b	28
Figure 16. Phase Comparison: Case 1b	28
Figure 17. Magnitude Comparison: Case 1c	29
Figure 18. Phase Comparison: Case 1c	29
Figure 19. Magnitude Comparison: Case 2a	30
Figure 20. Phase Comparison: Case 2a	30
Figure 21. Magnitude Comparison: Case 2b	31
Figure 22. Phase Comparison: Case 2b	31
Figure 23. Magnitude Comparison: Case 2c	32
Figure 24. Phase Comparison: Case 2c	32
Figure 25. Magnitude Comparison: Case 3a	33
Figure 26. Phase Comparison: Case 3a	33
Figure 27. Magnitude Comparison: Case 3b	34
Figure 28. Phase Comparison: Case 3b	34
Figure 29. Magnitude Comparison: Case 3c	35
Figure 30. Phase Comparison: Case 3c	35
Figure 31. Magnitude Comparison: FEM1a	42
Figure 32. Phase Comparison: FEM1a	42
Figure 33. Magnitude Comparison: FEM1b	43
Figure 34. Phase Comparison: FEM1b	43
Figure 35. Magnitude Comparison: FEM1c	44
Figure 36. Phase Comparison: FEM1c	44
Figure 37. Magnitude Comparison: FEM2a	45
Figure 38. Phase Comparison: FEM2a	45
Figure 39. Magnitude Comparison: FEM2b	46
Figure 40. Phase Comparison: FEM2b	46
Figure 41. Magnitude Comparison: FEM2d	47
Figure 42. Phase Comparison: FEM2d	47

Figure 43. Magnitude Comparison: FEM3a	48
Figure 44. Phase Comparison: FEM3a	48
Figure 45. Magnitude Comparison: FEM3d	49
Figure 46. Phase Comparison: FEM3d	49
Figure 47. Single Mode RMS Error: Case FEM1a	51
Figure 48. Single Mode RMS Error: Case FEM1b	51
Figure 49. Single Mode RMS Error: Case FEM2a	52
Figure 50. Single Mode RMS Error: Case FEM2b	52
Figure 51. Single Mode RMS Error: Case FEM2d	53
Figure 52. Single Mode RMS Error: Case FEM3a	53
Figure 53. Single Mode RMS Error: Case FEM3d	54
Figure 54. Product Solution Parts: Case FEM1b, $n = 4$	55
Figure 55. Product Solution Parts: Case FEM1b, $n = 5$	55
Figure 56. Product Solution Parts: Case FEM2b, $n = 8$	56
Figure 57. Product Solution Parts: Case FEM3b, $n = 16$	56
Figure 58. Resonant Effects at Various Outer Boundary Locations	57
Figure 59. Meridian Plane of Centered Sphere	59
Figure 60. Magnitude Comparison: Case1a	61
Figure 61. Phase Comparison: Case1a	61
Figure 62. Magnitude Comparison: Case1b	62
Figure 63. Phase Comparison: Case1b	62
Figure 64. Magnitude Comparison: Case1c	63
Figure 65. Phase Comparison: Case1c	63
Figure 66. Magnitude Comparison: Case2a	64
Figure 67. Phase Comparison: Case2a	64
Figure 68. Magnitude Comparison: Case2b	65
Figure 69. Phase Comparison: Case2b	65
Figure 70. Magnitude Comparison: Case2c	66
Figure 71. Phase Comparison: Case2c	66
Figure 72. Magnitude Comparison: Case3a	67
Figure 73. Phase Comparison: Case3a	67
Figure 74. Magnitude Comparison: Case3b	68
Figure 75. Phase Comparison: Case3b	68
Figure 76. Magnitude Comparison: Case3c	69
Figure 77. Phase Comparison: Case3c	69

LIST OF TABLES

Table 1. Centered Sphere Integration Results.....	23
Table 2. Centered Sphere Back-Propagation Results: Finite Element Method	40
Table 3. Surface Current Results Using Transfer Matrix	60

I. INTRODUCTION

A. BACKGROUND

1. The Importance of Stealth

The concept of stealth has been around since long before man made his appearance on earth. Nature realized that the survival of its creatures depended on their blending in with the background. Evolution has provided the means for nature's creatures to develop and refine stealth capabilities. It has been during the last fifty or so years that the military forces of the world have taken a keen interest in stealth [1]. The results were displayed by the success of the F117A stealth aircraft during the Persian Gulf War [2, 3, 4].

The success of these aircraft during the Gulf War can be attributed to many factors. By far the most important factor was possession and use of stealth technology. The U.S. military had it and the enemy did not. More importantly, the enemy did not possess the technology to defeat a stealthy airborne platform. That was in 1991, more than six years ago. Since then stealth technology has been ever so slowly let out of its "black box." It is no longer "our own little secret weapon" that only the U.S. military possesses, and there is no guarantee that during the next conflict our adversaries will not possess anti-stealth technology. In fact ultra-wideband radar (UWB) was being developed for detection of stealth platforms before the Gulf War began [5]. In 1994 the United States Air Force admitted that some radars, including some mobile units, could detect the B-2 bomber [6]. And as one would expect, the Russians are also developing their own anti-stealth technology [6]. The bottom line is that if stealth platforms are to remain stealthy, they need to continue to decrease their observability.

The idea of stealth is comprised of several aspects of observability including infrared radiation, optical, acoustic, and radar echo. The objective is to minimize the observables associated with your platform so as to reduce the chances of being detected by the enemy. While current stealth platforms have incorporated reductions in each of these areas, the most emphasis has been placed on reduction of radar signature. This is a consequence of radar being the primary means of detection for the U.S. military, its allies, and its adversaries. That being the case, this thesis attempts to take one small step in the direction of radar cross section reduction by determining the induced source distribution on a body which produces scattered electromagnetic radiation.

2. Goals of the Research

Radar cross-section (RCS) reduction is a key element of low-observability. Current techniques used in determining the RCS of a platform rely on analysis of measurements made in the far-field. Generally these measurements provide a gross picture of the platform's overall RCS as a function of viewing angle. This information enables engineers to then modify the design in an attempt to reduce its RCS. This becomes an iterative process with design modifications leading to measurements which lead to more design modifications.

At the other end of the spectrum, measurements made using a probe on or near the outer surface of the body may influence the quantities being measured. In other words the act of measuring would induce errors into the quantities being sought.

The focus of this study is to more accurately determine the source of scattering on a body. This will be done by evaluating the viability of back-propagating measurements to an axisymmetric body to image the source of scattering on the body. This analysis will

enable more precise location of scattering sources than does gross analysis of the far-field. Once the local scatterers have been identified it is then theoretically possible to remove or reduce them in the overall effort of radar cross-section reduction.

The objective of this study is to investigate the viability of back-propagating electromagnetic field measurements to an axisymmetric body in order to determine the source distribution for radiated power from the body. If this is indeed possible, then the follow-on objectives include determining the range and spatial resolution at which measurements must be made in order to provide meaningful results.

B. SOURCE IMAGING

1. Acoustics Work with Cylinders

A brief history of this subject starts with researchers attempting to determine sources of acoustic noise on a body. It was shown that acoustic intensity could be used to localize sources of sound on structures which radiate to the far field. A new quantity called the supersonic acoustic intensity vector was defined and its application to measurements on plate and cylinder-like structures was demonstrated [7].

“Supersonic intensity is composed only of wave components which radiate to the far field (supersonic), with the non-radiating (subsonic) components eliminated. The normal component of this supersonic intensity vector, measured in the extreme near field or on the surface of the structure, provides an accurate tool for locating regions (“hot spots”) on the structure which radiate to the far field. Furthermore, the supersonic intensity provides an accurate quantification of these source regions, providing a ranking of the strength of the identified source regions as a function of frequency. This identification and ranking provides a powerful new tool in the understanding and control of radiated noise.” [7]

Coupled with the finding that acoustic source regions could be determined through back-propagation was that the results were obtained in two dimensions. Using a cylinder as the scattering body, scattering data measurements were made on an arc of a circle with diameter on the axis of the cylinder [8]. In the spherical (r, θ, ϕ) coordinate system this translates to measurements over θ at a constant ϕ . The restricted case of axisymmetric fields and currents is the next level of difficulty before working with full three dimensional shapes.

2. Extension to Electromagnetics for Cylinder Geometry Case

The discoveries employing supersonic modes to enhance acoustic imaging on cylindrical shells has been translated into the realm of electromagnetics for the case of cylindrical geometry. It was shown that superluminal modes which satisfy $|k_z| < k$ and have faster-than-light axial propagation velocity provide time-average power to the far field. An optimal propagation deconvolution filter was implemented to remove the effects of the subluminal modes during back propagation. [9]

3. Extension to General Non-separable Geometries Using Finite Element Methods

The goal of this research is to extend the concepts developed in previously conducted research to bodies with non-separable geometries. By definition these bodies have shapes that do not lend themselves to explicit rigorous solutions using separable modes, such as cylindrical or spherical wave functions. A finite element method (FEM) is used to relate the conditions at the boundary (measuring region) to conditions on the surface of the body, in this case relating the scattered field to the source current that

generated it. The number of elements used is chosen so that the contour of the body is closely matched. Figure 1 shows a meridian plane of a sphere surrounded by a finite element mesh which connects the surface of the sphere to the arc of a circle with diameter on the axis of the sphere, as previously mentioned. In Figure 2, the body represented is a cone. The more contours on the body, the greater the number of elements required to closely match those contours. Ultimately the accuracy of the solution is determined by the number of elements used.

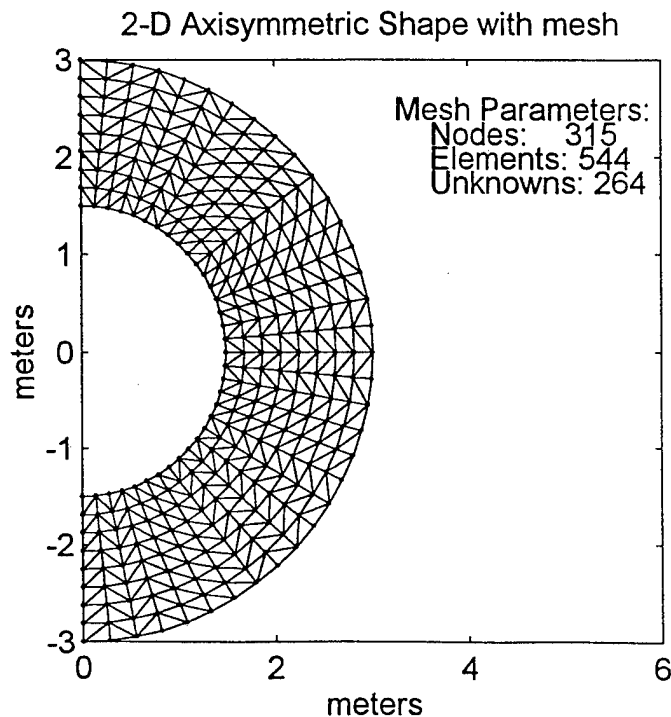


Figure 1. Sphere (Meridian Plane) Surrounded by Finite Element Mesh

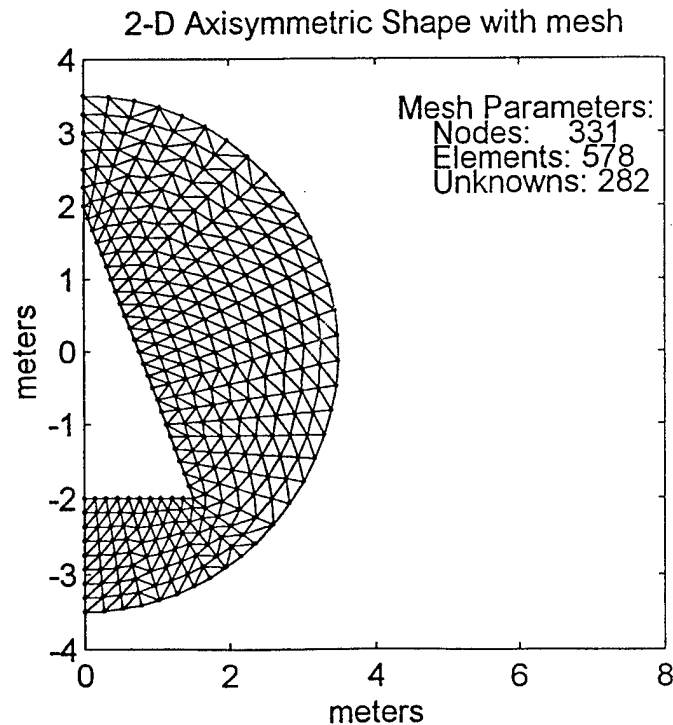


Figure 2. Cone (Meridian Plane) Surrounded by Finite Element Mesh

In the chapters that follow, the source current on the surface of an axisymmetric body is determined through back-propagation of the scattered field it generates. In Chapter II, the scattered field (measured field) is determined through numerical integration of a surface current induced on an axisymmetric body by a locally placed elemental dipole. Chapter III details the back-propagation of the scattered field. Chapter IV provides an analysis of both the numerical integration results and the back-propagation results. Conclusions are presented in Chapter V. An appendix which includes all pertinent computer code is also included to assist in the understanding and continuation of this research.

II. GENERATION OF SCATTERED FIELD (MEASURED FIELD)

A. BACKGROUND

Before the scattered field can be back-propagated it must be measured. To simulate the process and control the sources of error, the measured field is computed to a specified level of accuracy. While reducing potential error associated with field measurements, generating fields leads to an additional hurdle, namely how to generate a scattered field from an arbitrary axisymmetric body. This problem is solved by inducing a surface current on the body and integrating it to find the resulting scattered field. Potential error is introduced as a result of integration accuracy. A sphere is first chosen as the arbitrary axisymmetric body in order to test the accuracy of the general source integration algorithm.

A particular scattered field is generated by placing a radial directed elemental dipole in the vicinity of the metal sphere. The dipole induces a surface current \overline{J}_s on the sphere which in turn generates scattered fields \overline{E}_s and \overline{H}_s . The measured field \overline{H} at some specified distance from the sphere is composed of the field scattered (\overline{H}_s) from the sphere, and the field incident (\overline{H}_i) from the elemental dipole. The 'exact' induced currents and scattered fields can be computed for this test case and used to validate the accuracy of the numerical integration and finite element algorithms. Calculation of the \overline{H} field is considered in Section C. It is generated using the program DIPSPHR2.M found in the Appendix. Field integrations for axisymmetric currents are detailed in Section D and integration results are provided in Section E of this chapter.

B. SPECIALIZATION TO AXISYMMETRIC FIELD CASES

Determining the source distribution on bodies with non-separable geometries is the ultimate objective of research in this area. This thesis reduces the problem from three dimensions to two dimensions by assuming axisymmetric fields generated by axisymmetric currents on a body of revolution. There are two special cases to be considered: the TE_ϕ case in which the \bar{E} field and the surface current are transverse to $\hat{\phi}$, and its dual, the TM_ϕ case in which the \bar{H} field is transverse to $\hat{\phi}$ and the surface current is $\hat{\phi}$ -directed. These cases are depicted in Figure 3.

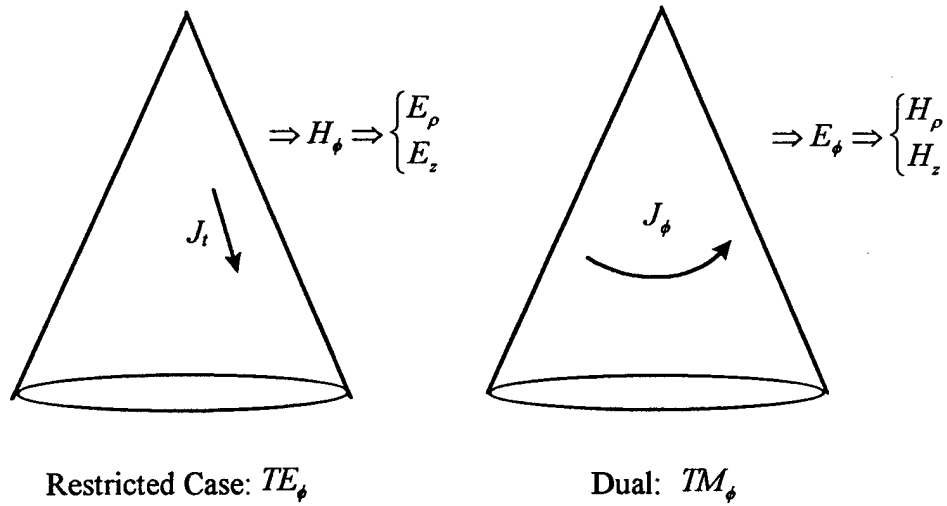


Figure 3. Axisymmetric Field Cases

This thesis will investigate the TE_ϕ case. The fields for this special case are,

$$\bar{H}(\rho, z) = H_\phi(\rho, z)\hat{\phi} \quad (1a)$$

$$\bar{E}(\rho, z) = E_\rho(\rho, z)\hat{\rho} + E_z(\rho, z)\hat{z} \quad (1b)$$

The fields for the dual special case, TM_ϕ , are,

$$\bar{E}(\rho, z) = E_\phi(\rho, z)\hat{\phi} \quad (2a)$$

$$\bar{H}(\rho, z) = H_\rho(\rho, z)\hat{\rho} + H_z(\rho, z)\hat{z} \quad (2b)$$

Maxwell's curl equations are: (with $\omega = 2\pi f$)

$$\nabla \times \bar{H} = j\omega\epsilon\bar{E} + \bar{J} \quad (3a)$$

$$\nabla \times \bar{E} = -j\omega\mu\bar{H} \quad (3b)$$

Using Equation (3a) for the assumed field components in Equation (1) gives

$$j\omega E_\rho = \frac{-1}{\epsilon} \frac{\partial H_\phi}{\partial z} - \frac{1}{\epsilon} J_\rho \quad (4a)$$

$$j\omega E_z = \frac{1}{\epsilon} \frac{1}{\rho} \frac{\partial}{\partial \rho} (\rho H_\phi) - \frac{1}{\epsilon} J_z \quad (4b)$$

These are the generating equations for \bar{E} in terms of H_ϕ and known source current \bar{J} .

Using Equation (3b) for the assumed fields in Equation (2) gives

$$j\omega H_\rho = \frac{1}{\mu} \frac{\partial E_\phi}{\partial z} \quad (5a)$$

$$j\omega H_z = -\frac{1}{\mu} \frac{1}{\rho} \frac{\partial}{\partial \rho} (\rho E_\phi) \quad (5b)$$

These are the generating equations for \bar{H} in terms of E_ϕ .

C. OFFSET DIPOLE TO GENERATE SURFACE CURRENT ON SPHERE

A radial directed dipole located in the vicinity of a metallic sphere is used to generate surface currents on the sphere. These surface currents are then integrated to find the scattered field at a specified distance. The dipole case is also used to test the

integration accuracy by providing a nearly exact scattered field. Figure 4 shows an elemental dipole located in the vicinity of a metal sphere in the spherical coordinate system.

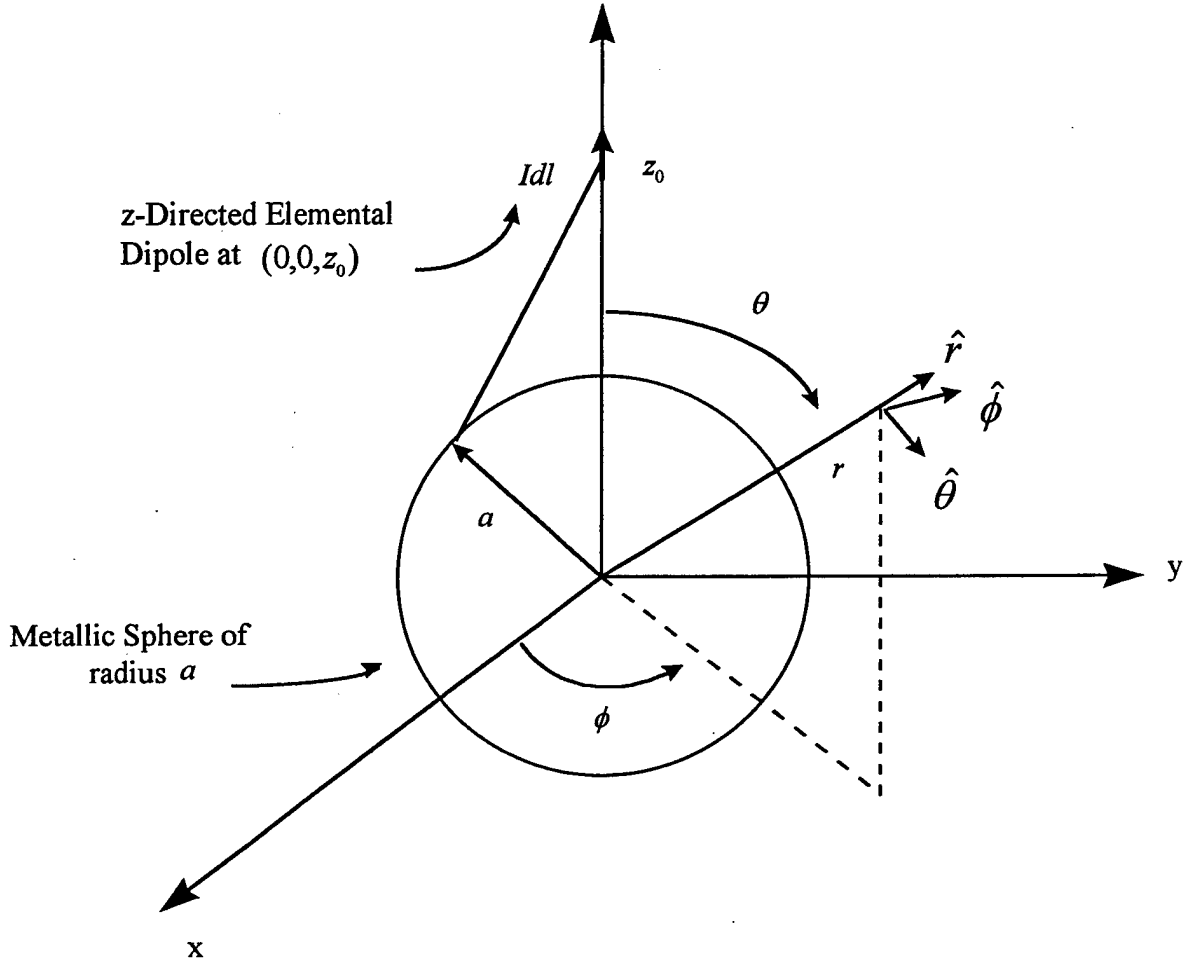


Figure 4. Dipole in Vicinity of Metal Sphere

The procedure for determining the surface current consists of several steps. The \overline{E}_i and \overline{H}_i fields due to the dipole are represented in (r, θ, ϕ) coordinates of the centered sphere. The scattered fields \overline{E}_s and \overline{H}_s due to the induced currents on the sphere are then expanded using spherical harmonic expansions with unknown coefficients. Enforcing

$\hat{r} \times (\overline{E}_i + \overline{E}_s) = 0 \Rightarrow \overline{E}_{\tan} = 0$ on the sphere surface allows solution for the expansion coefficients. Finally $\overline{J}_s = \hat{r} \times (\overline{H}_i + \overline{H}_s)$ is used to find induced surface currents which produce \overline{E}_s and \overline{H}_s fields scattered from the sphere.

An elemental dipole placed at the origin produces the following fields [10]:

$$E_{r_d} = \frac{\eta_0 Idl}{2\pi} \cos \theta_d \left[\frac{1}{r_d^2} - \frac{j}{\beta r_d^3} \right] e^{-j\beta r_d} \quad (6a)$$

$$E_{\theta_d} = \frac{\eta_0 Idl}{4\pi} \sin \theta_d \left[\frac{j\beta}{r_d} + \frac{1}{r_d^2} - \frac{j}{\beta r_d^3} \right] e^{-j\beta r_d} \quad (6b)$$

$$H_{\phi_d} = \frac{Idl}{4\pi} \sin \theta_d \left[\frac{j\beta}{r_d} + \frac{1}{r_d^2} \right] e^{-j\beta r_d} \quad (6c)$$

The position of the dipole must then be translated to the position $z = z_0$. This translation is accomplished using the following transformation formulas:

$$r_d = \sqrt{r^2 + z_0^2 - 2rz_0 \cos \theta} \quad (7a)$$

$$\cos \theta_d = \frac{r \cos \theta - z_0}{r_d} \quad (7b)$$

$$\sin \theta_d = \frac{r \sin \theta}{r_d} \quad (7c)$$

$$E_\theta = E_{\theta_d} \cos(\theta - \theta_d) - E_{r_d} \sin(\theta - \theta_d) \quad (8a)$$

$$E_r = E_{\theta_d} \sin(\theta - \theta_d) + E_{r_d} \cos(\theta - \theta_d) \quad (8b)$$

$$H_\phi = H_{\phi_d} \quad (8c)$$

The transformation formulas in Equations (7) and (8) are then used with Equation (6) to express the fields due to the dipole on the surface of the metal sphere, $E_{\theta i}(a, \theta)$, $E_{r i}(a, \theta)$ and $H_{\phi i}(a, \theta)$. This field will induce a surface current $\bar{J} = J_{\theta}(\theta)\hat{\theta}$ on the surface of the sphere which will, in turn, generate scattered fields $E_{\theta s}$, $E_{r s}$, and $H_{\phi s}$. The tangential \bar{E} field at the sphere surface will exactly cancel the tangential \bar{E} field due to the dipole thus producing a total tangential \bar{E} field of zero

$$E_{\theta s}(a, \theta) = -E_{\theta i}(a, \theta) \quad (9a)$$

The surface current will also satisfy $\bar{J} = \hat{n} \times \bar{H}_{total}$ on the surface:

$$\begin{aligned} \bar{J} &= \hat{r} \times (H_{\phi i} + H_{\phi s})\hat{\phi} \Big|_{r=a} = -(H_{\phi i} + H_{\phi s})\hat{\theta} \Big|_{r=a} (\hat{r} \times \hat{\phi}) = -\hat{\theta} \\ \Rightarrow J_{\theta}(\theta) &= -(H_{\phi i}(a, \theta) + H_{\phi s}(a, \theta)) \end{aligned} \quad (9b)$$

This $J_{\theta}(\theta)$ is what needs to be integrated to find the radiated $H_{\phi s}(r, \theta)$ at locations off the surface of the metal sphere. The result is $H_{\phi s}$ which will be used to compare results of the integration covered in the following section.

Note that although J_{θ} is produced by the total H_{ϕ} on the metal surface, it generates only the scattered field. The scattered field has an $E_{\theta s}$ which exactly cancels out the $E_{\theta i}$ of the incident dipole field on the sphere surface.

To determine the “exact” solution, the scattered fields can be expressed as weighted sums of spherical harmonics [11],

$$E_{\theta s}(r, \theta) = j\eta_0 \sum_{n=1}^{\infty} a_n \frac{\hat{H}_n^{(2)'}(\beta r)}{\beta r} P_n^1(\cos \theta) \quad (10a)$$

$$H_{\phi s}(r, \theta) = \sum_{n=1}^{\infty} \alpha_n \frac{\hat{H}_n^{(2)}(\beta r)}{\beta r} P_n^1(\cos \theta) \quad (10b)$$

where $\hat{H}_n^{(2)}(\beta r) = \hat{J}_n(\beta r) - j\hat{Y}_n(\beta r)$ is the "Riccati" spherical Hankel function of the second kind representing outbound waves. $P_n^1(\cos \theta)$ is the "associated Legendre function" and is the $m = 1$ case of $P_n^m(\cos \theta)$. To numerically solve the problem, truncate the series in Equation (10) and solve for N values of complex α_n . Using

Equation (9a) and defining $D_n = \frac{\hat{H}_n^{(2)}(\beta a)}{\beta a}$ gives

$$j\eta_0 \sum_{n=1}^N \alpha_n D_n P_n^1(\cos \theta) = -E_{\theta i}(\alpha, \theta) \quad (11)$$

The α_n are found by use of orthogonality of the associated Legendre functions,

$P_n^m(\cos \theta)$. For the special case $m = 1$,

$$\int_0^{\pi} P_n^1(\cos \theta) P_l^1(\cos \theta) \sin \theta d\theta = \begin{cases} \frac{2n(n+1)}{2n+1} & l = n \\ 0 & l \neq n \end{cases} \quad (12)$$

We can sift out coefficients:

$$j\eta_0 \alpha_n D_n \frac{2n(n+1)}{2n+1} = - \underbrace{\int_0^{\pi} E_{\theta i}(\alpha, \theta) P_n^1(\cos \theta) \sin \theta d\theta}_{\equiv I_n} \quad (13a)$$

$$\alpha_n = \frac{I_n}{j\eta_0 D_n} \frac{(2n+1)}{2n(n+1)} \quad (13b)$$

The I_n integration can be performed numerically to any accuracy since $E_{\theta i}(\alpha, \theta)$ and

$P_n^1(\cos \theta)$ can be obtained using as many θ -points as desired. Once the α_n are found the

$J_\theta(\theta)$ can be computed at any θ value by use of Equation (9b) with H_ϕ given by Equation (10b).

D. FIELD INTEGRATION FOR AXISYMMETRIC CURRENTS

As noted in the introduction, the first step is to measure the field that will be back-propagated to the surface of the axisymmetric body. For our purposes we will assume an axisymmetric surface current distribution on the body. The "measured" fields will actually be determined through the integration of the surface current. In this context the scattered field is generated through integration rather than through illumination and measurement.

The surface of an arbitrary axisymmetric body of revolution can be defined by use of the generating contour $\rho'(z')$ using the (ρ, ϕ, z) cylindrical coordinate system as shown in Figure 5. Source points on the body are defined by individual (ρ, z) pairs. The field point in space is located at (ρ, ϕ, z) . The axisymmetric surface current distribution is $\overline{J}_s(r') = J_t(\rho', z')\hat{t} + J_\phi(\phi', z')\hat{\phi}$. The unit vectors \hat{t} and $\hat{\phi}$ are tangent to the surface at each point and both J_t and J_ϕ are constant with changing ϕ .

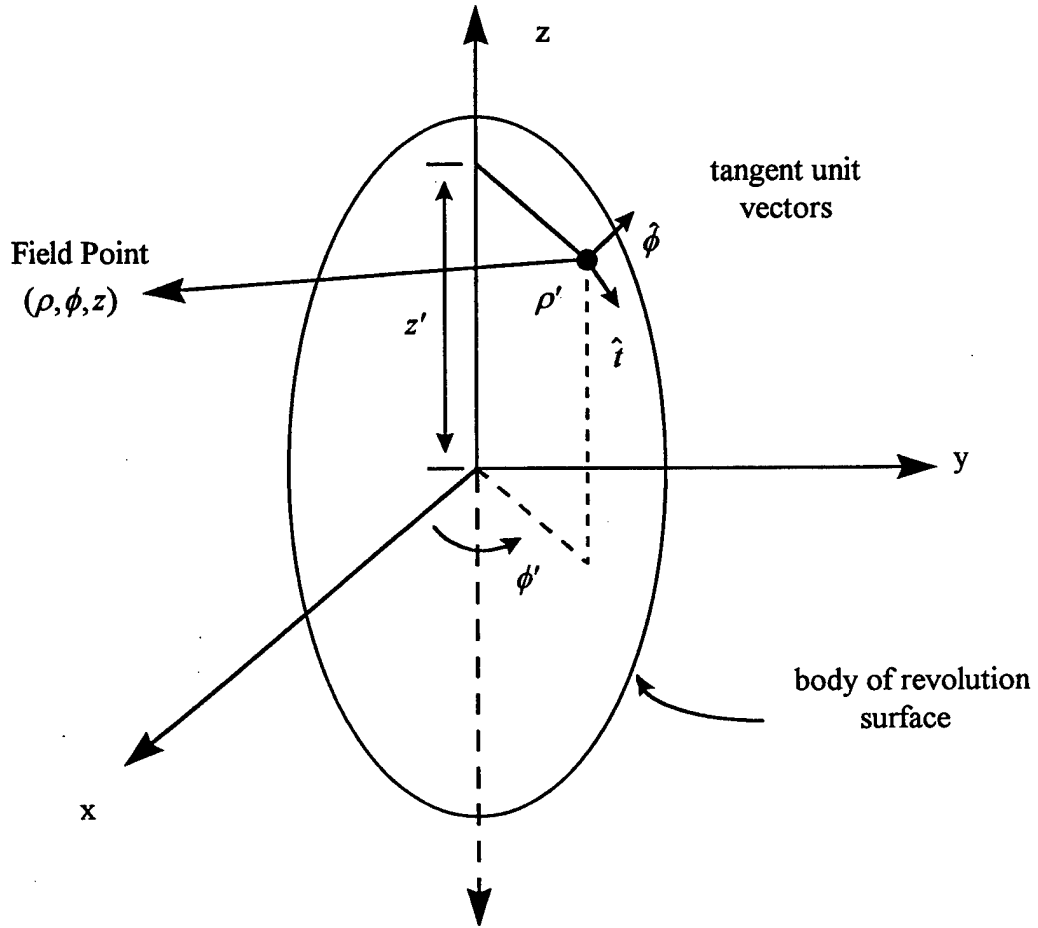


Figure 5. Axisymmetric Body of Revolution

The fields will be numerically evaluated via the vector potential formulation given by [11]:

$$\bar{H}(\bar{r}) = \frac{1}{\mu_0} \nabla \times \bar{A}(\bar{r}) \quad (14a)$$

$$\bar{E} = \frac{1}{j\omega\epsilon_0} \nabla \times \bar{H} = j\omega\bar{A} - \frac{j}{\omega\mu\epsilon} \nabla(\nabla \cdot \bar{A}) \quad (14b)$$

where

$$\bar{A}(\bar{r}) = \frac{\mu_0}{4\pi} \iint_{\text{surface}} \bar{J}_s(\bar{r}') \frac{e^{-j\beta R}}{R} dS' \quad (15)$$

with $\bar{R} = \bar{r} - \bar{r}'$ and $R = |\bar{r} - \bar{r}'|$. For field points and source points with coordinates (ρ, ϕ, z) and (ρ', ϕ', z') the law of cosines gives

$$R = \sqrt{\rho^2 + \rho'^2 - 2\rho\rho' \cos(\phi - \phi') + (z - z')^2} \quad (16)$$

The curl operator in Equation (14a) is taken inside the integral in Equation (15) and note that it only operates on the $e^{-j\beta R}/R$ term (unprimed position in $R = |\bar{r} - \bar{r}'|$)

$$\bar{H}(\bar{r}) = \frac{1}{4\pi} \iint_{\text{surface}} \nabla \left(\frac{e^{-j\beta R}}{R} \right) \times \bar{J}_s(\bar{r}') dS' \quad (17a)$$

where

$$\nabla \left(\frac{e^{-j\beta R}}{R} \right) = -\bar{R} \left(\frac{1 + j\beta R}{R^3} \right) e^{-j\beta R} \quad (17b)$$

Thus the general solution is:

$$\bar{H}(\bar{r}) = \frac{1}{4\pi} \iint_{\text{surface}} [\bar{J}_s(\bar{r}') \times \bar{R}] \left(\frac{1 + j\beta R}{R^3} \right) e^{-j\beta R} dS' \quad (18)$$

The next step is to derive the explicit integrations to be performed. To do so we select \bar{r} in the x-z plane, with $\phi = 0$ as shown in Figure 6. Since \bar{J}_s and the resulting fields so derived are axisymmetric (not functions of ϕ) we lose no generality by doing this. In fact, if we find H_x, H_y and H_z at this field point we note that for other locations where $\phi \neq 0$ the substitutions $H_x \rightarrow H_\rho; H_y \rightarrow H_\phi$ and $H_z \rightarrow H_z$ apply. Also note that

$$\bar{r} = \rho \hat{x} + z \hat{z} \quad (19a)$$

$$\bar{r}' = \rho' \cos \phi' \hat{x} + \rho' \sin \phi' \hat{y} + z' \hat{z} \quad (19b)$$

(19c)

(19d)

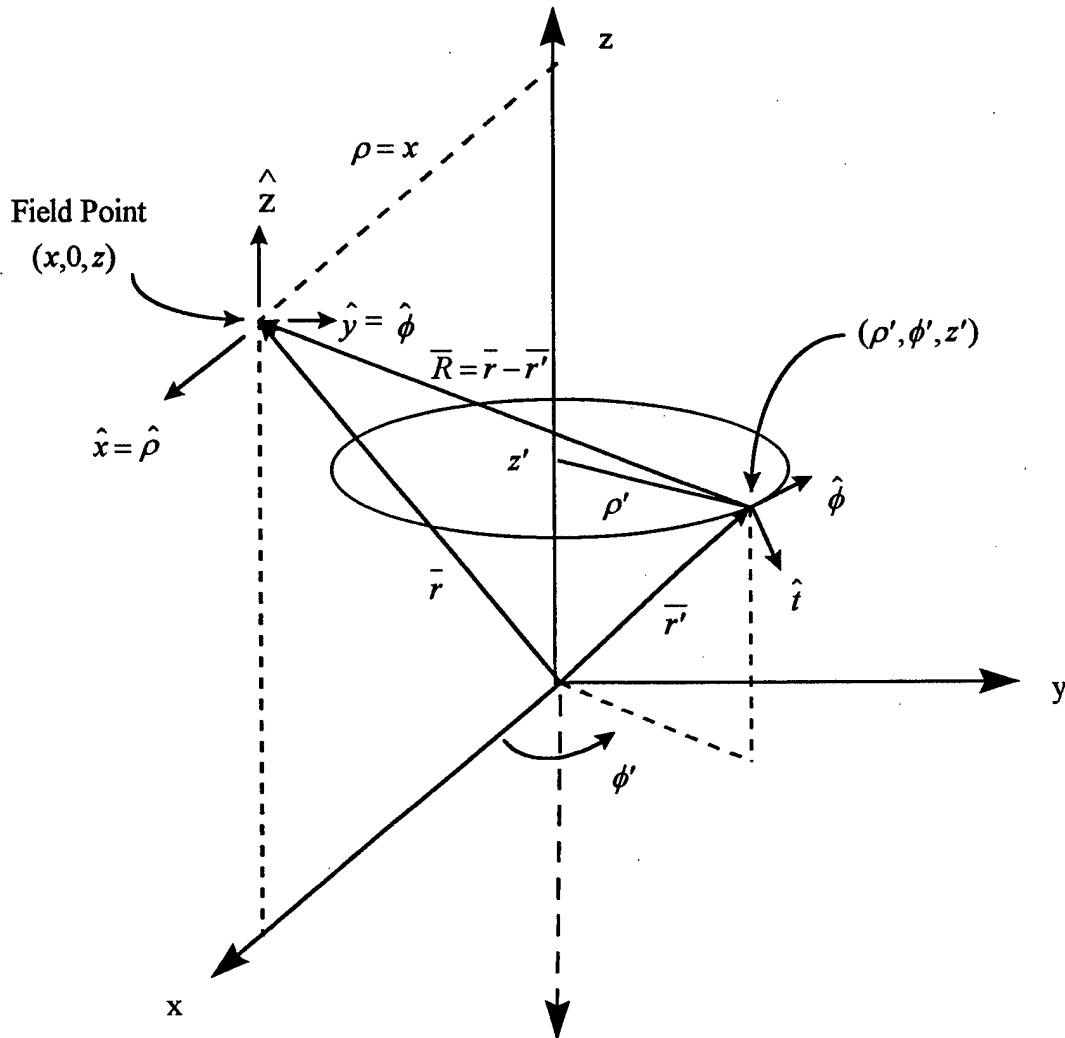


Figure 6. Geometry for Explicit Integrations

The field integrations will be performed numerically by breaking the axisymmetric surface into a large number of flat circular rings as shown in Figure 7a. These rings are stacked to approximate the surface of revolution. Each ring is “flat” in the direction of \hat{t} and curved in the direction of $\hat{\phi}$ as depicted in Figure 7b.

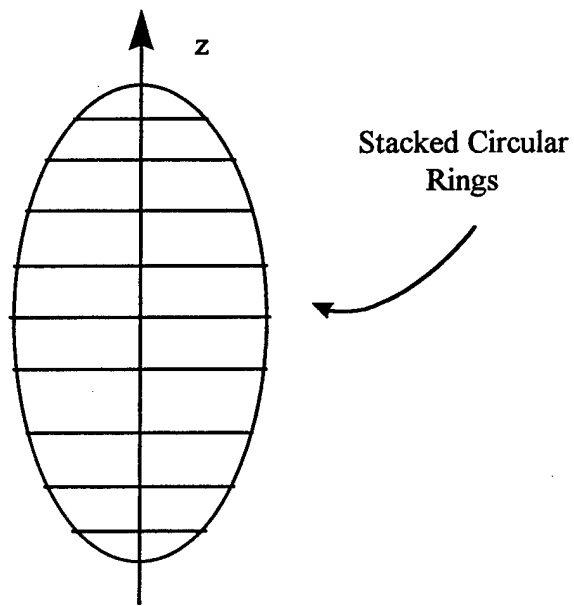


Figure 7a: Stacked Circular Rings form Axisymmetric Body

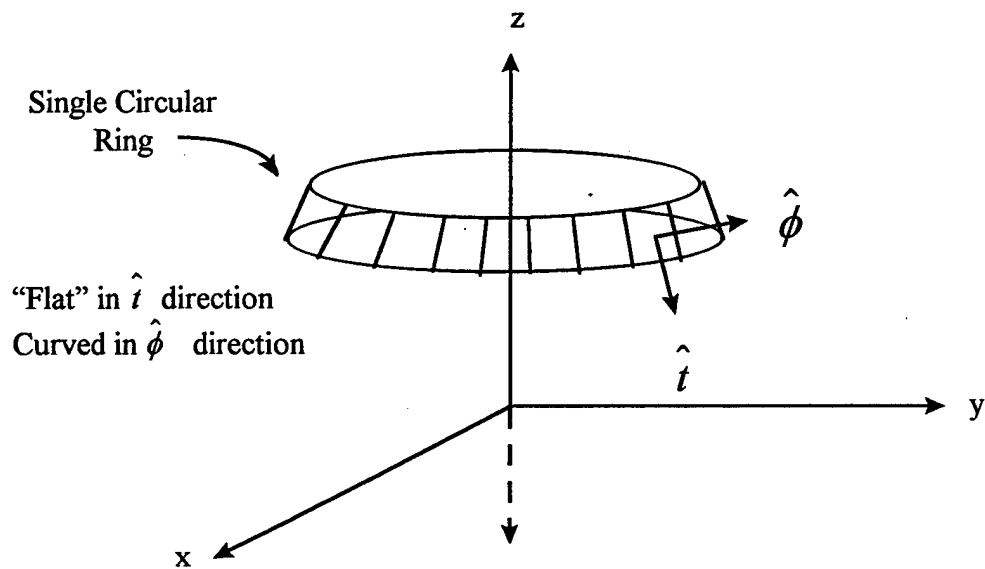


Figure 7b: Single Circular Ring

Figure 7. Decomposition of Axisymmetric Body

Consider now evaluating $\overline{H(\vec{r})}$ in Equation (18) due only to $\overline{J_s(\vec{r}') = J_t(s)\hat{t}}$ over a single ring as in Figure 7b. Over the ring we will approximate $J_t(s)$ as piecewise linear, specified using its values at the top and bottom of the ring, $J_t(s_1)$ and $J_t(s_2)$ via

$$J_t(s) \cong J_t(s_1) \frac{(s-s_1)}{(s_1-s_2)} + J_t(s_2) \frac{(s-s_1)}{(s_2-s_1)} \quad (20)$$

This equation is a straight line interpolating function between known values at s_1 and s_2 .

A single ring is shown in Figure 8a where s is the path length over the ringed surface from the $+z$ axis. The piecewise linear variation of $J_t(s)$ between s_1 and s_2 is shown in

Figure 8b.

To evaluate Equation (18) for $\overline{J_s(\vec{r}') = J_t(s)\hat{t}}$ over a single ring, we note that

$$\hat{t} = \cos\alpha \cos\phi' \hat{x} + \cos\alpha \sin\phi' \hat{y} - \sin\alpha \hat{z} \quad (21)$$

where $\cos\alpha = \hat{t} \cdot \hat{\rho}$ and $-\sin\alpha = \hat{t} \cdot \hat{z}$. After simplifying,

$$\hat{t} \times R = \hat{x}(t_y R_z - t_z R_y) + \hat{y}(t_z R_x - t_x R_z) + \hat{z}(t_x R_y - t_y R_x) \quad (22)$$

and substituting Equation (22) into Equation (18) with restriction to one ring gives,

$$H_x = \frac{1}{4\pi} \int_{s_1}^{s_2} J_t(s) [(z-z') \cos\alpha - \rho' \sin\alpha] F_s(s) \rho' ds \quad (23a)$$

$$H_y = \frac{1}{4\pi} \int_{s_1}^{s_2} J_t(s) \{ [\rho' \sin\alpha - (z-z') \cos\alpha] F_c(s') - \rho \sin\alpha F_1(s) \} \rho' ds \quad (23b)$$

$$H_z = \frac{-1}{4\pi} \int_{s_1}^{s_2} J_t(s) \rho \cos\alpha F_s(s) \rho' ds \quad (23c)$$

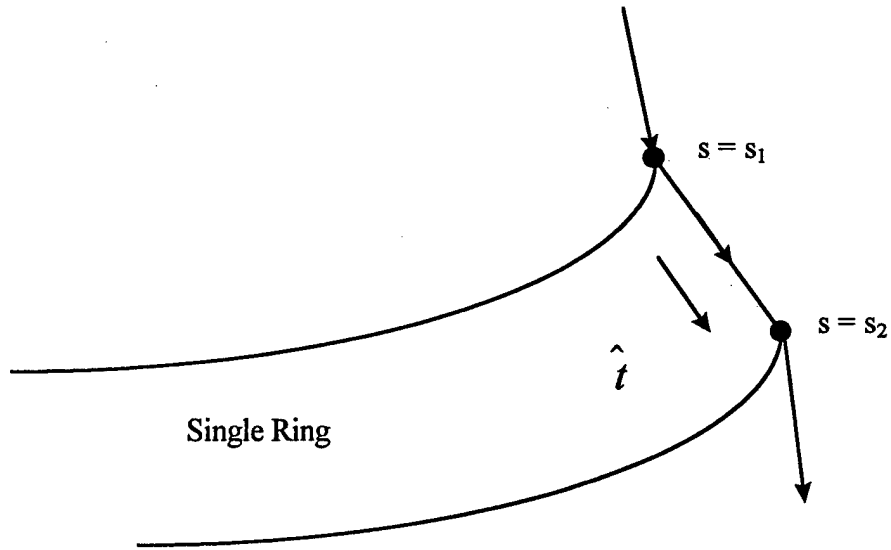


Figure 8a: Single Ring

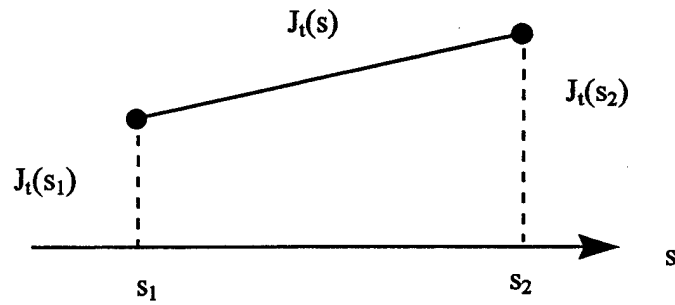


Figure 8b: Piecewise Linear Variation $J_t(s)$

Figure 8. Surface Current Variation Over One Ring

where

$$F_s(s) = \int_{-\pi}^{\pi} \sin \phi' \left(\frac{1 + j\beta R}{R^3} \right) e^{-j\beta R} d\phi' \quad (24a)$$

$$F_c(s) = \int_{-\pi}^{\pi} \cos \phi' \left(\frac{1 + j\beta R}{R^3} \right) e^{-j\beta R} d\phi' \quad (24b)$$

$$F_1(s) = \int_{-\pi}^{\pi} \left(\frac{1 + j\beta R}{R^3} \right) e^{-j\beta R} d\phi' \quad (24c)$$

As we vary ϕ' while holding s constant (e.g. ρ', z' constant), $R(\phi')$ is an even function: $R(-\phi') = R(\phi')$. Therefore $\left(\frac{1 + j\beta R}{R^3} \right) e^{-j\beta R}$ is also an even function of ϕ' .

Since $\sin \phi'$ is an odd function of ϕ' the integrand in Equation (24a) is also odd giving

$F_s(s) \equiv 0$. We are left with only H_y in (10b) since $H_x = H_z = 0$.

Extending this to any position \bar{r} , we have for $\bar{J}_s = J_t(s)\hat{t}$,

$$\bar{H} = H_{\phi}(\bar{r})\hat{\phi} \quad (25a)$$

where

$$H_{\phi} = \frac{1}{4\pi} \int_s J_t(s) \left\{ [\rho' \sin \alpha - (z - z') \cos \alpha] F_c(s) - \rho \sin \alpha F_1(s) \right\} \rho' ds \quad (25b)$$

and

$$F_c(s) = 2 \int_0^{\pi} \cos \phi' \left(\frac{1 + j\beta R}{R^3} \right) e^{-j\beta R} d\phi' \quad (26a)$$

$$F_1(s) = 2 \int_0^{\pi} \left(\frac{1 + j\beta R}{R^3} \right) e^{-j\beta R} d\phi' \quad (26b)$$

E. CENTERED SPHERE INTEGRATION TEST CASES

A centered sphere was chosen as the test case to determine the accuracy of the integration algorithm. The integration algorithm was developed using the trapezoidal rule. Nine cases were tested with sphere sizes ranging from a radius of one wavelength to ten wavelengths. For each sphere size the \bar{H} field was generated at three different locations: 0.2, 1 and 3 wavelengths from the outer surface of the sphere.

The offset distance of the dipole was kept constant for each of the three cases associated with the three different sphere sizes. The number of modes used was determined by the following:

$$N = \text{integer}(2ka + 2), \quad (27)$$

where k is the wave number ($2\pi/\lambda$) and a is the sphere radius. In each of the nine cases the frequency of operation was 300MHz. The RMS error was determined by comparing the \overline{H} field determined through integration to the \overline{H} field exact solution found using the procedure developed in Section II.C. Each of the cases was tested with increasingly fine segmentation in θ and ϕ on the sphere surface until the RMS error was in the neighborhood of one percent. In order to achieve the desired integration accuracy, the number of integration points on the body was increased. This relates to the spatial resolution required when measuring the \overline{H} field in order to achieve acceptable results when back propagating that field. As the number of integration points on the body increases, the measured \overline{H} field becomes more accurate. The more accurate the measured field, the better the surface current on the sphere can be resolved. The test cases summarized in Table 1 are chosen based solely on the RMS error associated with each being in the neighborhood of one percent.

The results shown in Table 1 indicate the RMS error for source integrated H_ϕ observed at the "field distance" radius. The RMS error is a function of the number of surface points at which the surface current was integrated. Figures 9 through 12 show how the integration results converge for several of the cases shown in Table 1. For the

CENTERED SPHERE INTEGRATION RESULTS							
Case	Sphere Radius (λ)	Field Distance (λ)	ϕ Segments	θ Segments	Dipole Offset (λ)	Modes	H_p RMS Error (%)
1a	1	1.2	21	21	5	14	1.1490
1b	1	2	21	21	5	14	1.1620
1c	1	4	21	21	5	14	1.1510
2a	5	5.2	78	78	9	64	1.0310
2b	5	6	78	78	9	64	0.1220
2c	5	8	78	78	9	64	0.1250
3a	10	10.2	157	157	14	128	0.8268
3b	10	11	157	157	14	128	0.0456
3c	10	13	157	157	14	128	0.0459

Table 1. Centered Sphere Integration Results

cases in Table 1, the number of ϕ and θ segments is based on the radius of the sphere. However, the number of ϕ segments remains constant as the radius of each ring (see Figure 7) decreases near both poles of the sphere. This finer ϕ segmentation gives increasingly narrower patches of surface area over which the integration is performed. Consequently, the RMS error does not appear to decrease significantly as the number of ϕ segments is increased. This is a result of the increased ϕ segmentation that is "built in"

as the radius of the rings decrease. An increase in RMS error is observed for the decreased field distance from the sphere in Cases 2a and 3a. Since the field distance is only 0.2λ from the sphere surface in these cases, the large relative contribution and rapid variation of inverse distance terms in the integrand of Equation (18) for surface points closest to the field point require increasingly fine segmentation for accurate numerical integration.

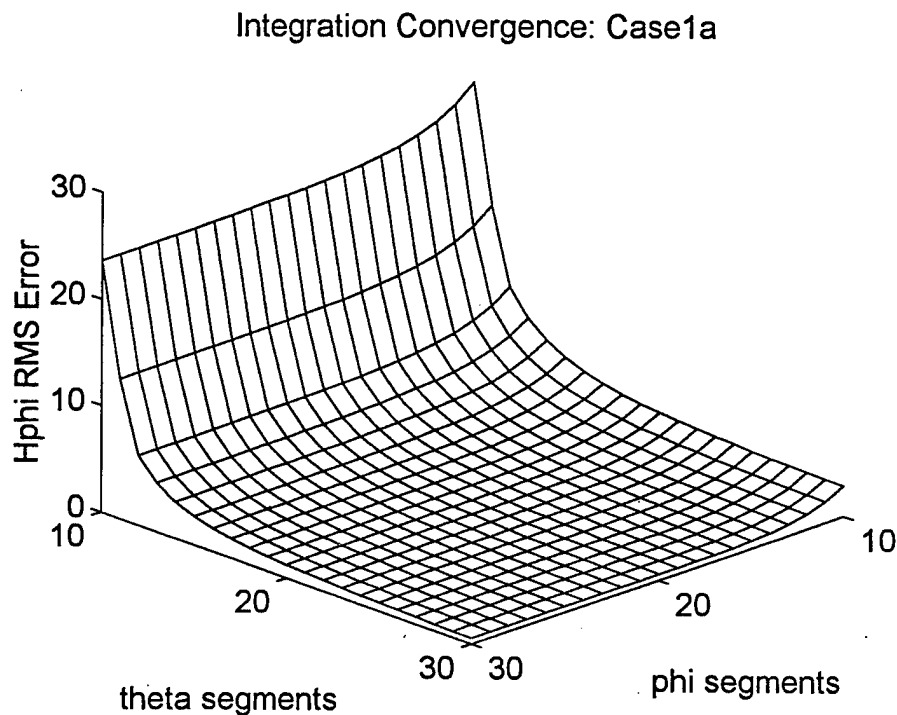


Figure 9. Integration Convergence: Case1a

Integration Convergence: Case1b

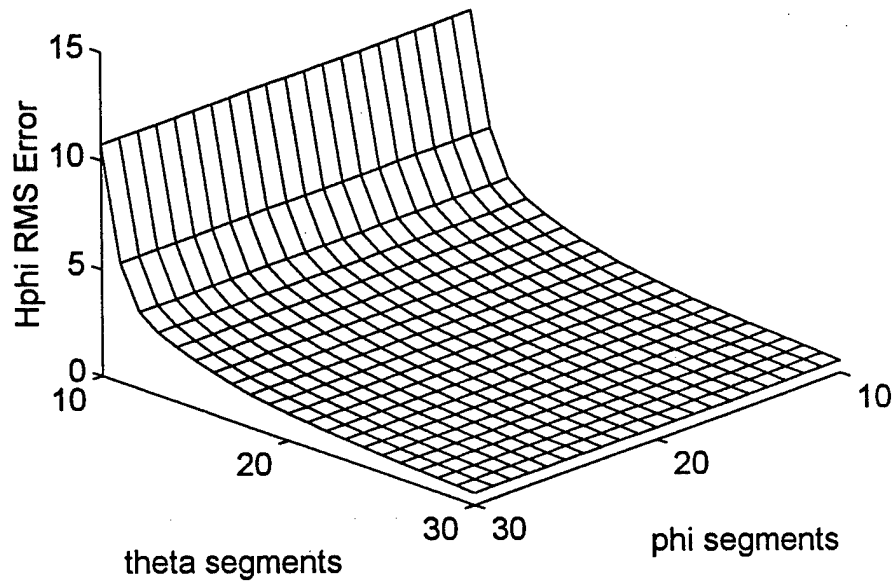


Figure 10. Integration Convergence: Case 1b

Integration Convergence: Case2a

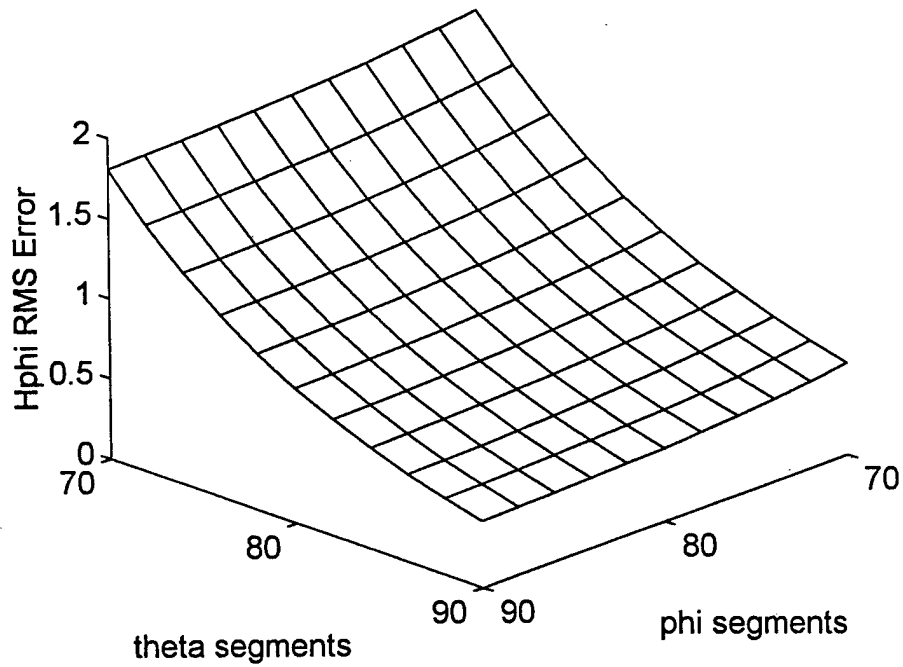


Figure 11. Integration Convergence: Case 2a

Integration Convergence: Case2b

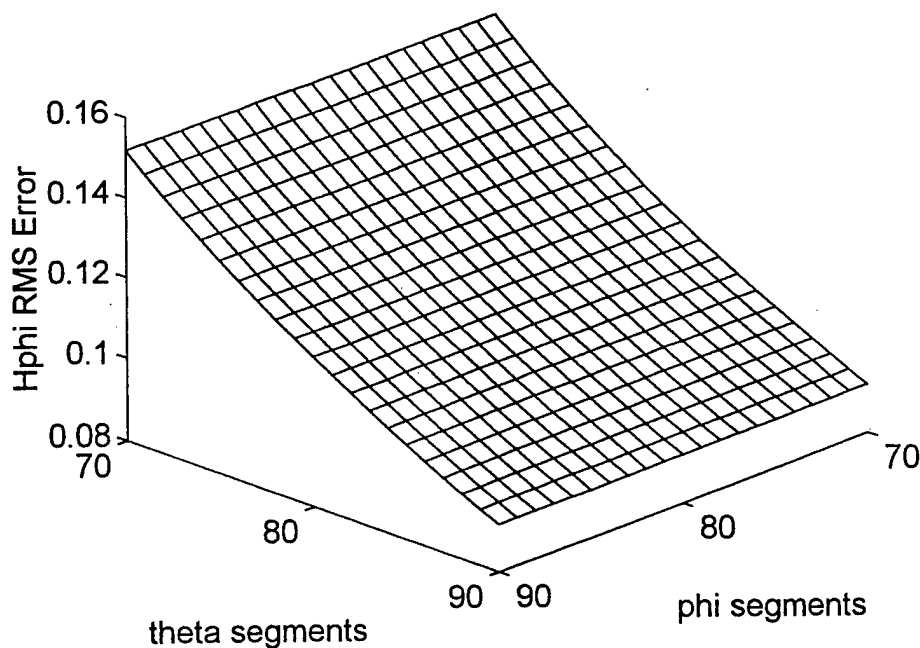


Figure 12. Integration Convergence: Case 2b

The magnitude and phase of the \bar{H} field at the measured distance are presented in Figures 13 through 30. These figures help to tell the complete story of the computed \bar{H} field. In each figure the “exact” quantity computed via series solution is depicted by a line and the “measured” quantity is depicted by dots. Note that in both the magnitude and the phase plots the measured quantity closely matches the exact quantity. These results indicate that the integration produces an \bar{H} field with minimal error. This knowledge will help isolate the source of error that may present itself due to the back-propagation process, which will be described in Chapter III.

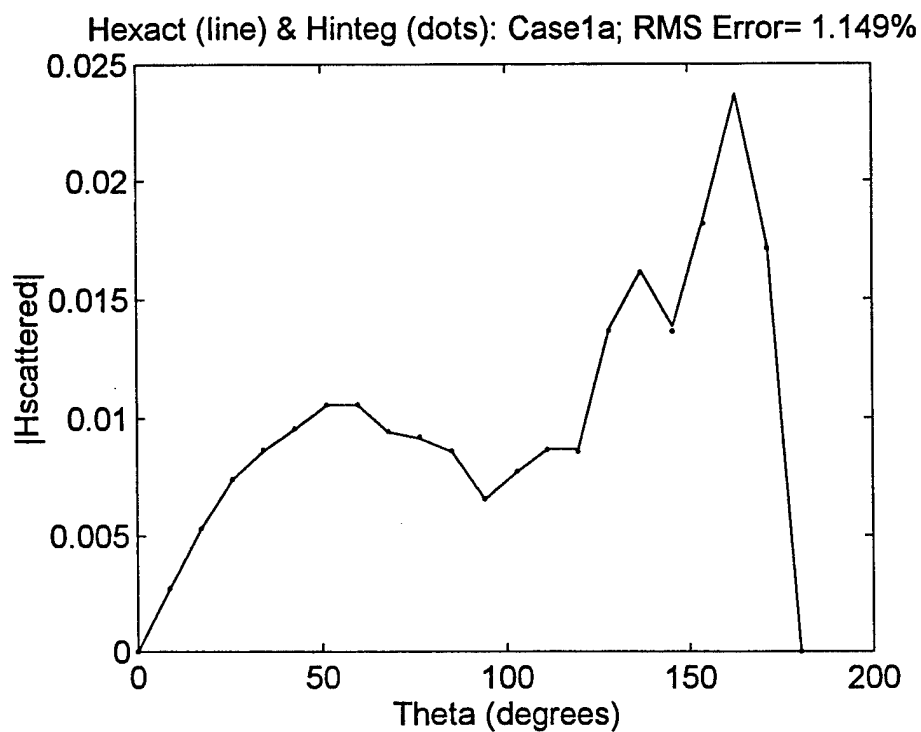


Figure 13. Magnitude Comparison: Case 1a

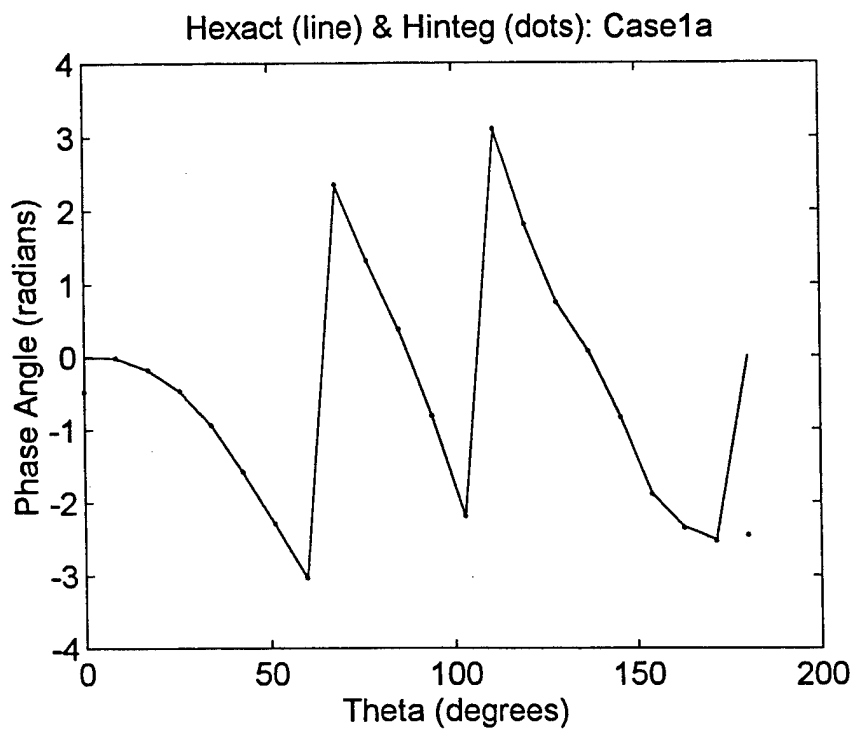


Figure 14. Phase Comparison: Case 1a

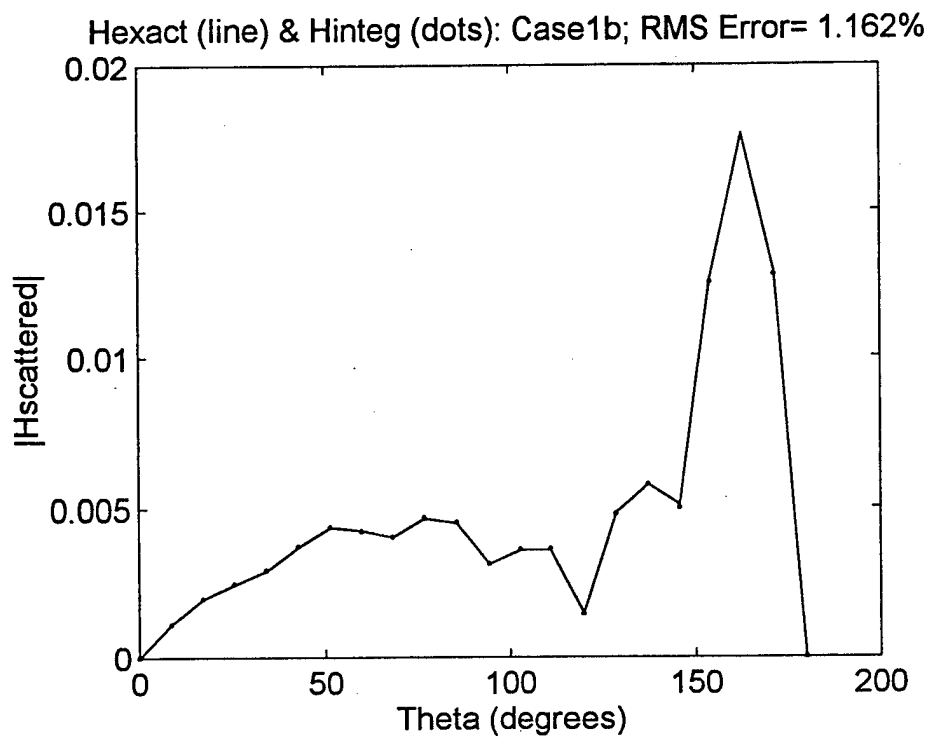


Figure 15. Magnitude Comparison: Case 1b

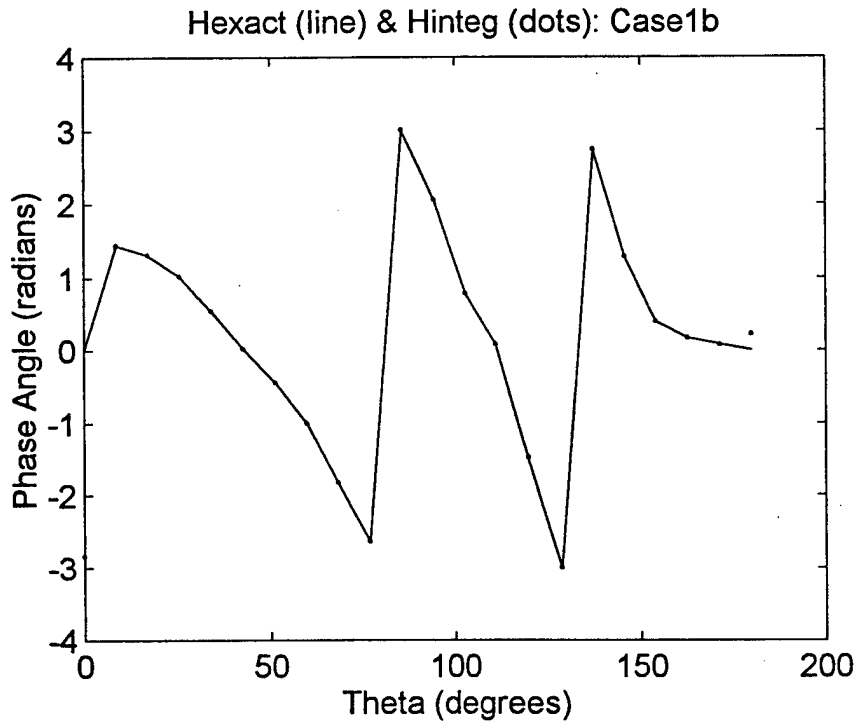


Figure 16. Phase Comparison: Case 1b

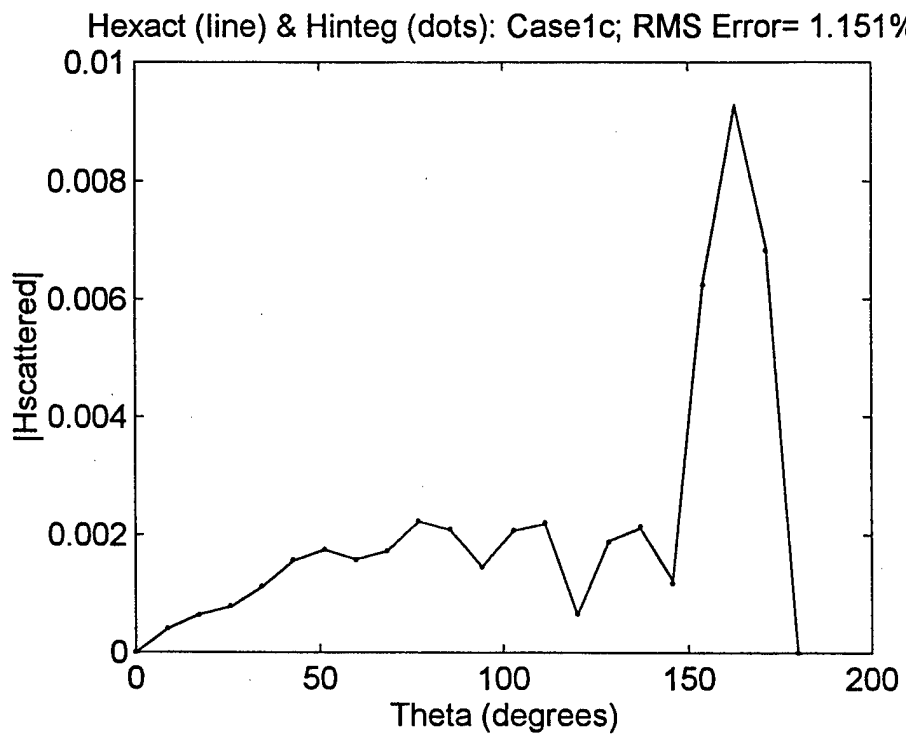


Figure 17. Magnitude Comparison: Case 1c

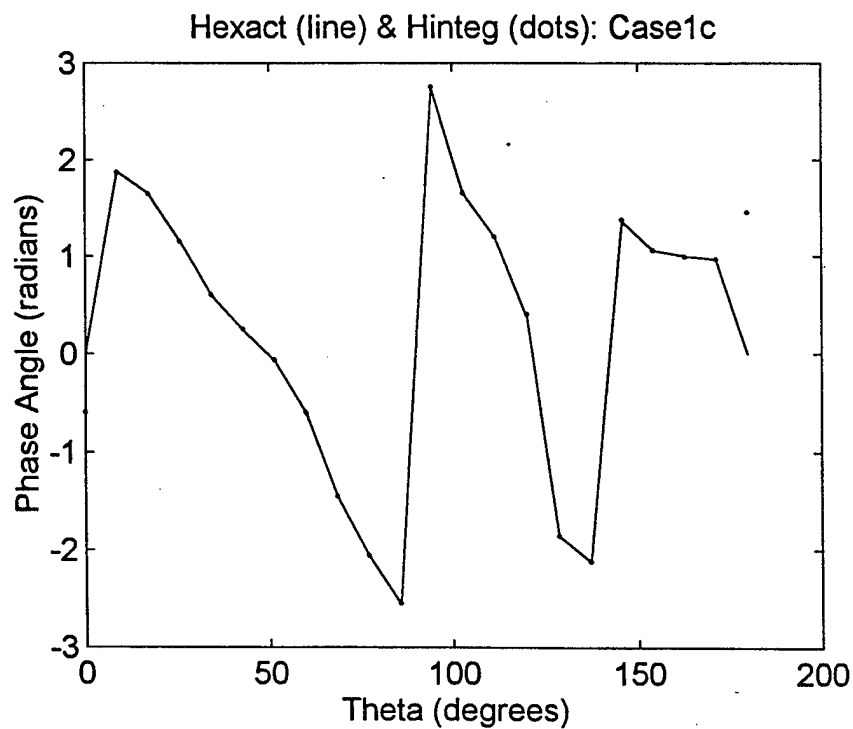


Figure 18. Phase Comparison: Case 1c

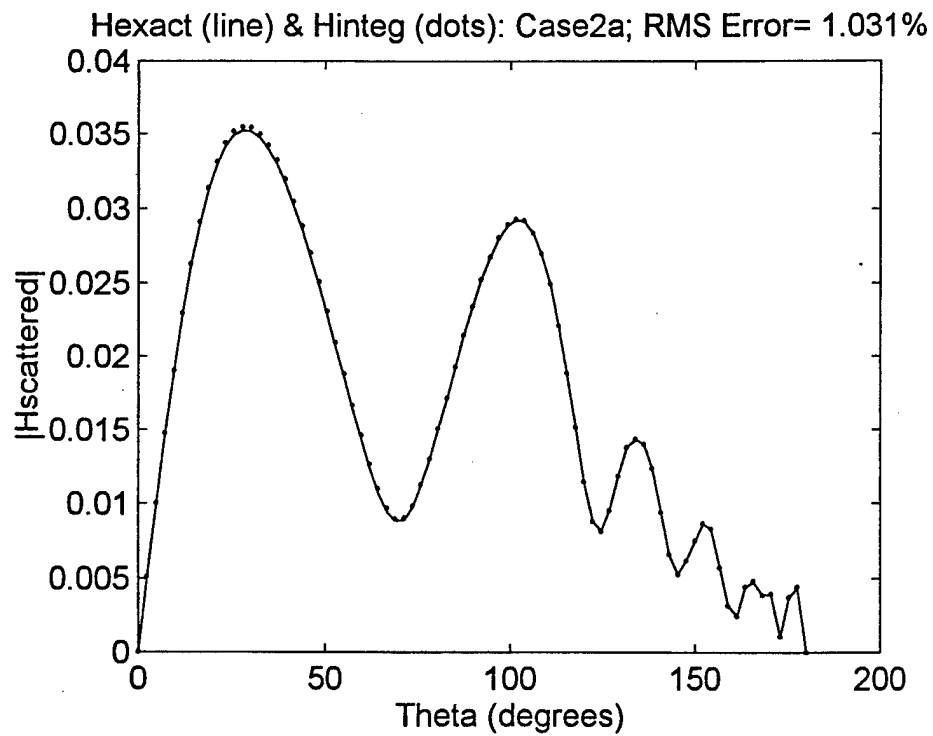


Figure 19. Magnitude Comparison: Case 2a

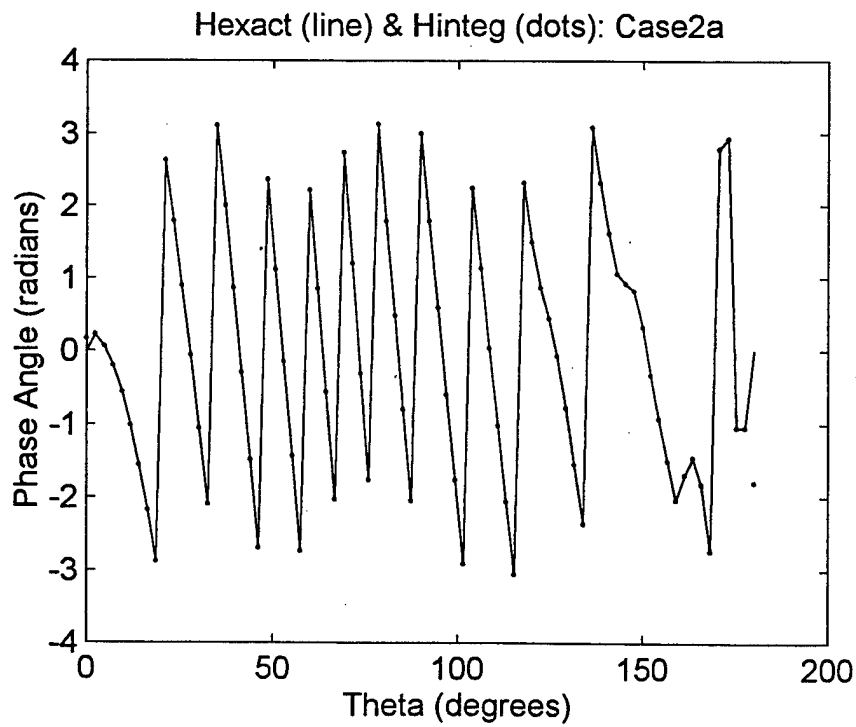


Figure 20. Phase Comparison: Case 2a

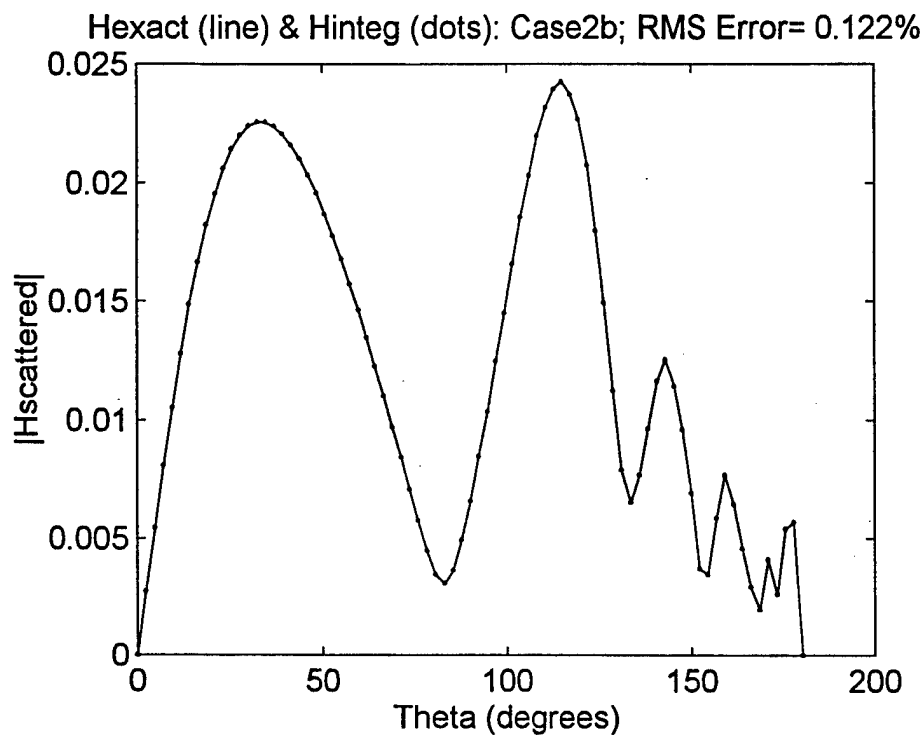


Figure 21. Magnitude Comparison: Case 2b

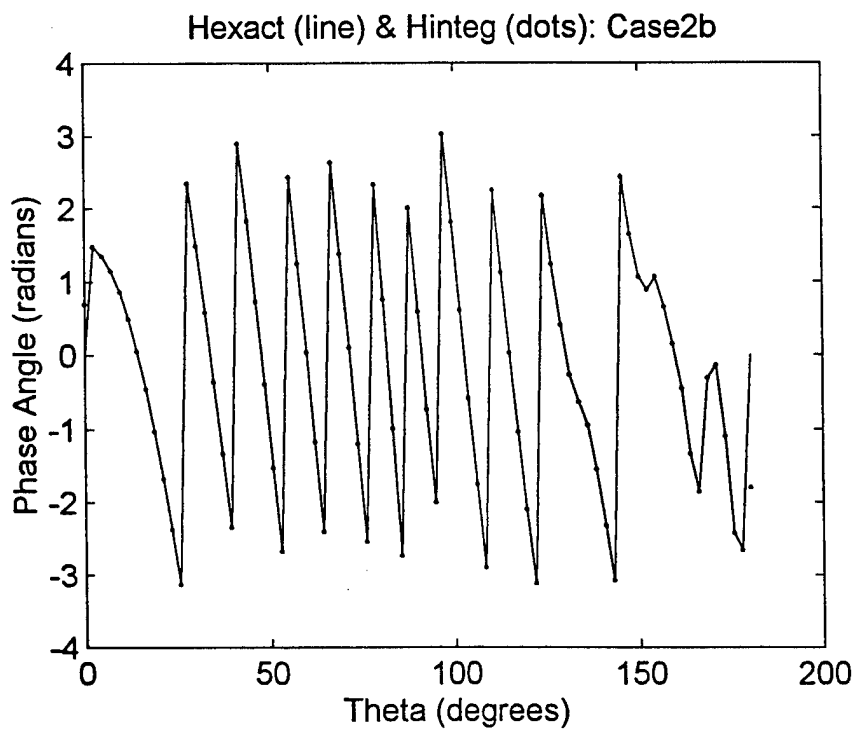


Figure 22. Phase Comparison: Case 2b

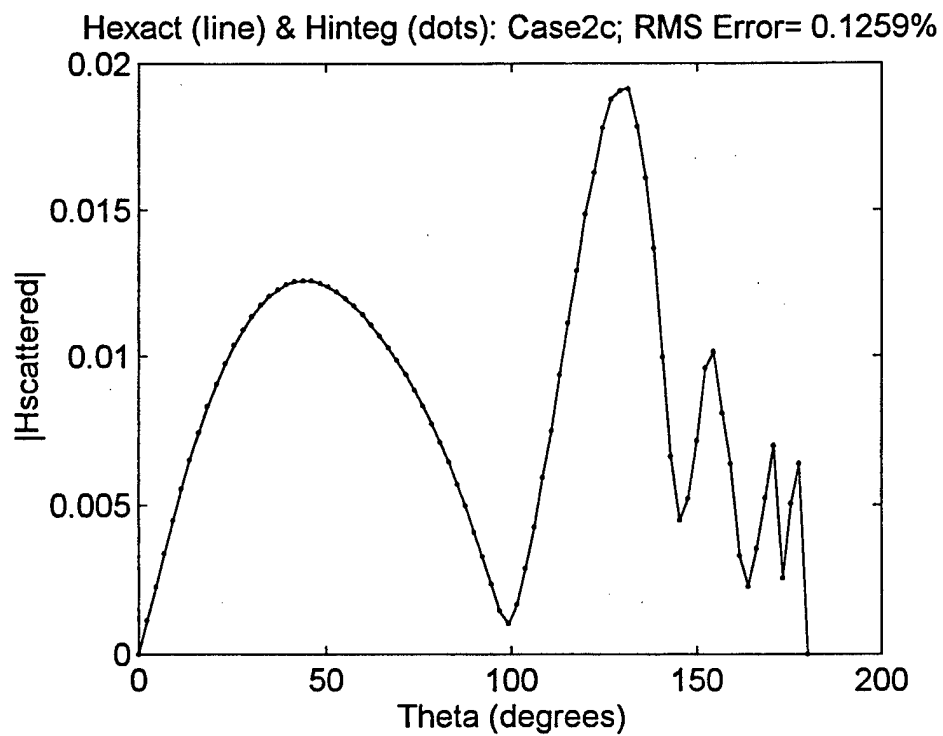


Figure 23. Magnitude Comparison: Case 2c

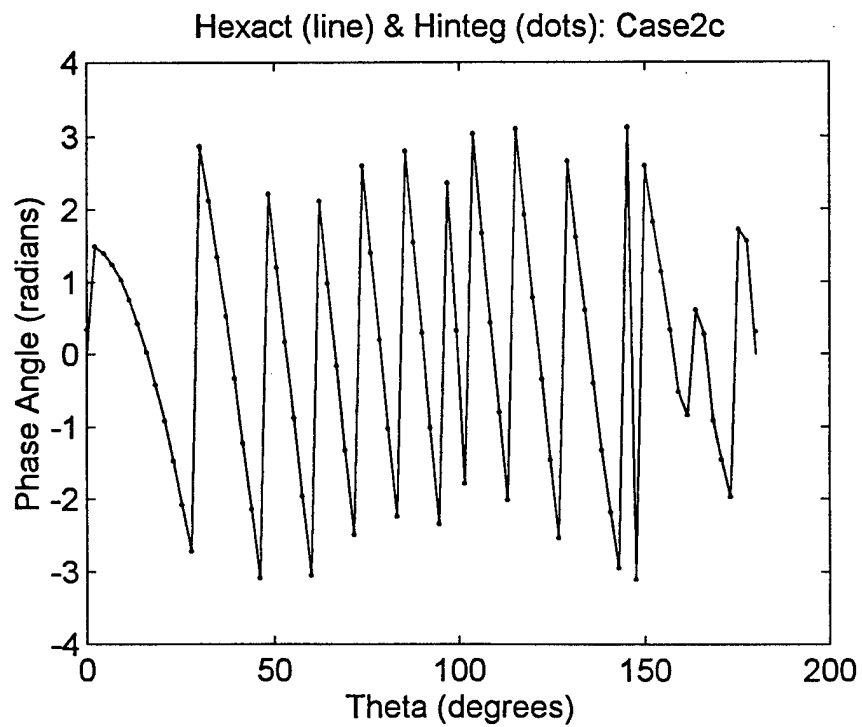


Figure 24. Phase Comparison: Case 2c

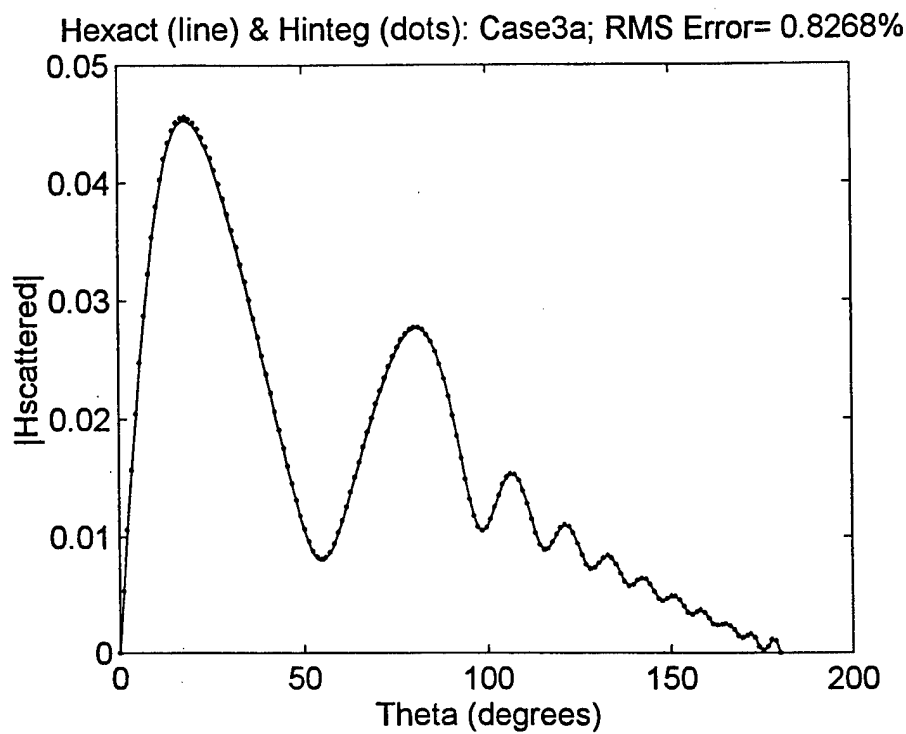


Figure 25. Magnitude Comparison: Case 3a

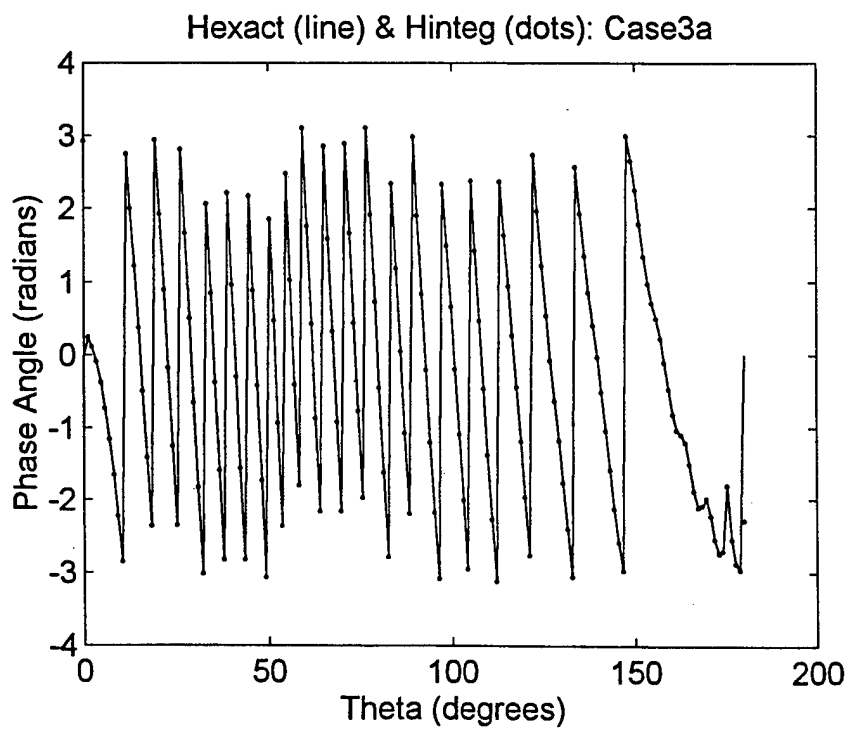


Figure 26. Phase Comparison: Case 3a

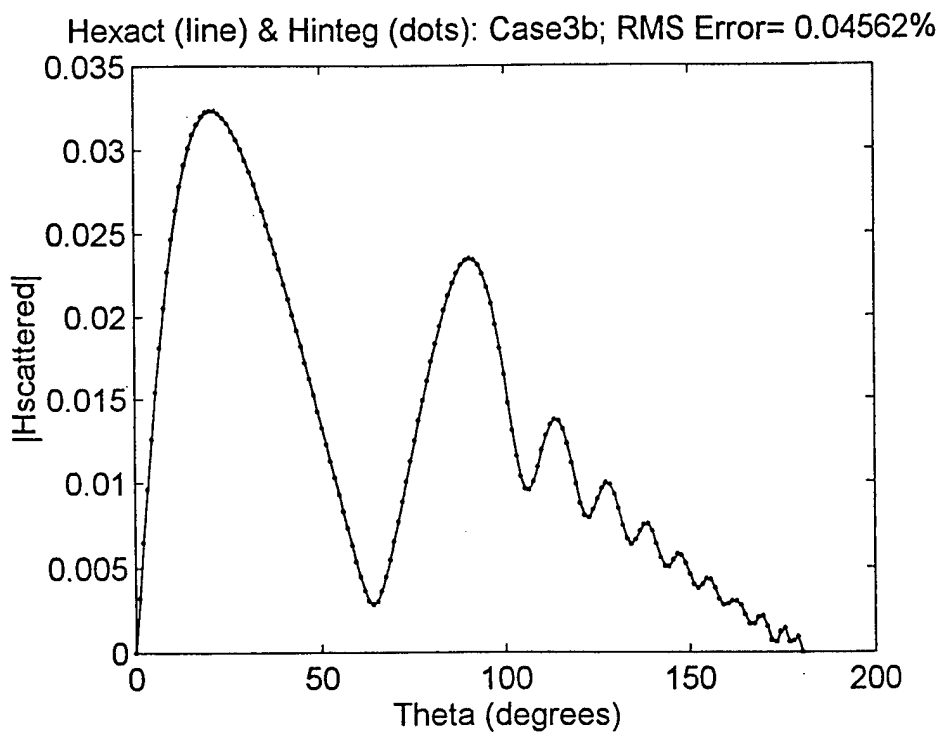


Figure 27. Magnitude Comparison: Case 3b

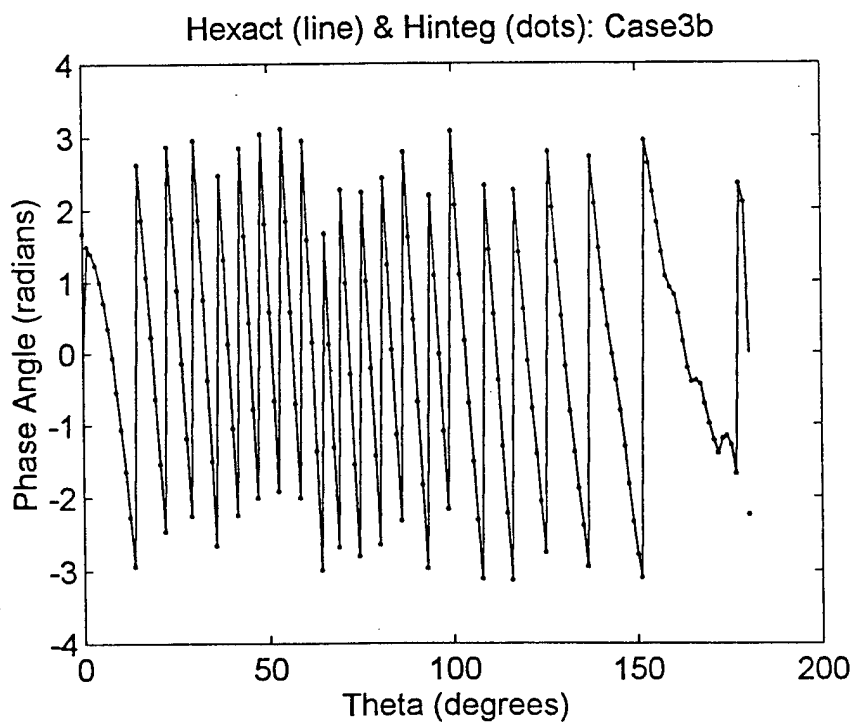


Figure 28. Phase Comparison: Case 3b

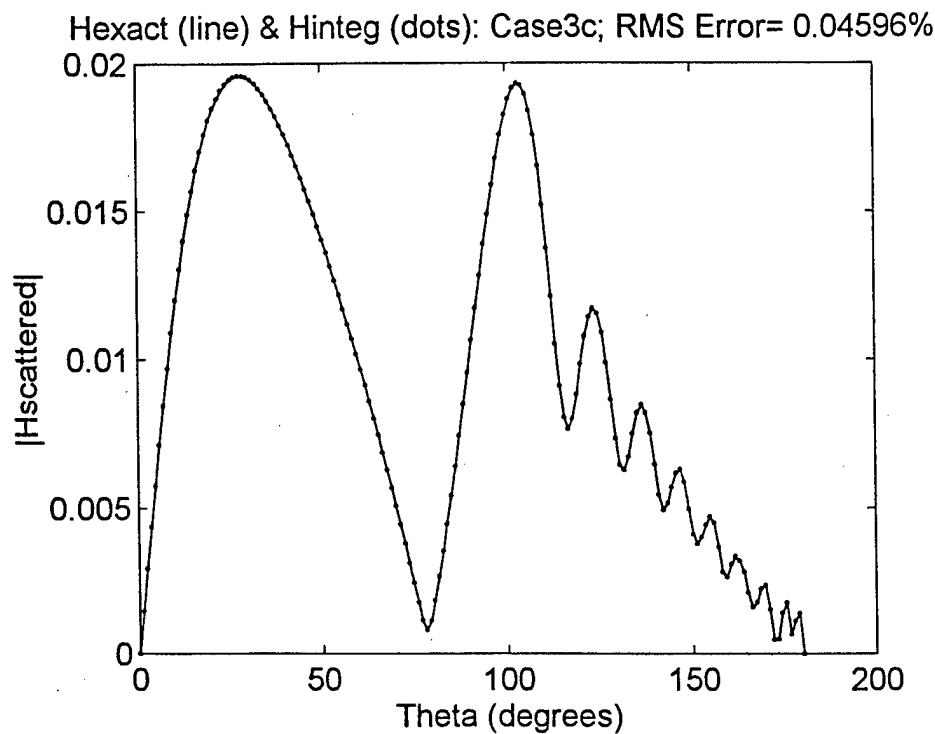


Figure 29. Magnitude Comparison: Case 3c

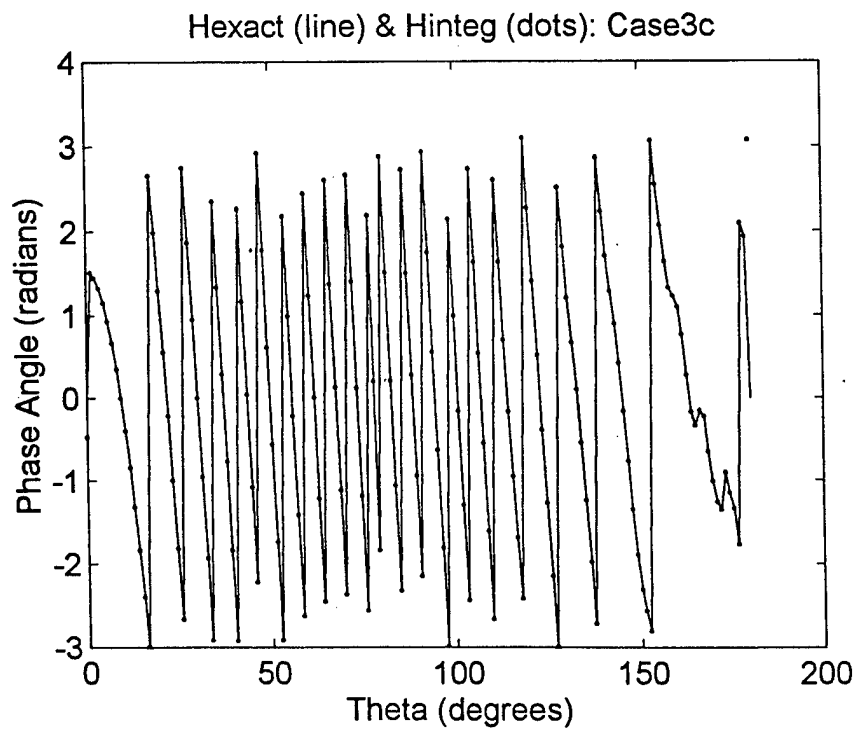


Figure 30. Phase Comparison: Case 3c

III. BACK PROPAGATION OF SCATTERED FIELD (MEASURED FIELD)

A. BACKGROUND

A finite element method is used to back-propagate the measured field to the surface of the sphere. The measured fields that are back-propagated are those determined in Chapter II and summarized in Table 1. Once the measured field is back-propagated, the surface current is determined using Equation (9b). The surface current due to back-propagation ($\bar{J}_{\theta_{back}}$) is compared to the original surface current ($\bar{J}_{\theta_{exact}}$) due to the elemental dipole which is computed using a spherical harmonic series, per Section II.C. The following section describes the finite element formulation.

B. FINITE ELEMENT FORMULATION FOR AXISYMMETRIC FIELDS

For the special case being considered, with no ϕ variation in materials or sources, and $J_\phi = 0$, the fields are derived in Section II.B., results of which are repeated here for convenience,

$$\bar{H}(\rho, z) = H_\phi(\rho, z)\hat{\phi} \quad (28a)$$

$$\bar{E}(\rho, z) = E_\rho(\rho, z)\hat{\rho} + E_z(\rho, z)\hat{z} \quad (28b)$$

Maxwell's curl equations are: (with $\omega = 2\pi f$)

$$\nabla \times \bar{H} = j\omega\epsilon\bar{E} + \bar{J} \quad (29a)$$

$$\nabla \times \bar{E} = -j\omega\mu\bar{H} \quad (29b)$$

Using Equation (29a) for assumed fields in Equation (28) gives

$$j\omega E_\rho = \frac{-1}{\varepsilon} \frac{\partial H_\phi}{\partial z} - \frac{1}{\varepsilon} J_\rho \quad (30a)$$

$$j\omega E_z = \frac{1}{\varepsilon} \frac{1}{\rho} \frac{\partial}{\partial \rho} (\rho H_\phi) - \frac{1}{\varepsilon} J_z \quad (30b)$$

These are the generating equations for \bar{E} in terms of H_ϕ and known source current \bar{J} . In this case Equation (29b) simplifies to:

$$j\omega(\nabla \times \bar{E}) \cdot \hat{\phi} = j\omega \left[\frac{\partial E_\rho}{\partial z} - \frac{\partial E_z}{\partial \rho} \right] = \omega^2 \mu H_\phi \quad (31)$$

Substituting the \bar{E} fields from Equation (30) into Equation (31) gives the partial differential equation (PDE) satisfied by H_ϕ :

$$\frac{\partial}{\partial \rho} \left[\frac{1}{\varepsilon \rho} \frac{\partial}{\partial \rho} (\rho H_\phi) \right] + \frac{\partial}{\partial z} \left[\frac{1}{\varepsilon} \frac{\partial H_\phi}{\partial z} \right] + \omega^2 \mu H_\phi = \frac{\partial}{\partial \rho} \left(\frac{1}{\varepsilon} J_z \right) - \frac{\partial}{\partial z} \left(\frac{1}{\varepsilon} J_\rho \right) \quad (32)$$

where $\varepsilon = \varepsilon(\rho, z)$ is allowed to be inhomogeneous.

The PDE in Equation (32) will be numerically solved using the finite element method (FEM), where H_ϕ is approximated with electrically small triangular element regions in the (ρ, z) plane. [12]

A variational Euler-Lagrange algorithm is used to implement the finite element method. This algorithm replaces the solution of the PDE in Equation (32) with finding the stationary point in complex function space of a quadratic (in H_ϕ) functional. We first expand the field using pyramidal basis functions, $u_n(\rho, z)$, defined for each node in the mesh and having support of the surrounding triangular elements,

$$H_{\phi}(\rho, z) = \sum_{n=1}^N h_n u_n(\rho, z) \quad (33)$$

and then substitute Equation (33) into the functional. The stationary solution is found by differentiating with respect to the unknown values of H_{\bullet} , located at the m-th nodes, to yield the linear system

$$\sum_{n=1}^N h_n \iint_{\text{overlapping elements}} \frac{1}{\rho} \nabla(\rho u_m) \cdot \nabla(\rho u_n) - k^2 \rho u_m u_n d\rho dz = 0 \quad (34)$$

Defining the double integrals indexed on m, n as $T(m, n)$, the linear system in Equation (34) can be rewritten as,

$$\sum_{n \text{ inside boundary}} h_n T(m, n) = - \sum_{n \text{ on boundary}} h_n T(m, n) \quad (35)$$

$$\begin{matrix} \downarrow \\ na(m) \end{matrix} \begin{bmatrix} \ddots & & 0 \\ & \underline{\underline{A}} & \\ 0 & & \ddots \end{bmatrix} \xrightarrow{na(n)} \begin{bmatrix} h_1 \\ h_2 \\ \vdots \\ h_{Nm} \end{bmatrix} = \begin{bmatrix} \vdots \\ \vdots \\ \vdots \\ \vdots \end{bmatrix} \xrightarrow{hb(n)} \begin{bmatrix} \vdots \\ \vdots \\ \vdots \\ \vdots \end{bmatrix} \begin{matrix} \text{boundary} \\ \text{values} \end{matrix} \quad (36)$$

The m-th row of $\underline{\underline{A}}$ and $\underline{\underline{B}}$ is formed by Equation (35) with the n-th term corresponding to a column of $\underline{\underline{A}}$ if h_n is unknown. The appropriate column of $\underline{\underline{B}}$ is filled if h_n is a boundary node. There is no contribution to $\underline{\underline{A}}$ or $\underline{\underline{B}}$ for nodes on the z-axis ($\rho = 0$) since $H_n(\rho = 0) = 0$ and those nodal values of h_n are known. [13]

C. FINITE ELEMENT METHOD LIMITATIONS

The finite element method was successful for back-propagation of fields measured at distances less than 0.25 wavelengths from the surface of the sphere. When the field was

measured at distances greater than 0.25 wavelengths, errors due to back-propagation increased significantly. The same cases for which the measured field was generated were used for back-propagation. These results are summarized in Table 2. The program FEM2.M was used to determine the surface current due to back-propagation. It can be found in the Appendix.

BACK-PROPAGATION RESULTS: FINITE ELEMENT METHOD					
Case	Sphere Radius (λ)	Field Distance (λ)	Modes	H_{ϕ} RMS Error (%)	J_{θ} RMS Error (%)
FEM1a	1	1.2	14	0.0590	0.9976
FEM1b	1	2	24	0.0338	30.09
FEM1c	1	4	50	0.0147	25.87
FEM2a	5	5.2	64	0.0043	0.7406
FEM2b	5	6	74	0.0052	57.18
FEM2d	5	5.26	64	0.0042	662.9
FEM3a	10	10.2	128	0.0017	0.7333
FEM3d	10	10.26	128	0.0063	5.547

Table 2. Centered Sphere Back-Propagation Results: Finite Element Method

The magnitude and phase of the surface current on the PEC sphere, as determined through the finite element method, is shown in Figures 31 through 42. These figures help to tell the complete story of the accuracy in back propagating to obtain the current. In each figure the “exact” quantity is depicted by a solid line and the calculated quantity is depicted by dots. Note that in both the magnitude and phase plots the calculated quantity closely matches the exact quantity for the cases in which the \overline{H} field is measured less than 0.25 wavelengths away from the surface of the sphere. In the cases where the distance is one wavelength, the error is immense. Cases FEM2d and FEM3d have been added to the original nine test cases in order to demonstrate what happens when the measurement distance is increased to 0.26 wavelengths from the surface of the sphere. The following section will investigate the cause of this error.

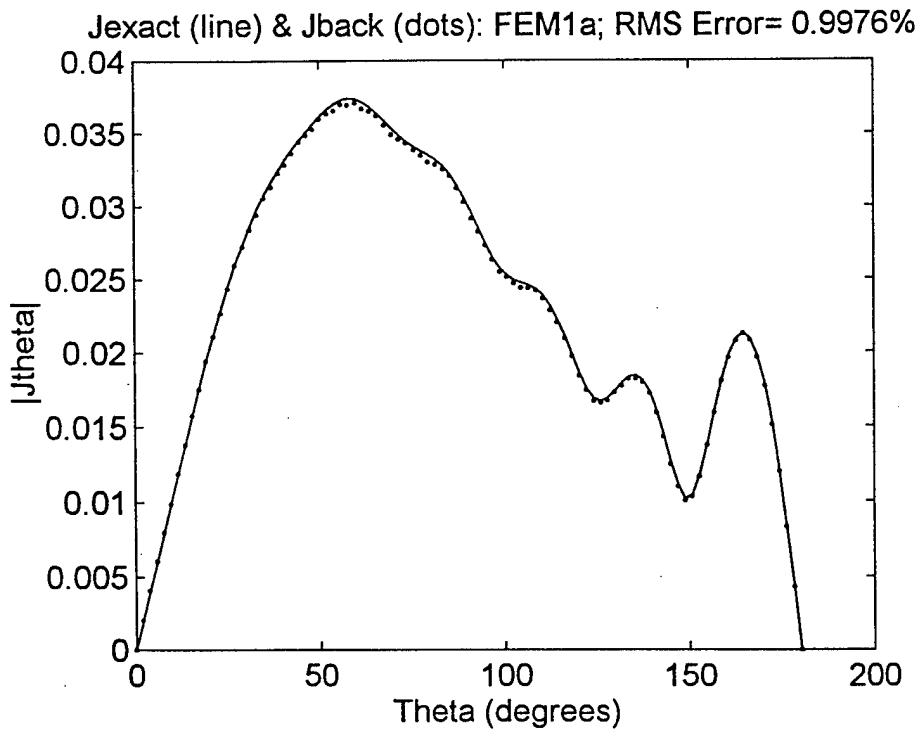


Figure 31. Magnitude Comparison: FEM1a

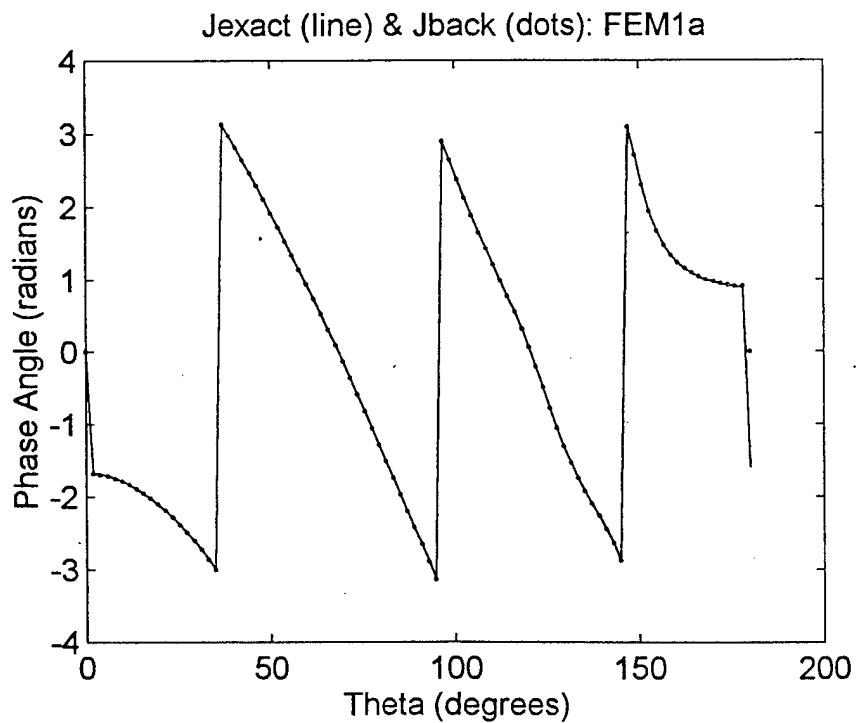


Figure 32. Phase Comparison: FEM1a

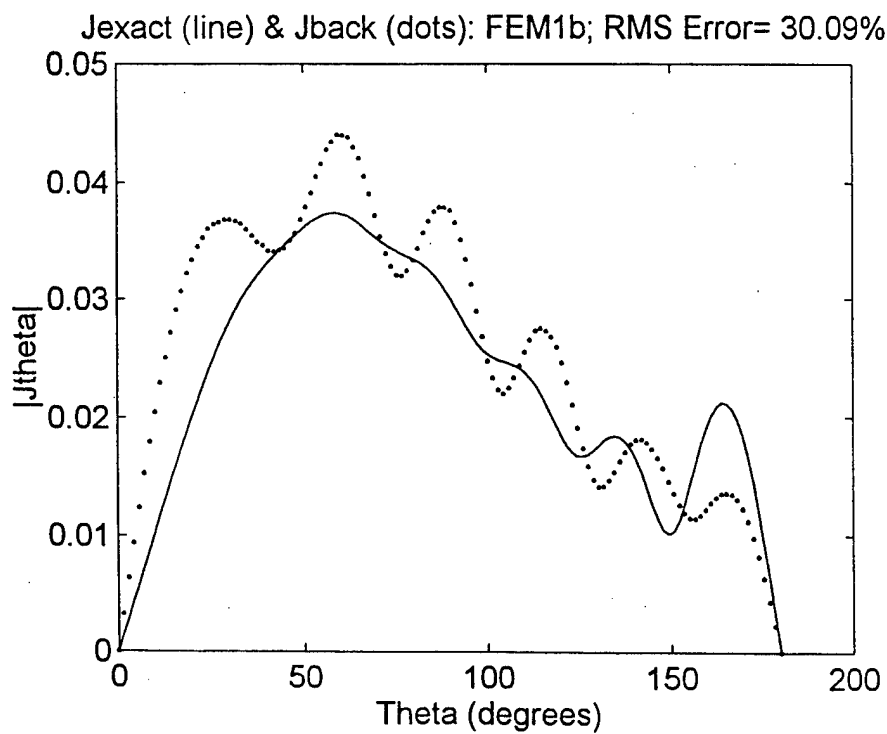


Figure 33. Magnitude Comparison: FEM1b

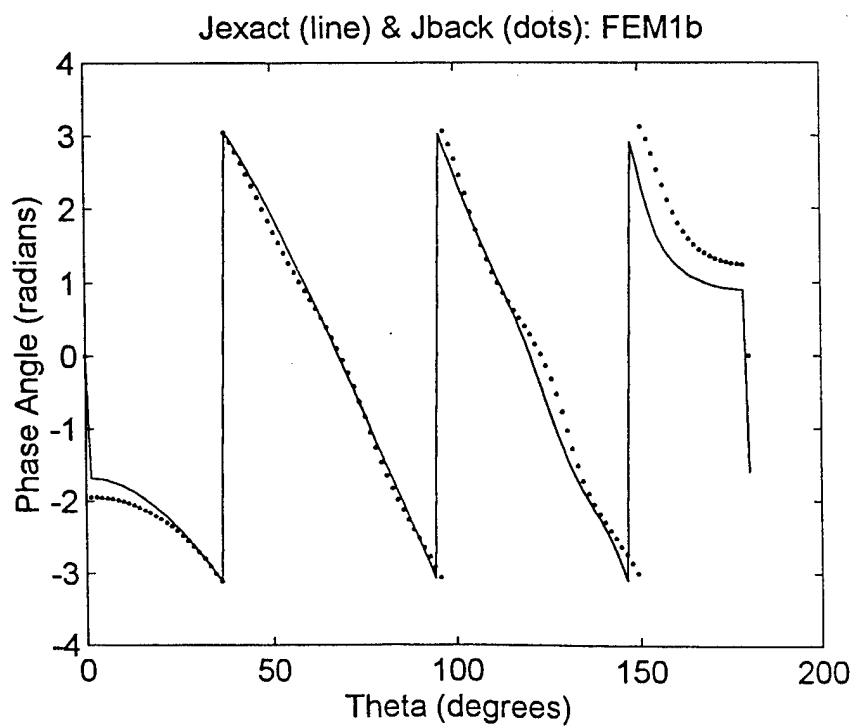


Figure 34. Phase Comparison: FEM1b

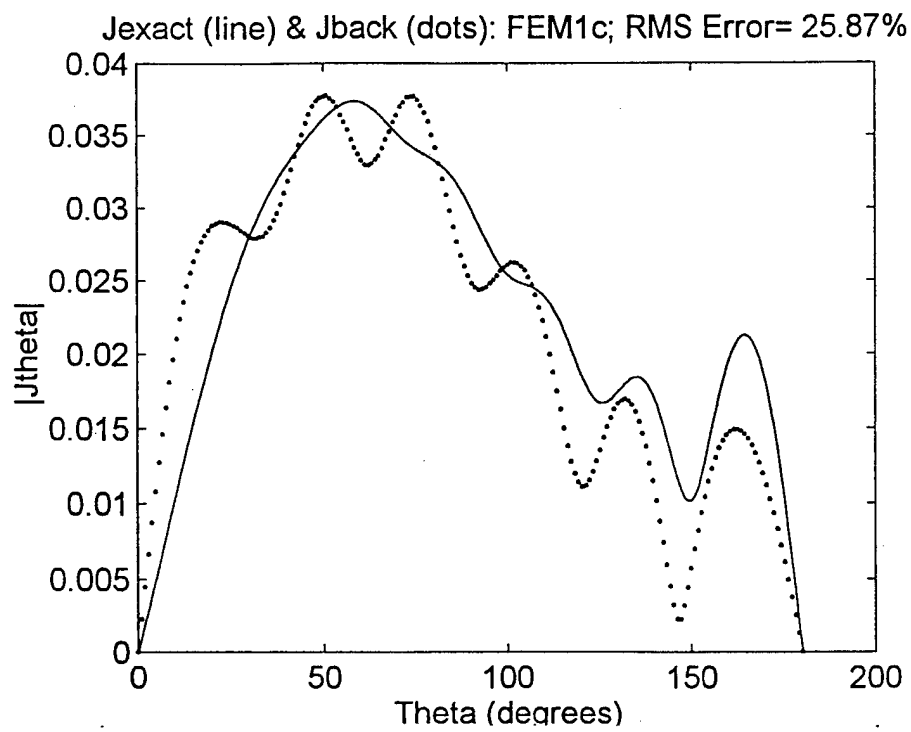


Figure 35. Magnitude Comparison: FEM1c

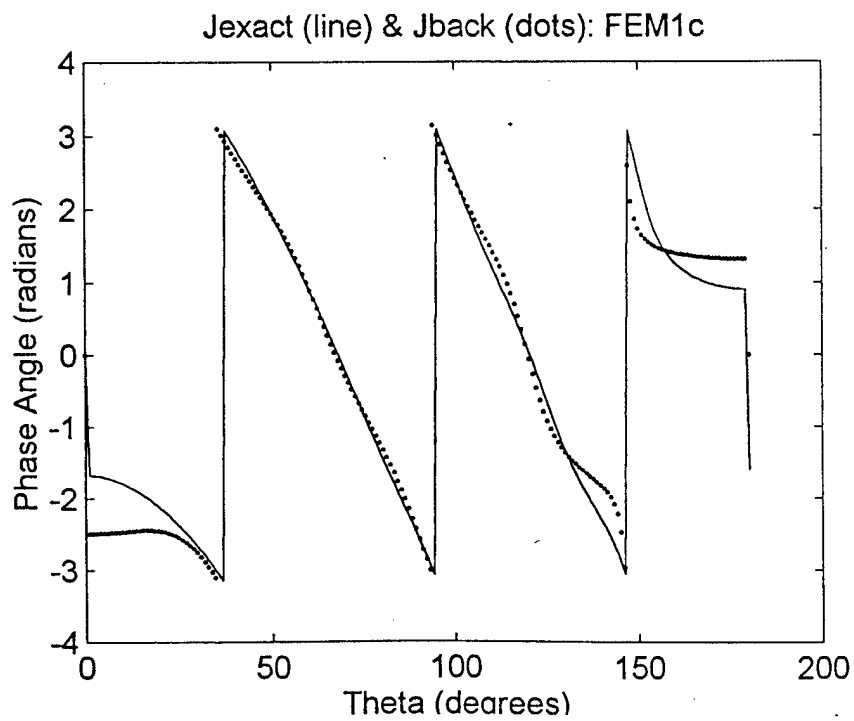
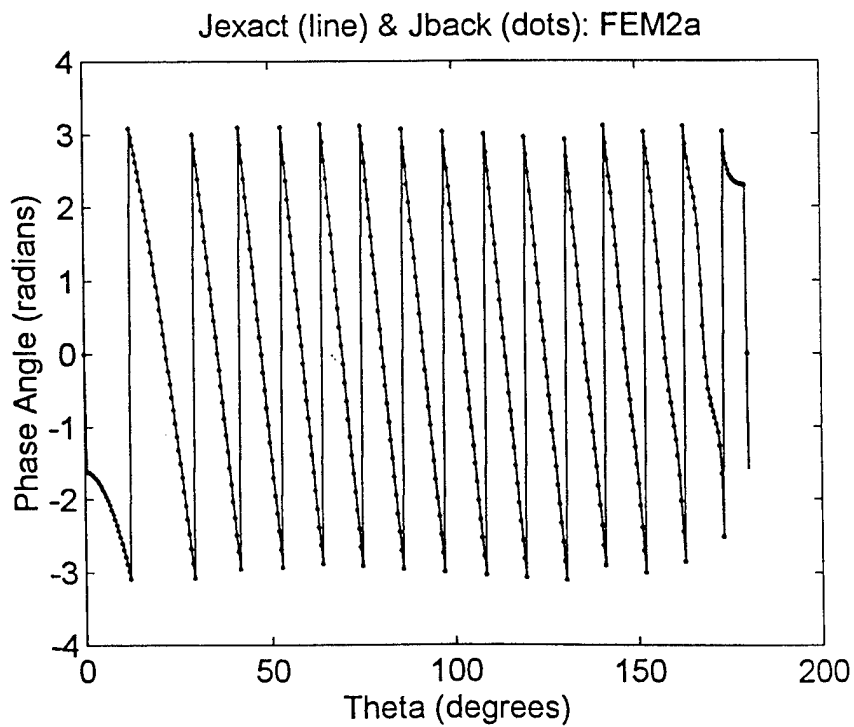
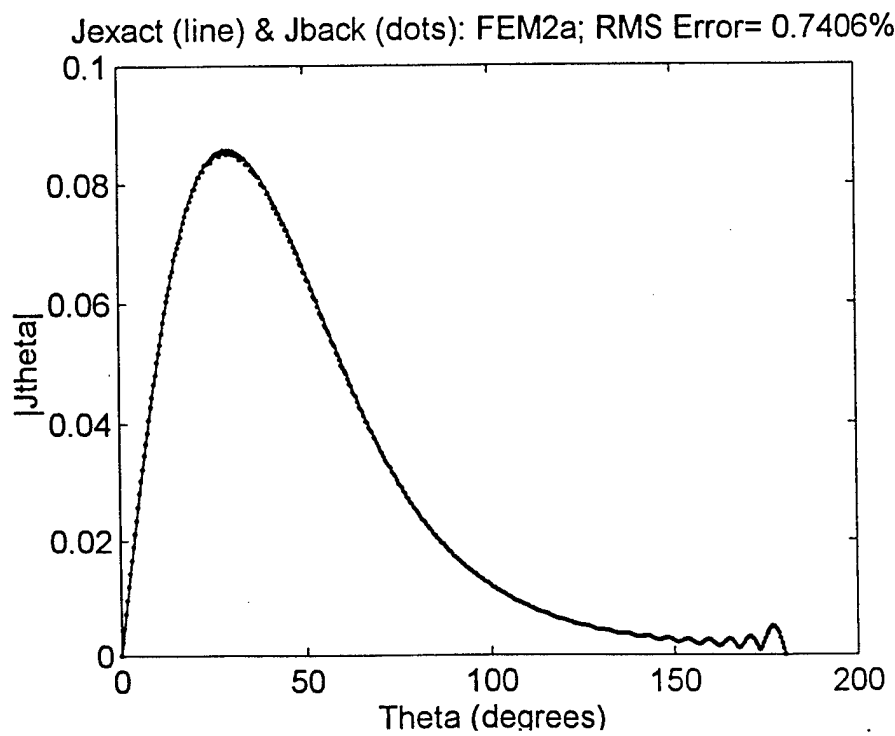


Figure 36. Phase Comparison: FEM1c



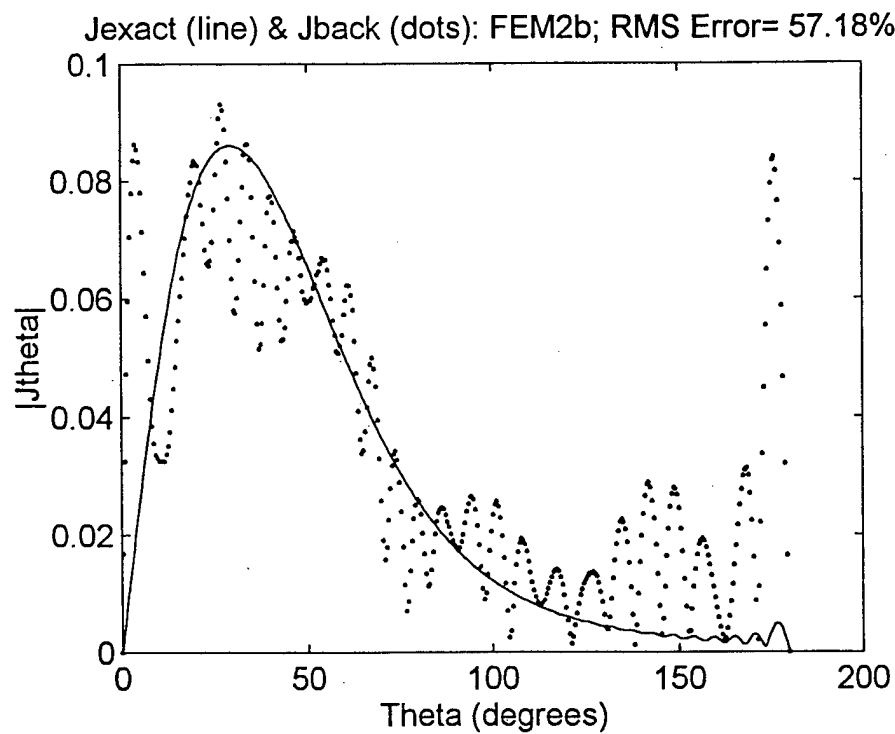


Figure 39. Magnitude Comparison: FEM2b

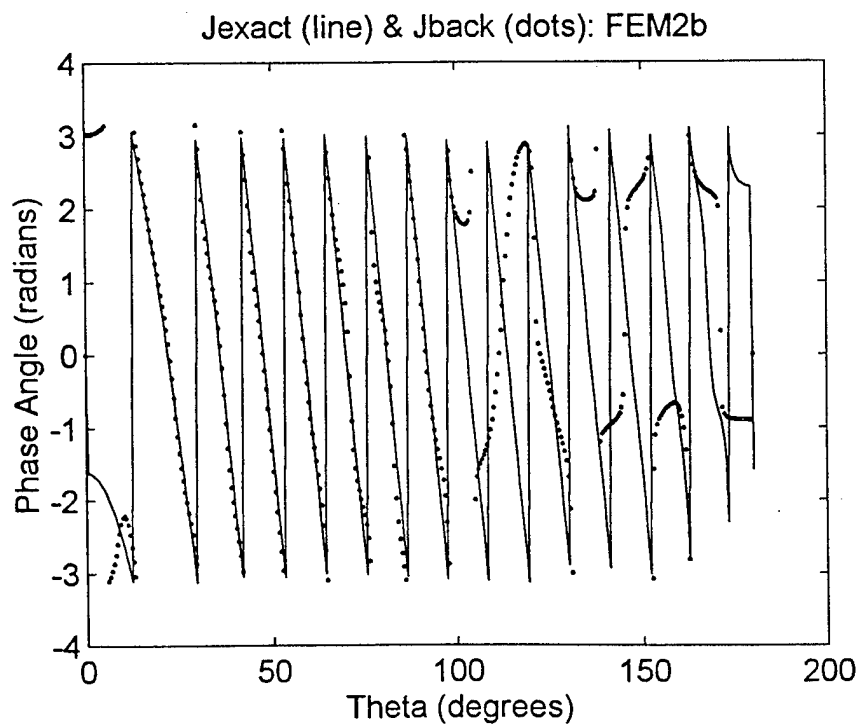


Figure 40. Phase Comparison: FEM2b

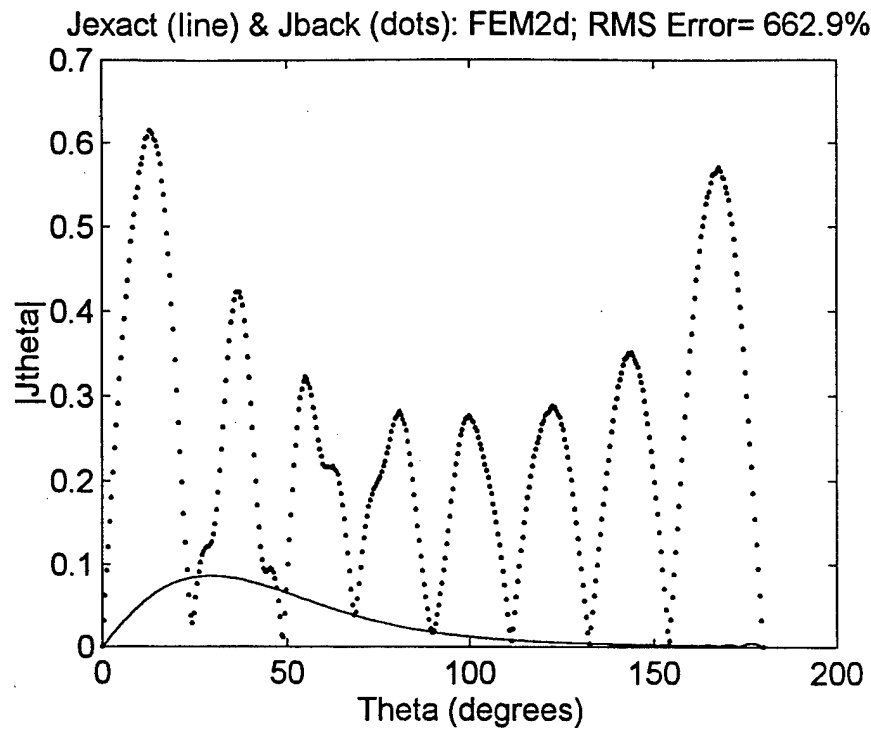


Figure 41. Magnitude Comparison: FEM2d

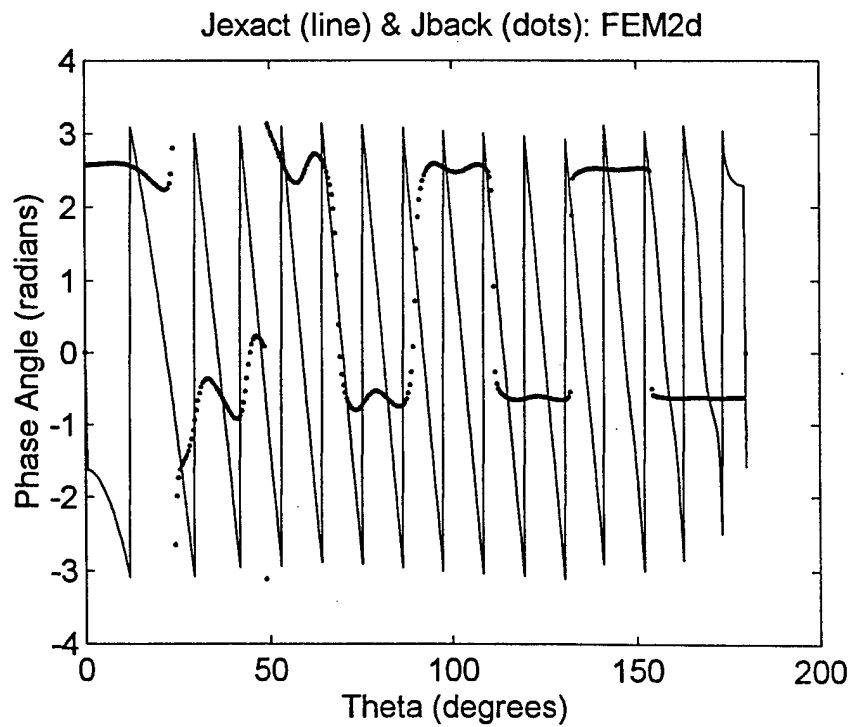


Figure 42. Phase Comparison: FEM2d

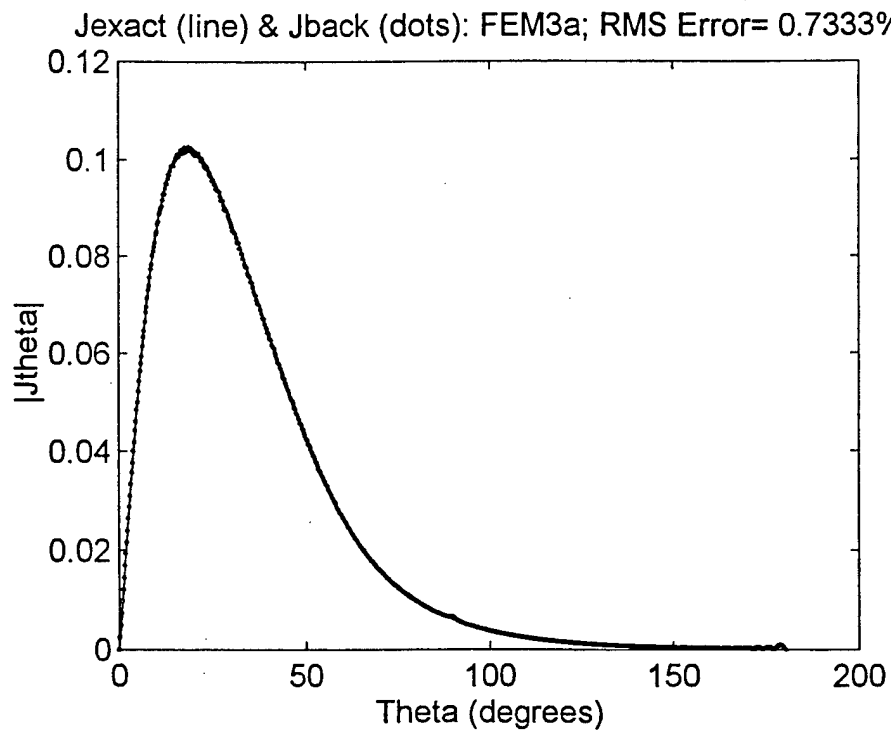


Figure 43. Magnitude Comparison: FEM3a

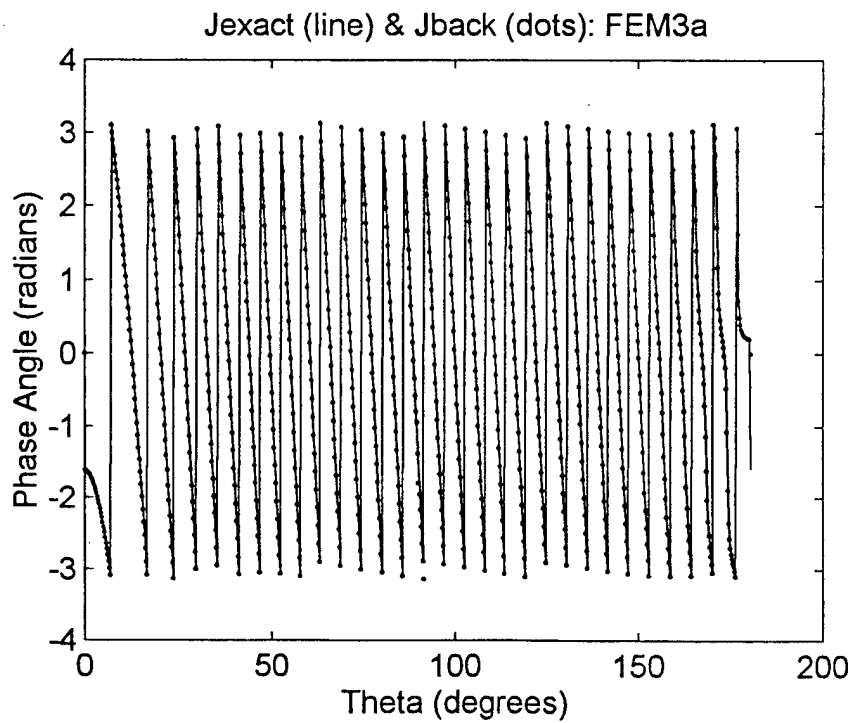


Figure 44. Phase Comparison: FEM3a

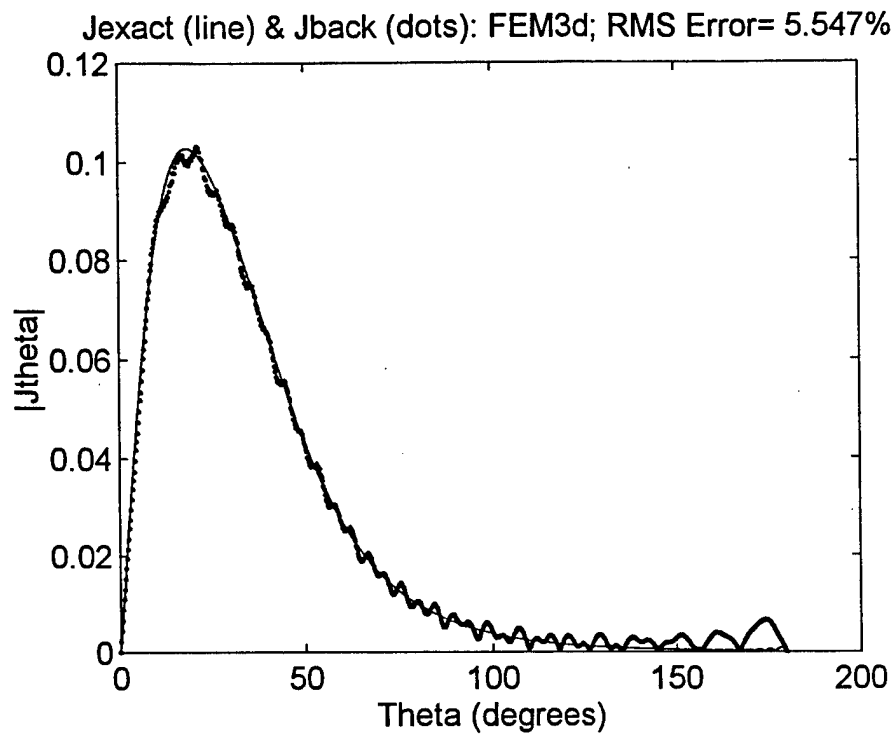


Figure 45. Magnitude Comparison: FEM3d

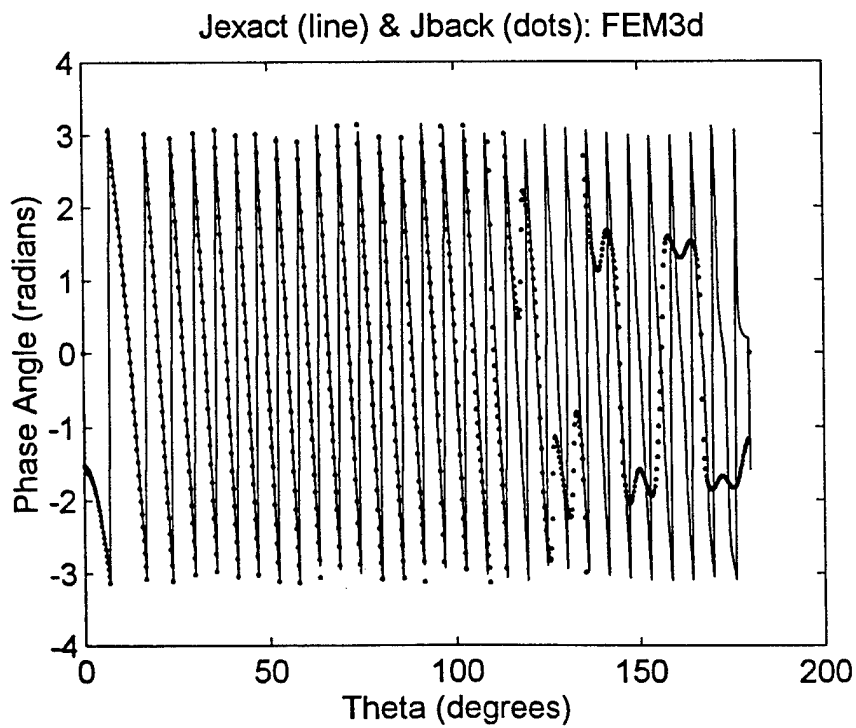


Figure 46. Phase Comparison: FEM3d

When back-propagating measurements are made at distances greater than 0.25 wavelengths from the surface of the sphere using the FEM approach, the RMS error of the predicted surface current tends to increase dramatically relative to the situation of smaller distances. This appears to result from resonant modes injecting themselves into the solution in varying degrees. Figure 47 shows the single mode RMS error for a centered PEC sphere used in case FEM1a. Note that the RMS error associated with each mode is relatively low; all but two are below one percent. The results shown Table 2 indicate that back-propagation gave a solution with less than one percent RMS error. Figure 48 shows the single mode RMS error for case FEM1b. In this case the measured field was one wavelength from the surface of the sphere. Note that the lower order modes generally have RMS error in the neighborhood of five percent or less, except for mode $n = 5$ which is nearly fifty percent RMS error. This error "spike" indicates a resonant mode that significantly alters the solution. As can be seen in Figures 48 through 53, the resonant modes seem to appear in only the cases where the measurement distance is greater than 0.25 wavelengths from the surface of the sphere.

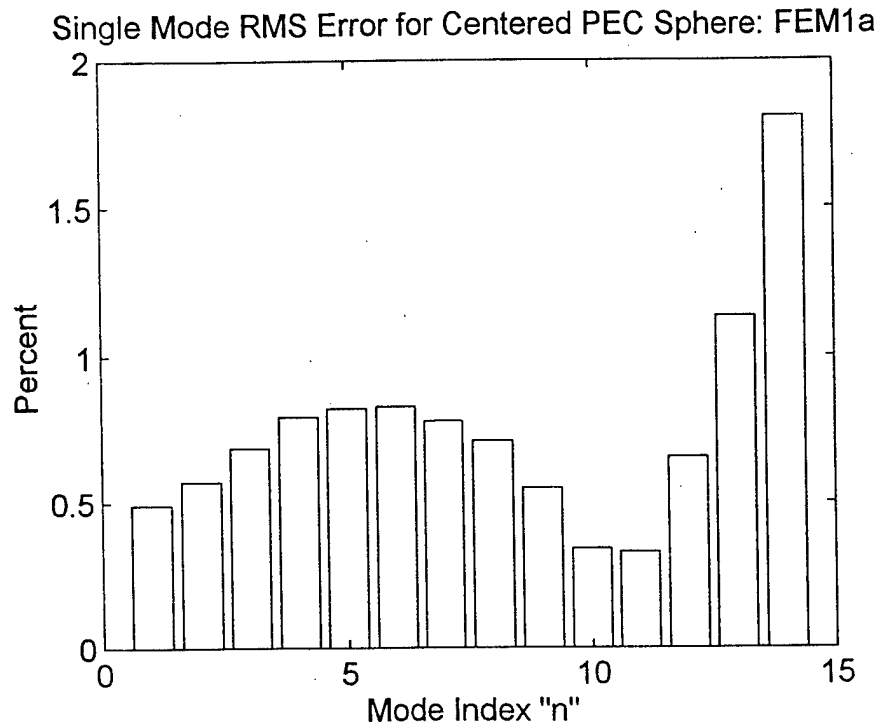


Figure 47. Single Mode RMS Error: Case FEM1a

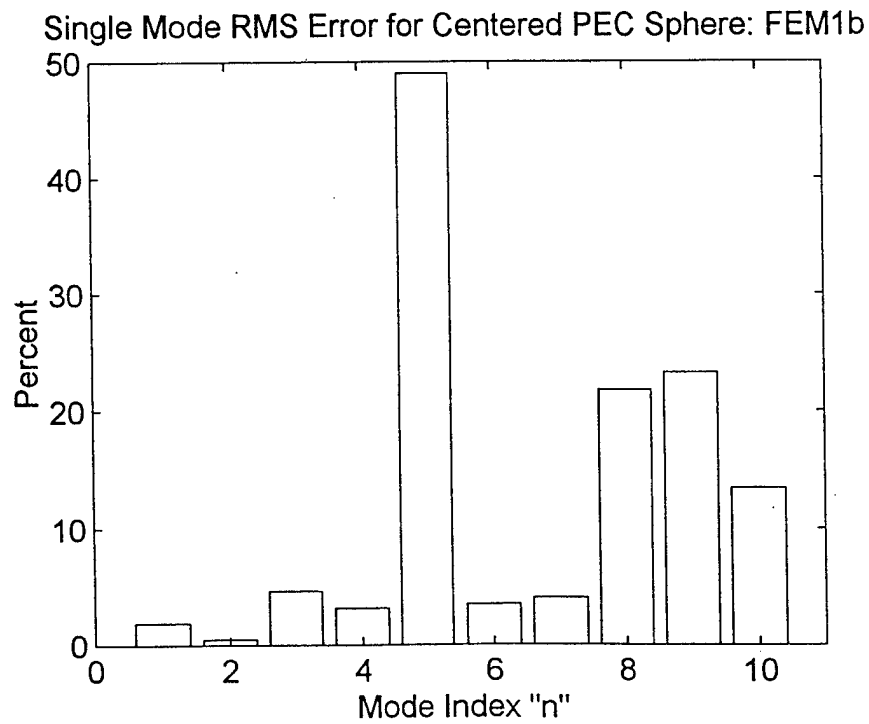


Figure 48. Single Mode RMS Error: Case FEM1b

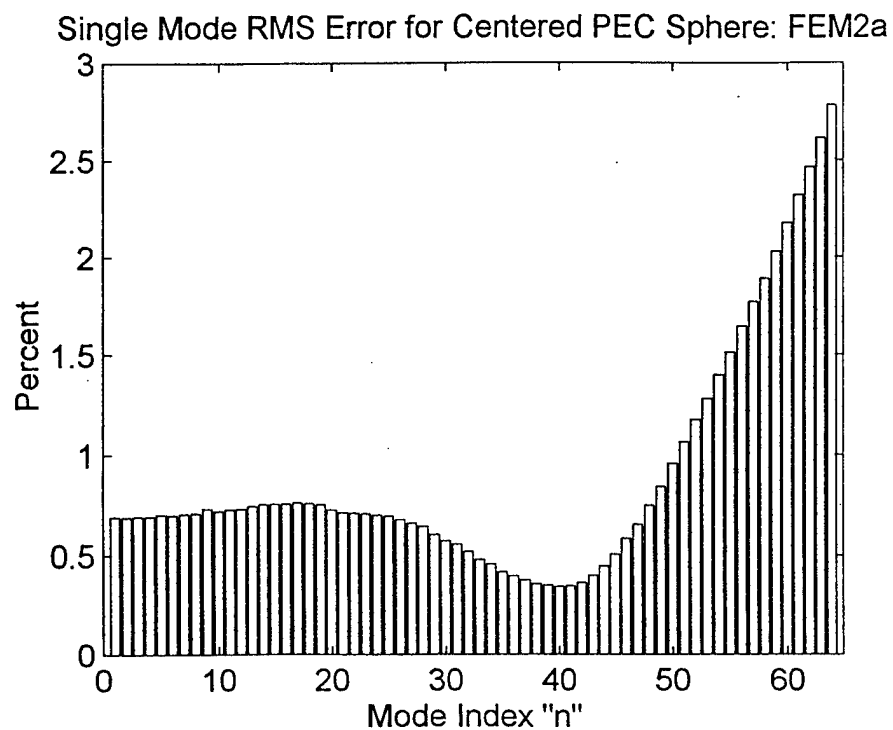


Figure 49. Single Mode RMS Error: Case FEM2a

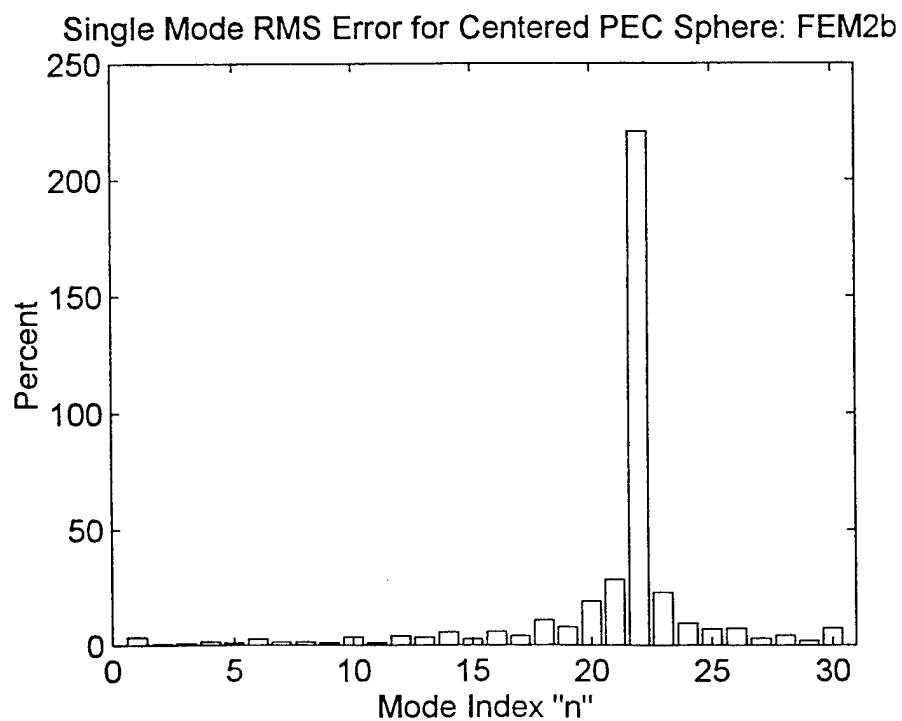


Figure 50. Single Mode RMS Error: Case FEM2b

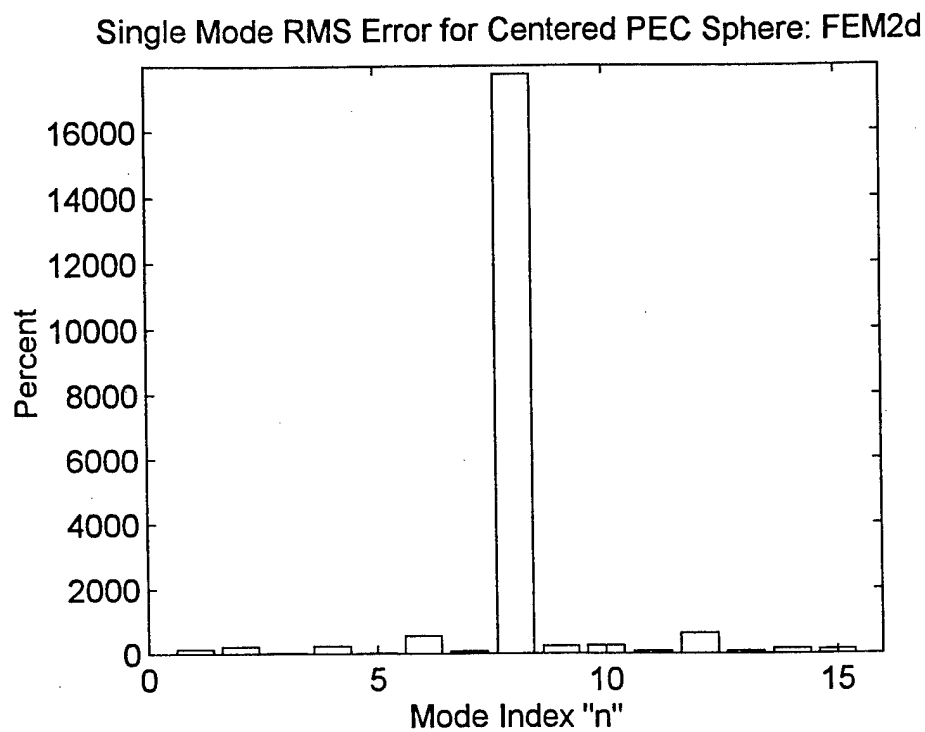


Figure 51. Single Mode RMS Error: Case FEM2d

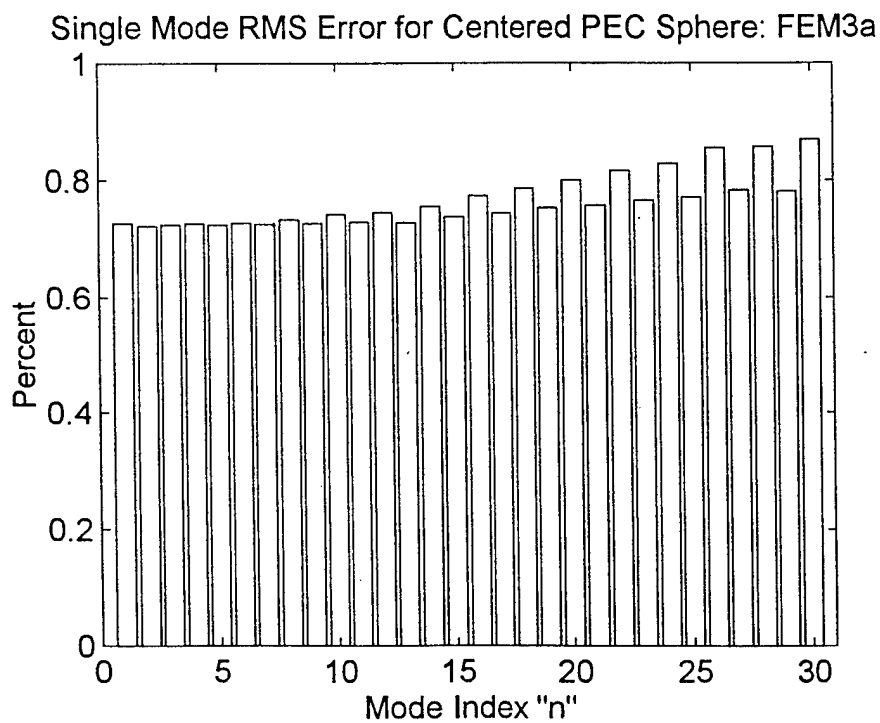


Figure 52. Single Mode RMS Error: Case FEM3a

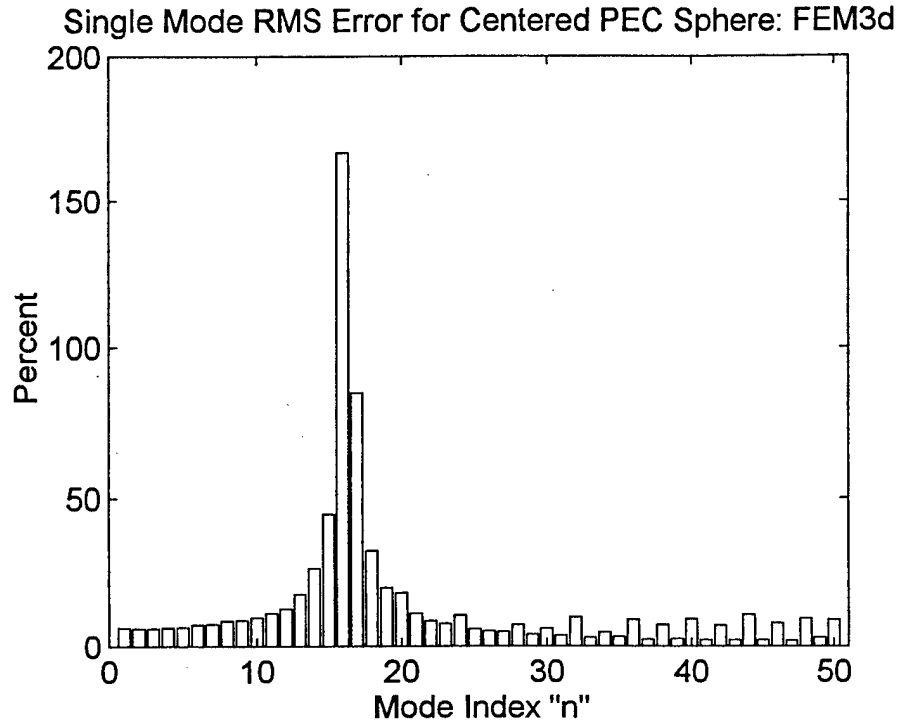


Figure 53. Single Mode RMS Error: Case FEM3d

Another way to view this phenomenon is by looking at the product solution parts of $H_p(r, \theta) = g(r) \cdot h(\theta)$ for a given mode, n . The radial variation, $g(r)$, to be shown in the upper subplots, indicates the contribution at the PEC sphere surface due to a constant contribution of $g(b) = 1$ on the outer boundary. Figures 54 and 55 show the radial variation for modes $n = 4$ and $n = 5$, respectively, for the case FEM1b. Note that mode 4 provides relatively small contribution at the PEC sphere surface. Mode 5, however, indicates an extremely large contribution at the PEC sphere surface. Two additional cases have been added here to further illustrate this observation. Cases FEM2d and FEM3d shown in Figures 56 and 57, respectively, are both cases in which the measured field is 0.26 wavelengths from the surface of the sphere. Note the large contribution at the surface of the sphere due to the resonant modes captured in each of these figures.

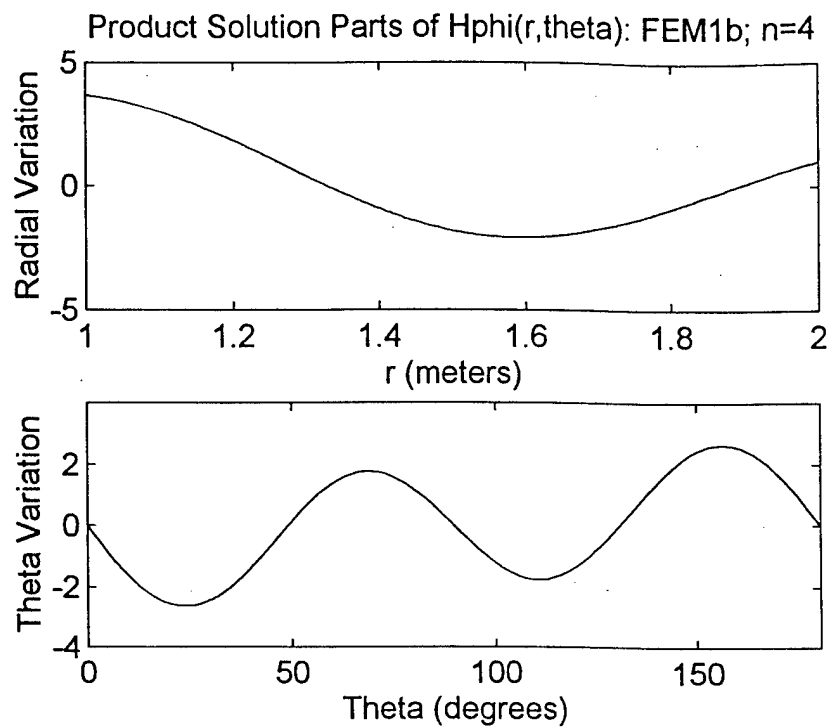


Figure 54. Product Solution Parts: Case FEM1b, $n = 4$

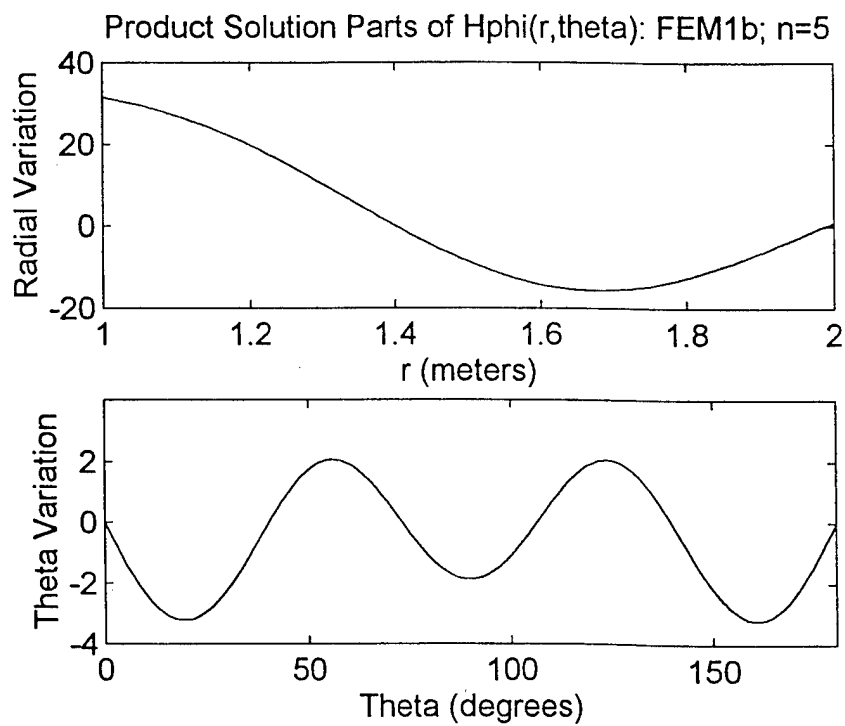


Figure 55. Product Solution Parts: Case FEM1b, $n = 5$

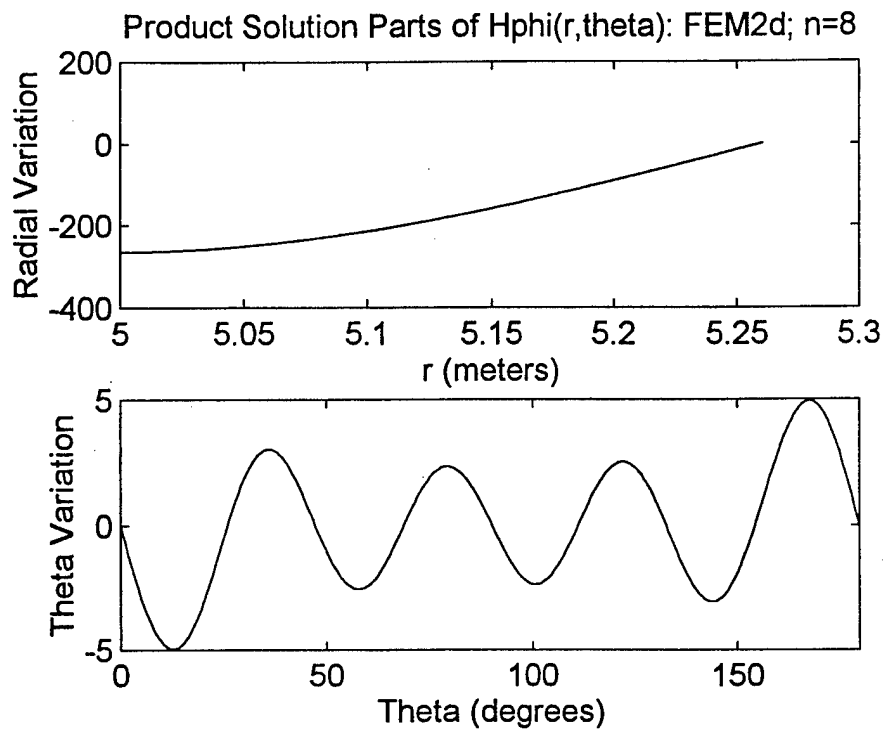


Figure 56. Product Solution Parts: Case FEM2b, $n = 8$

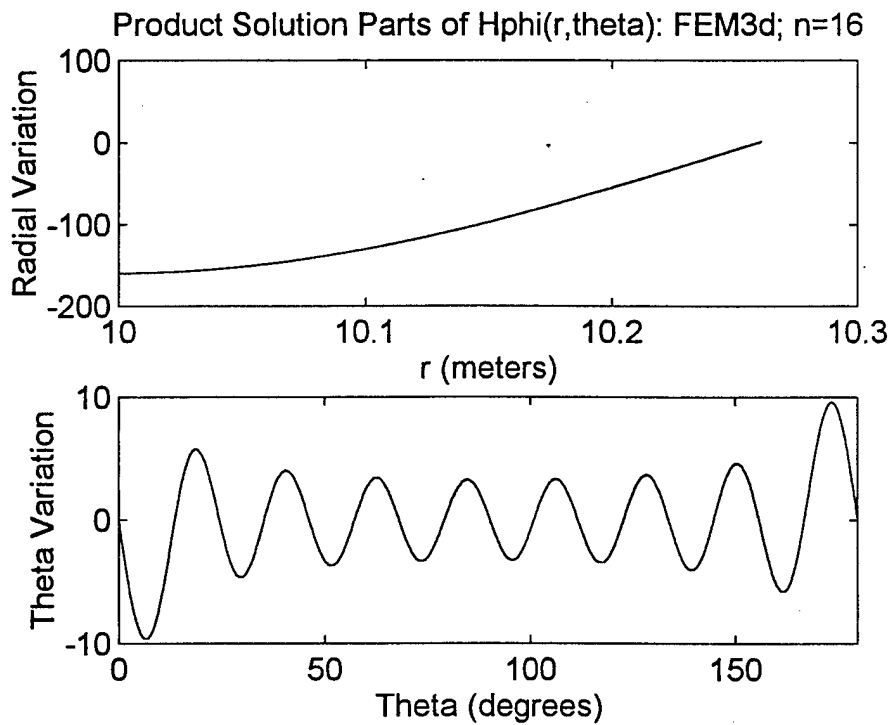


Figure 57. Product Solution Parts: Case FEM3b, $n = 16$

Additional insight is provided by viewing the resonant modes that appear when the field is measured at varying distances from a fixed size sphere. Figure 58 considers modes $n = 1$ to 100. Each line in Figure 58 displays the contribution of $g(a)$ from a single mode at the sphere surface as a result of a constant contribution of $g(b) = 1$ at the boundary distance. The "best radius," $b = 5.641 \lambda_0$ in this case, provides the minimum $g(a)$ from all modes applied as $g(b) = 1$. From the perspective of minimal resonance effects, this is the best location to measure the field.

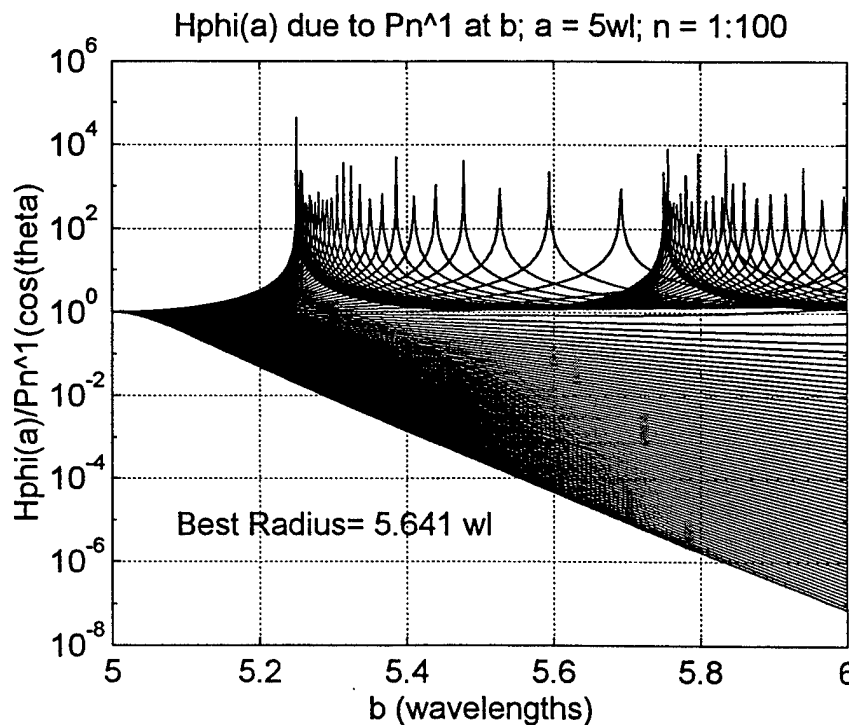


Figure 58. Resonant Effects at Various Outer Boundary Locations

D. TRANSFER MATRIX FOR CENTERED SPHERE

As can be seen in Table 2 the results due to back-propagation are poor for measurements made greater than approximately 0.25 wavelengths from the surface of the sphere. A transfer matrix using spherical harmonics for a centered sphere was developed

to accurately back propagate the field on the outer boundary to that on the sphere, without the bothersome injection of resonant modes as appear with the FEM solution. This method will give some indication as to the spatial resolution required when measuring the field so that the source current on the sphere can be accurately determined.

Figure 58 shows a meridian plane for a centered sphere of radius a enclosed by an outer boundary arc of radius b . For any radius r , where $a \leq r \leq b$, the total \bar{H} field can be determined by: [14]

$$H_\phi(r, \theta) \cong \sum_{n=1}^N a_n \left[\frac{\hat{J}_n(kr)}{kr} + b_n \frac{\hat{H}_n^{(2)}(kr)}{kr} \right] P_n^1(\cos \theta) \quad (37)$$

where:

$$b_n = -\frac{\hat{J}_n'(ka)}{\hat{H}_n^{(2)'}(ka)} \quad (38)$$

forces $E_\theta = 0$ for each mode on the surface of the sphere.

A specified $f(\theta) = H_\phi(b, \theta)$ will provide a set $\{a_n\}$. The a_n coefficients are determined by moment matching, using orthogonality of Legendre functions. This technique is detailed in [14]. The transfer matrix H_s is developed such that

$$H_\phi(a, \theta_q) = \underline{\underline{H_s}}(q, p) \cdot H_\phi(b, \theta_p) \quad (39)$$

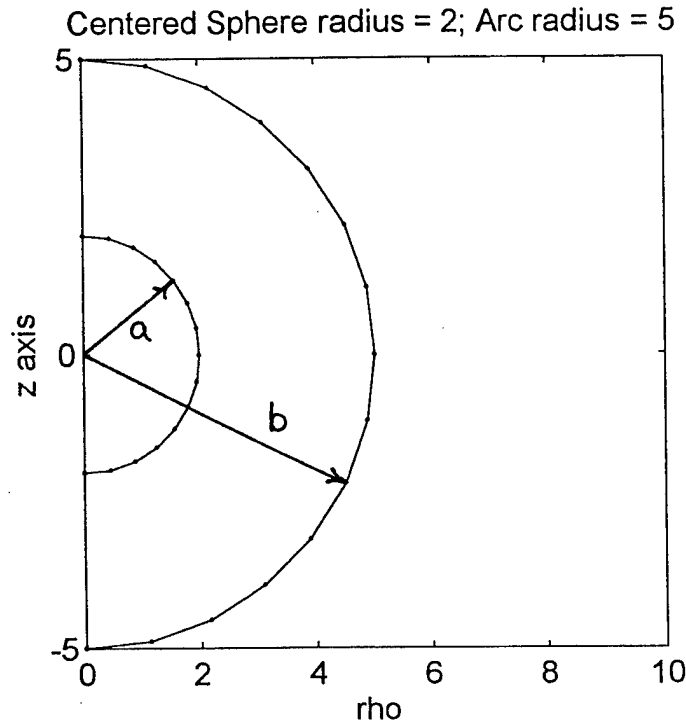


Figure 59. Meridian Plane of Centered Sphere

where $H_{\theta}(b, \theta_p)$ is a column array of the θ_p sampled field at radius b , as determined in Chapter II. The array product results in the column array of H_{θ} at radius a which corresponds to the surface of the sphere. From this result the surface current is then determined using Equation (9b). The test cases using the transfer matrix were generated using the program HSPHERE1.M which can be found in the Appendix. Table 3 tabulates the results and compares them to those obtained using the finite element method. It should be noted that the transfer matrix works only for a centered sphere and can not be applied to any arbitrary axisymmetric body.

SURFACE CURRENT RESULTS USING TRANSFER MATRIX						
Case	Sphere Radius (λ)	Field Distance (λ)	Modes	θ Segments	H_ϕ RMS Error (%)	J_θ RMS Error (%)
1a	1	1.2	14	94	0.0590	0.8085
1b	1	2	24	125	0.0338	0.6271
1c	1	4	50	188	0.0147	0.7349
2a	5	5.2	64	408	0.0043	0.7946
2b	5	6	74	376	0.0052	0.9453
2d	5	5.26	64	408	0.0042	0.7764
3a	10	10.2	128	801	0.0017	0.7885
3d	10	10.26	128	801	0.0063	0.7827

Table 3. Surface Current Results Using Transfer Matrix

The magnitude and phase of the surface current on the PEC sphere, as determined by the transfer array, is shown in Figures 60 through 77. Once again these figures help to tell the complete story of the surface current. In each figure the exact quantity is depicted by a solid line and the calculated quantity is depicted by dots. Note that in both the magnitude and phase plots the calculated quantity closely matches the exact quantity.

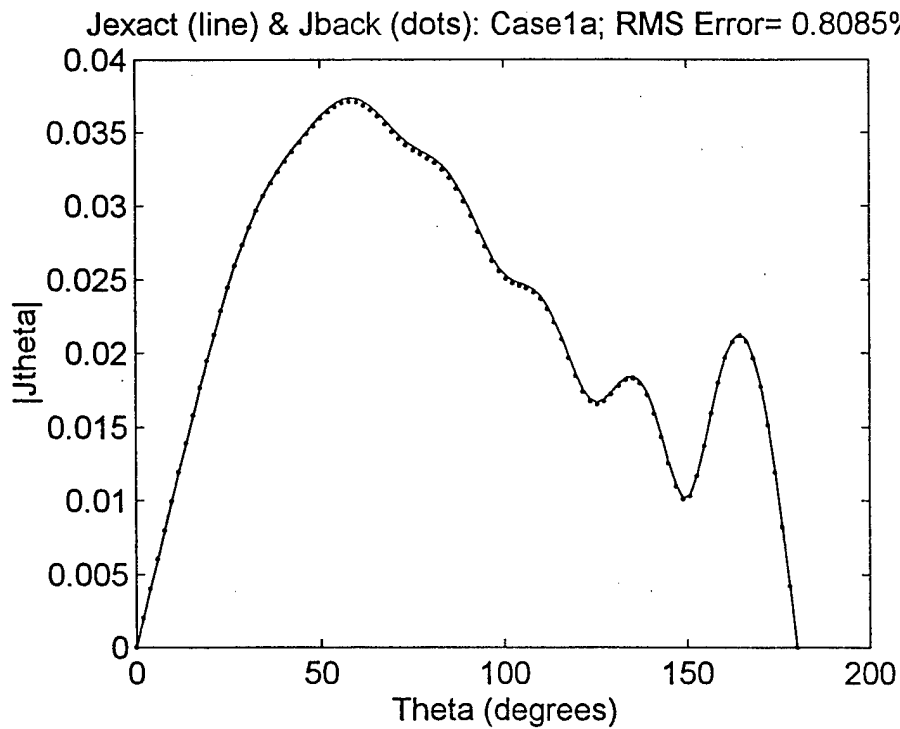


Figure 60. Magnitude Comparison: Case1a

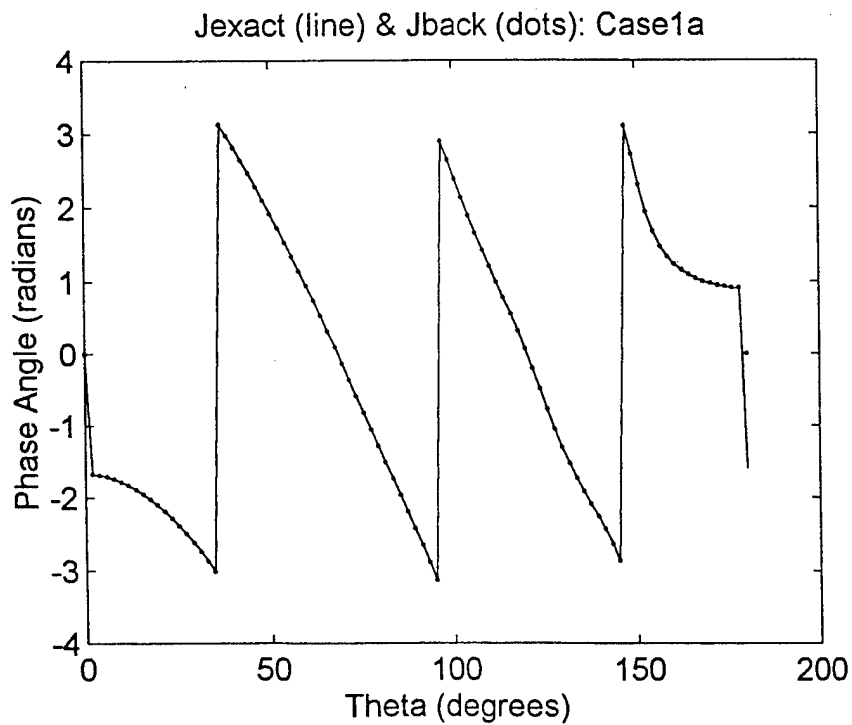


Figure 61. Phase Comparison: Case1a

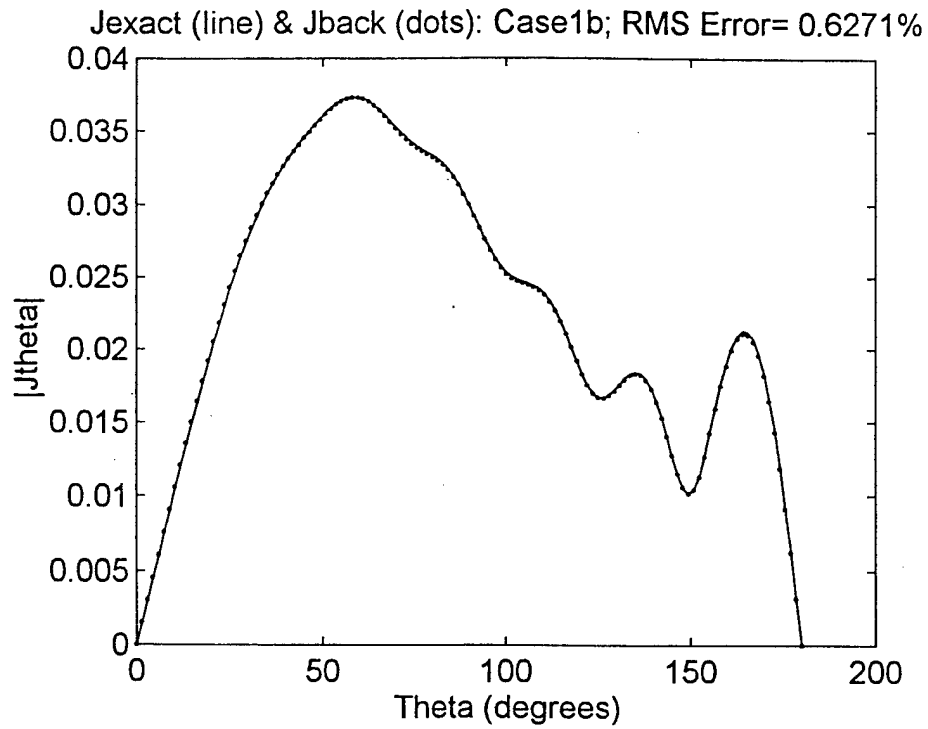


Figure 62. Magnitude Comparison: Case1b

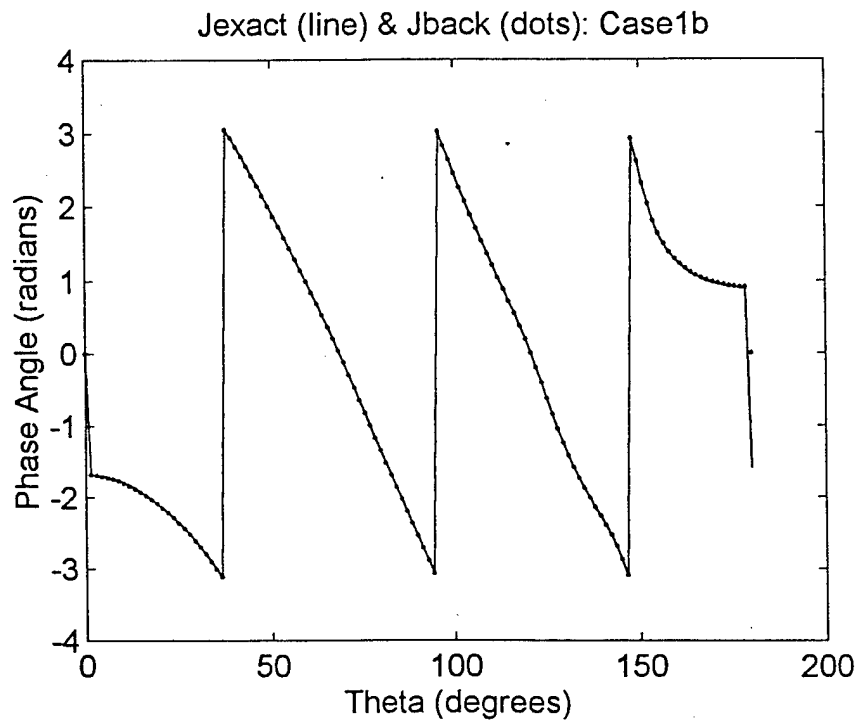


Figure 63. Phase Comparison: Case1b

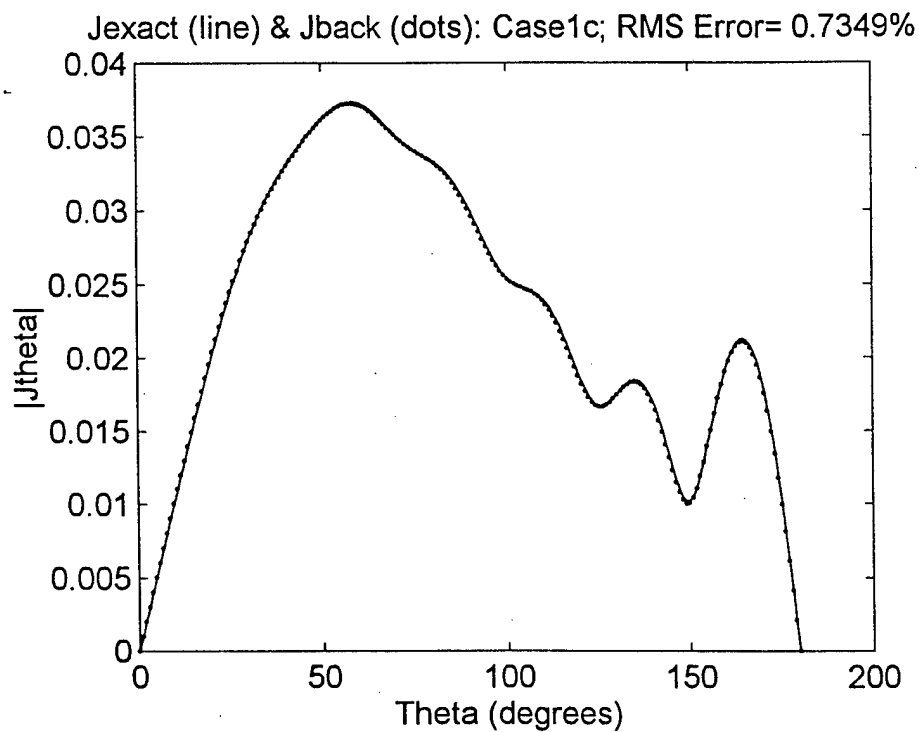


Figure 64. Magnitude Comparison: Case1c

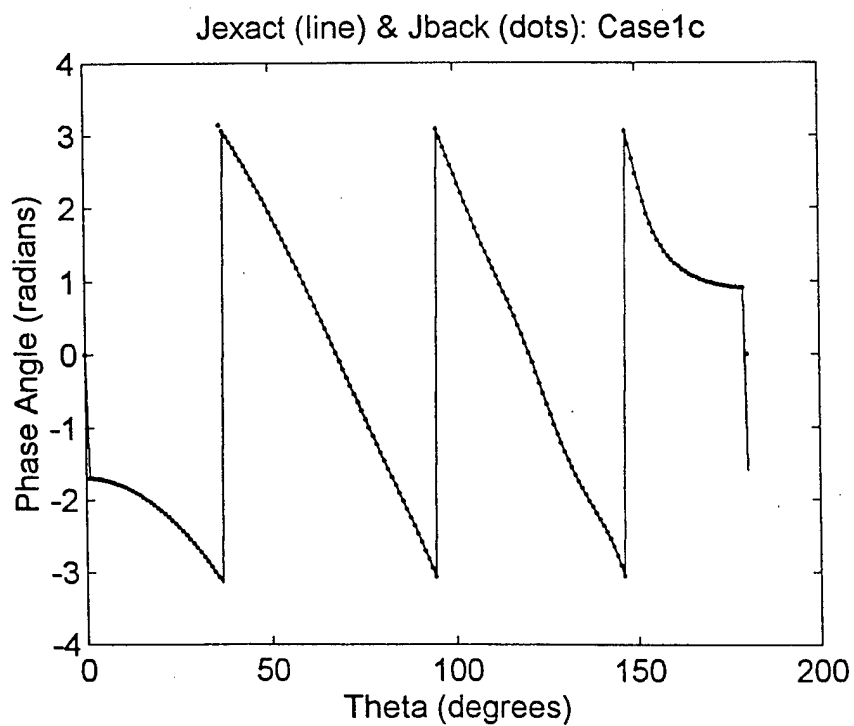


Figure 65. Phase Comparison: Case1c

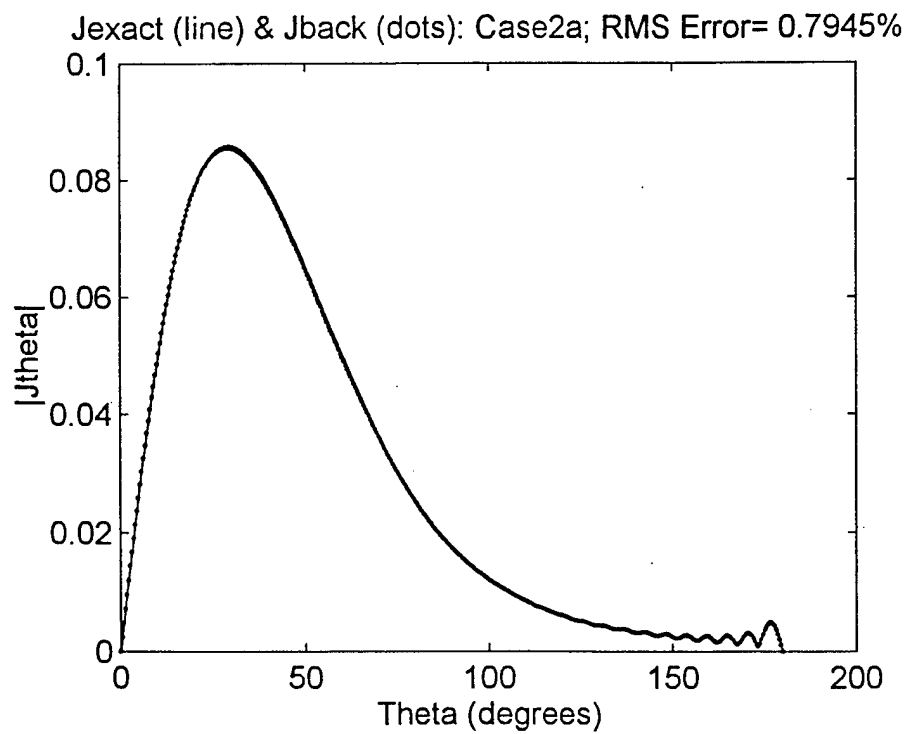


Figure 66. Magnitude Comparison: Case2a

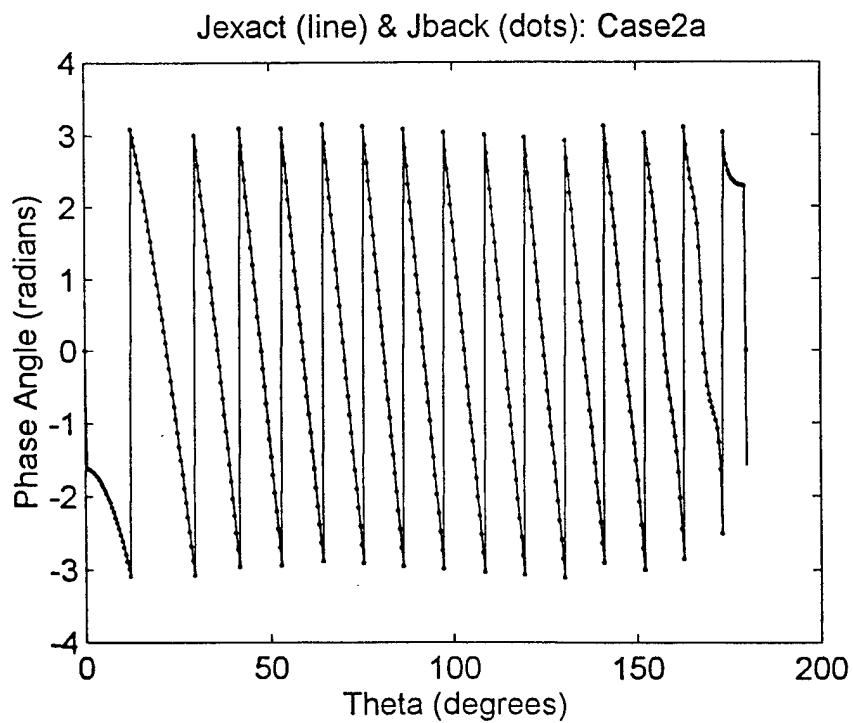


Figure 67. Phase Comparison: Case2a

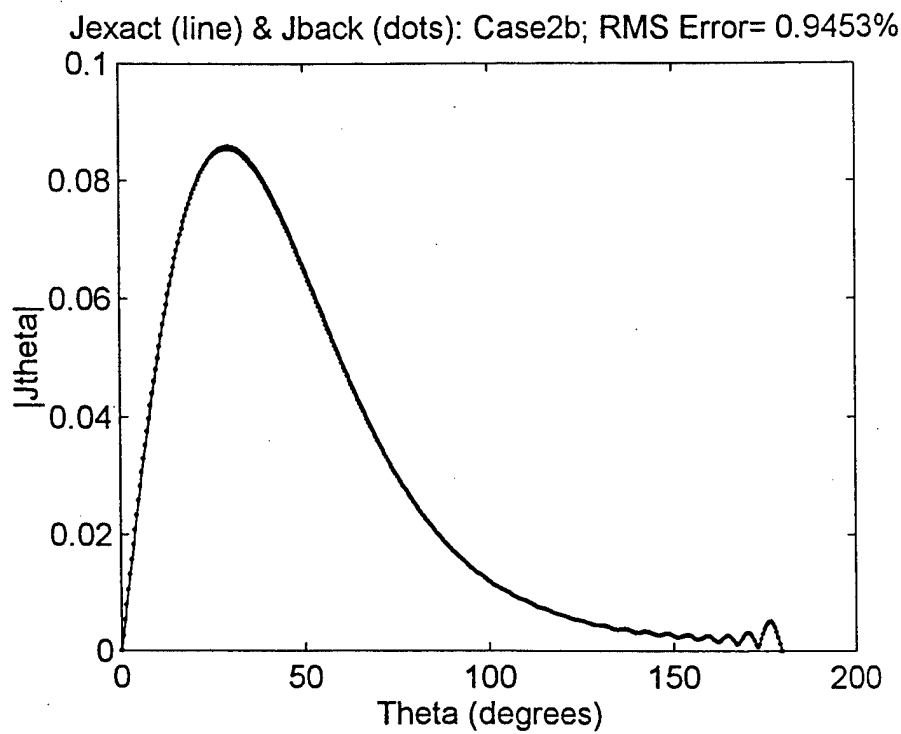


Figure 68. Magnitude Comparison: Case2b

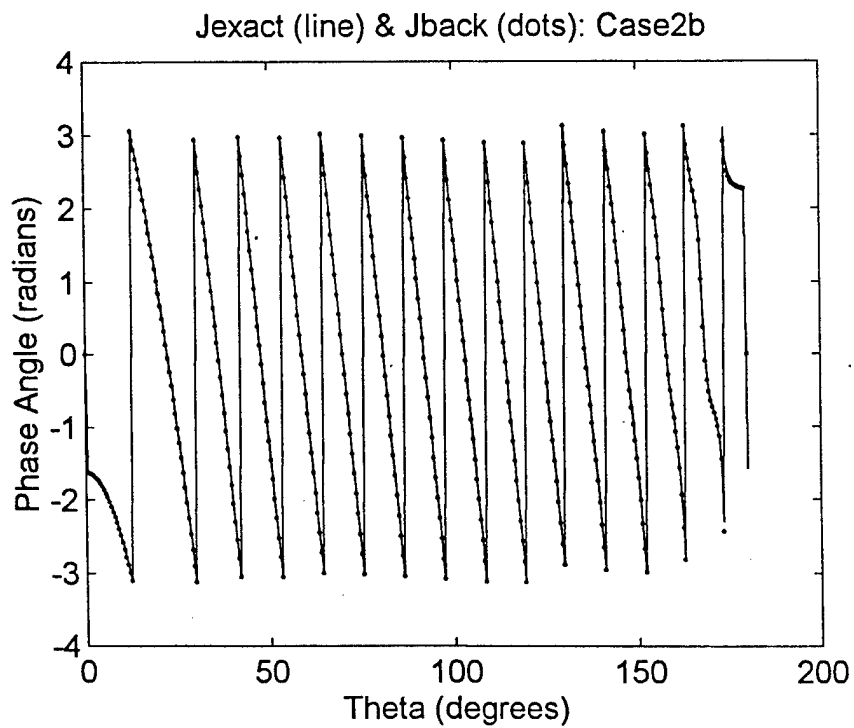


Figure 69. Phase Comparison: Case2b

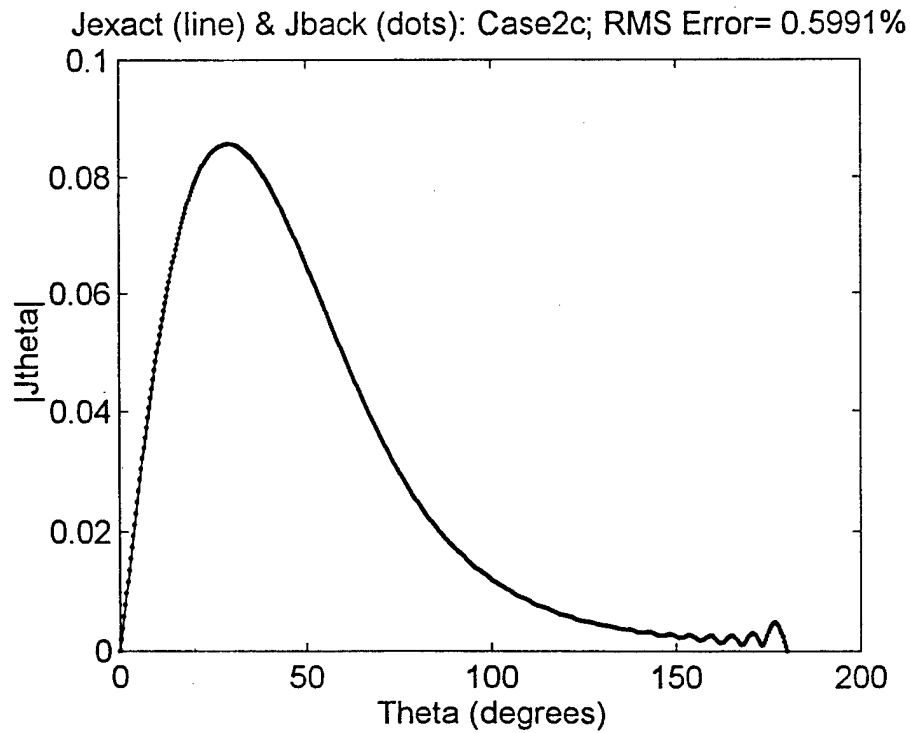


Figure 70. Magnitude Comparison: Case2c

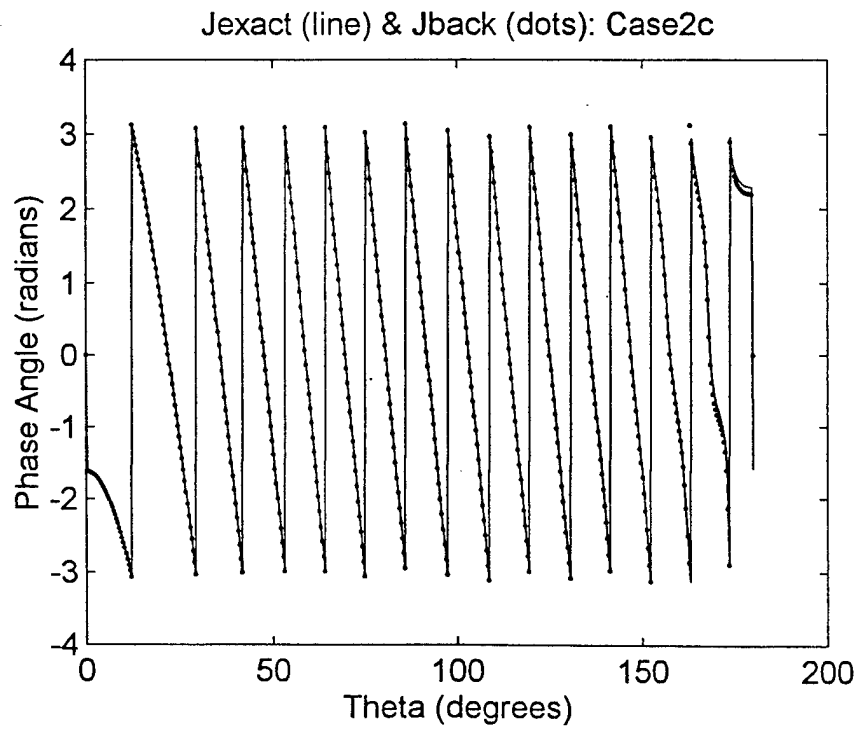


Figure 71. Phase Comparison: Case2c

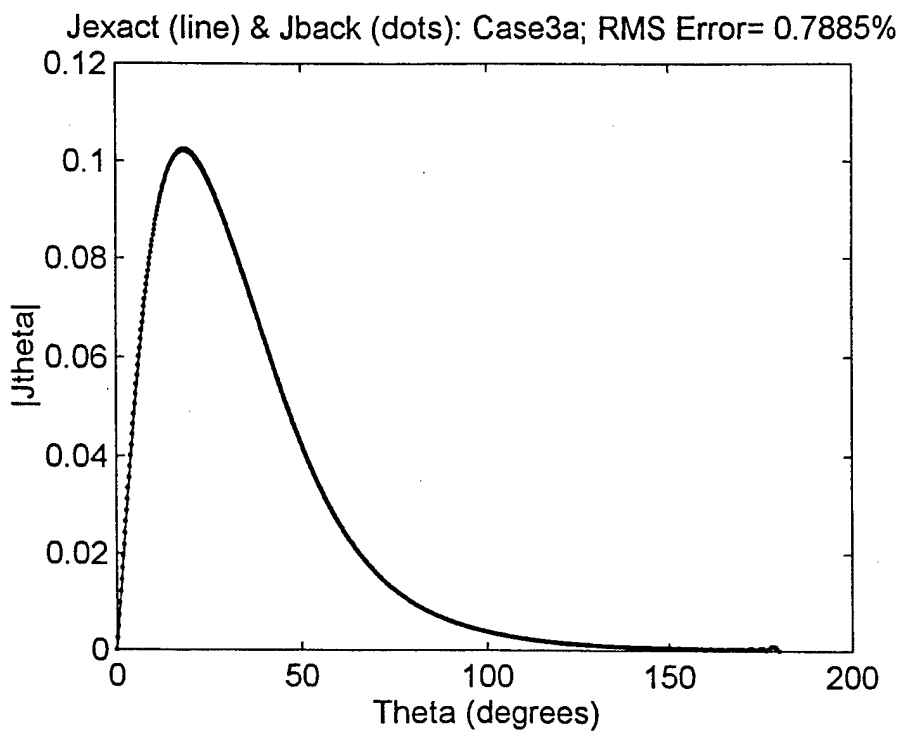


Figure 72. Magnitude Comparison: Case3a

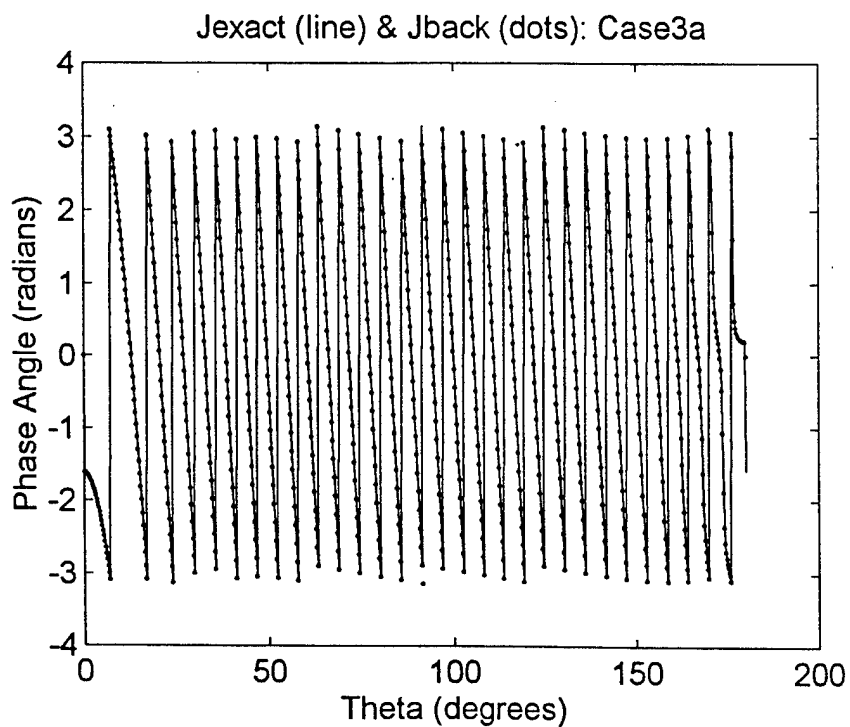


Figure 73. Phase Comparison: Case3a

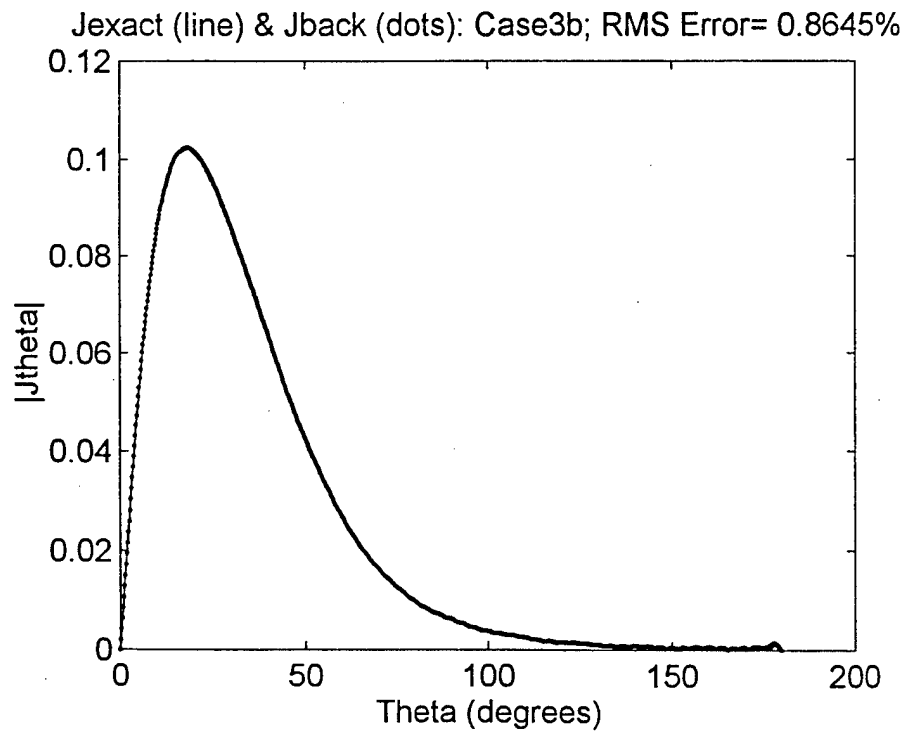


Figure 74. Magnitude Comparison: Case3b

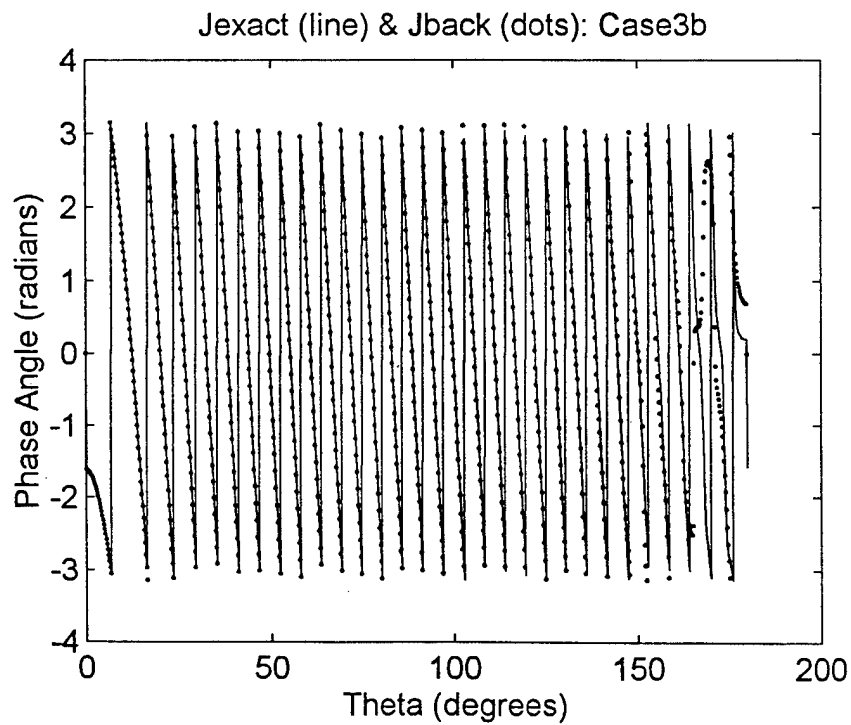


Figure 75. Phase Comparison: Case3b

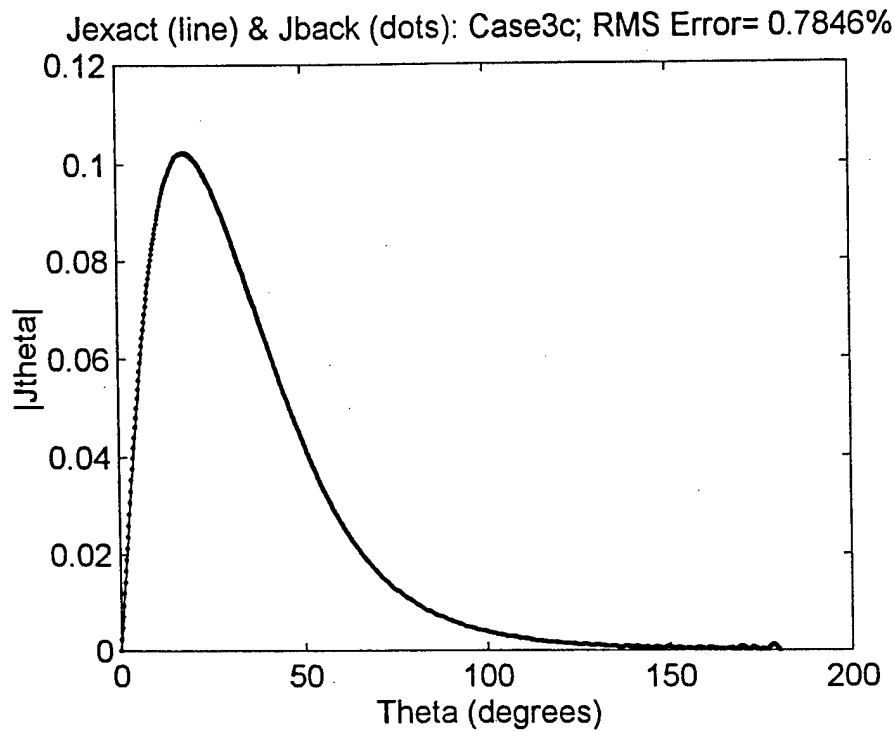


Figure 76. Magnitude Comparison: Case3c

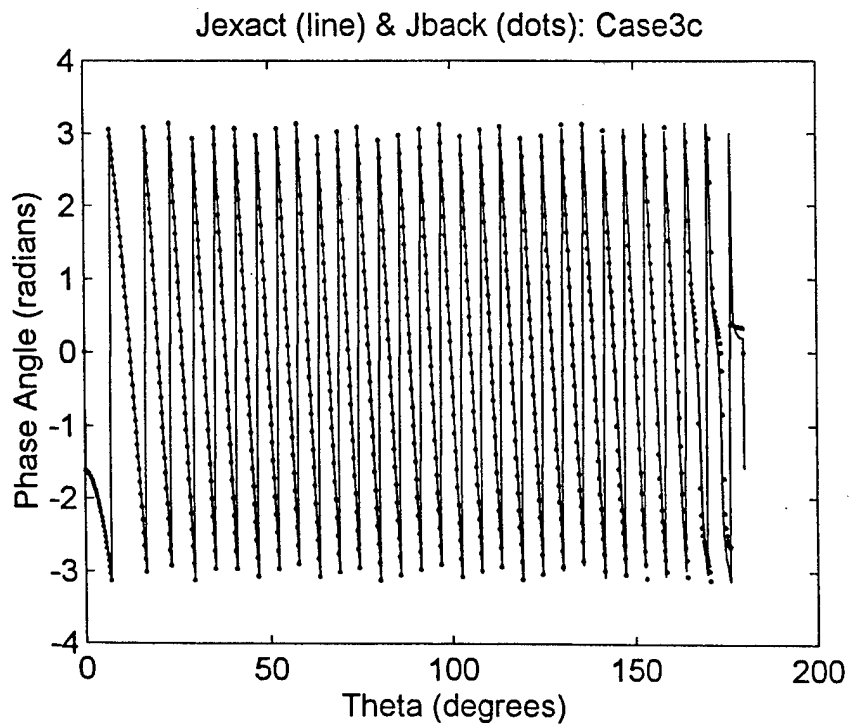


Figure 77. Phase Comparison: Case3c

IV. ANALYSIS OF RESULTS

A. THE INTEGRATION ALGORITHM

Since the "measured" fields to be back-propagated were to be determined through integration, the first part of this thesis was dedicated to generating accurate fields through numerical integration. As is shown in Table 1, properly performed numerical integration provides highly accurate measured fields. Figures 9 through 12 provide several examples of how quickly the integration converges. In each case the percent RMS error is determined essentially by the number of points on the sphere surface over which the integration takes place. For the cases included in this thesis the number of points was chosen such that the error due to back-propagation, as determined by the transfer matrix, would be kept below one percent.

Figures 13 through 30 show the magnitude and phase of the measured field determined through numerical integration. For each figure the measured field is over-laid on the exact field. Visual inspection indicates the magnitudes are nearly the same over the entire range of theta. RMS error computations indicate a difference of only a few hundredths of one percent. Visual inspection of the phase comparison gives similar results - both the computed and the exact are nearly the same.

As the number of surface points increase for a constant sphere size, the accuracy of the measured \overline{H} field increases. This result takes the form of decreasing RMS error as shown in the integration convergence of Figures 9 through 12. As the measurement distance increases for a constant sphere size, the number of points required for accurate integration results decreases. This can be seen by comparing Cases 2a and 2b shown in

Figures 11 and 12. For the larger measurement distance of Case 2b the RMS error is significantly smaller using the same number of points as Case2a.

B. FINITE ELEMENT METHOD PROBLEMS

The finite element method was used successfully to determine the source current on the PEC sphere when the field was measured at distances less than 0.25 wavelengths from the sphere surface. Table 2 summarizes the test cases used in this thesis.

The large errors that arise when the field to be back-propagated was measured at distances greater than 0.25 wavelengths from the sphere surface appear to be caused by resonant modes. These modes are shown for several cases in Figures 48, 50, 52 and 53. When back-propagated, these modes provide overwhelmingly disproportionate contributions at the sphere surface. These contributions are shown for a few representative cases in Figures 55, 56, and 57. It appears these resonant modes come about as a result of the boundary conditions placed on the outer boundary, the location at which the field is measured. As can be seen in Figures 48, 50, 51 and 53, these resonant modes appear as sharp spikes in the plot.

C. TRANSFER MATRIX

The transfer matrix that was used to determine the source current on the body gave results with less than one percent RMS error. The low error is a result of the number of surface points used to determine the measured field, and the number of points at which the field was measured at the outer boundary. The relationship between number of surface points and numerical integration accuracy was discussed in Section A. As can be seen in Equation (18), the measured field varies inversely with distance from segment to

field point. This inverse distance variation is the main point of concern when R is small at the closest point of approach. There is a large relative contribution to the integration from this surface region and the variation in the field is rapid. The number of segments on the sphere surface in this near-region must be increased to ensure the accuracy of numerical integration.

V. CONCLUSIONS

The objective of this research was to investigate the viability of back-propagating electromagnetic field measurements to an axisymmetric body in order to determine the source distribution for radiated power from the body. The method for achieving this objective was straightforward. First, the "measured fields" were simulated through numerical integration. Second, these fields were input into a finite element algorithm to determine the source current on a PEC axisymmetric body. The original thrust of the thesis was to investigate the ranges and resolution at which the fields could be measured in order to provide a usable level of accuracy in determining the source distribution on the body. The test cases were to include various "arbitrary" axisymmetric shapes to include cones, offset cones, offset spheres, and various cone-cylinder-sphere combinations. The centered sphere was to be used for very basic test purposes only.

Along the way to the objective it was found that the finite element method provided inaccurate results in the centered sphere tests for all but very limited cases. This discovery prompted a redirection of efforts to investigate the sources of error. Consequently, progress towards the original goals was sidetracked; but, that is often the nature of true research into the unknown.

The integration program developed to determine the measured fields was found to converge to an accurate solution. Although the shape tested was a sphere, the theory developed in Chapter II using stacked circular rings can be easily extended to arbitrary axisymmetric shapes.

The finite element method was selected as a means to determine the source current on the sphere through back-propagation. The errors associated with this method for the

centered sphere were unexpected. Consequently, solving these associated resonance problems was not intended to be the focus of this thesis. Further testing of the FEM solution will be done as part of extensions to this effort in follow-on thesis efforts and techniques for mitigating resonance effects will be explored.

REFERENCES

- [1] Bahret, W. F., "The Beginnings of Stealth Technology," *IEEE Transactions on Aerospace and Electronic Systems*, vol. 29, issue 4, October 1993, p. 1377-85.
- [2] Fulghum, D. A., "F-117A pilots, Generals Tell Congress About Stealth's Value in Gulf War," *Aviation Week and Space Technology*, vol. 134, no. 18, May 1991, p.66.
- [3] McPoyle, K. W., "Flexibility of Attack Aircraft Crucial To Crushing Iraq's Military Machine," *Aviation Week and Space Technology*, vol. 134, No. 16, April 1991, p.46.
- [4] Opall, B., "Air Force Sticks by its Stealth Plans," *Defense News*, 1 April 1996, The Time Journal Company.
- [5] Scott, W. B., "UWB Radar Has Potential to Detect Stealth Aircraft," *Aviation Week and Space Technology*, vol. 131, No. 23, 4 December 1989, p.38.
- [6] Sweetman, B., "Assessing Stealth Countermeasures," *International Defense Review*, Vol. 27, No. 3, 1 March 1994, p.38.
- [7] Williams, E. G., "Supersonic Acoustic Intensity," *J. Acoust. Soc. Am.* 97,121-127 (1995).
- [8] Williams, E. G., "Imaging the Sources on a Cylindrical Shell from Farfield Pressure Measured on a Semicircle," Naval Research Laboratory, Washington, D.C., August 1995.
- [9] Morgan, M. A., "EM Radiation Source Imaging Using Superluminal Cylindrical Modes," In preparation.
- [11] Balanis, C. A., *Advanced Engineering Electromagnetics*, John Wiley & Sons, New York, 1989.
- [10] Sadiku, M. N. O., *Elements of Electromagnetics*, Saunders College Publishing, Philadelphia, 1994.
- [12] Morgan, M. A., "Finite Element Formulation: Axisymmetric Fields," Notes of 7 April 97.
- [13] Morgan, M. A., "Variational Euler-Lagrange Algorithm," Notes of 16 April 97.
- [14] Morgan, M. A., "Solution for Transfer Array Using Spherical Harmonics for Centered Sphere," Notes of 2 May 97.

APPENDIX - MATLAB CODES

```
% thesis2.M by Dan Wawrzyniak 5/10/97
% updated 5/14/97
% Combines all programs into one
% Includes checking integration error first
% Allows user to save data in a .mat file for future use
clear all;
case = input('What case are you running? ','s');
f0 = input('Enter frequency in MHz: ');
lambda = 3e2/f0;
disp(['Wavelength = ',num2str(lambda),' meters']);
a1 = input('Enter metal sphere radius in terms of wavelength: '); a = a1*lambda;
r1 = input('Enter outer boundary in terms of wavelength: '); r = r1*lambda;
eta = 120*pi; % free-space Z_0
Idl = 1; % dipole moment
B = 2*pi/lambda; % wavenumber
z01 = input('Enter z-position of elemental dipole in terms of wavelength: ');
z0 = z01*lambda;
Nth1 = input('Enter number of theta points: '); Nth = Nth1-1;
ppwl = input('Enter number points per wavelength: ');
dth=pi/Nth; th=(0:dth:pi); thdeg=180*th/pi;
sth=sin(th); cth=cos(th);
% computing rd, sin(thd), and cos(thd) for sphere surface (r=a)
rd=sqrt(a*a+z0*z0-2*a*z0*cth); sthd=a*sth./rd; cthd=(a*cth-z0)./rd;
% computing field components in dipole centered coordinates
Fth=Idl*exp(-j*B*rd)./(4*pi*rd);
Hpi=Fth.*sthd.*(j*B + 1./rd);
Etd=eta*Fth.*sthd.*(j*B + 1./rd - j./(B*rd.*rd));
Erd=2*eta*Fth.*cthd.*(1./rd - j./(B*rd.*rd));
% translating incident field spherical components
cdth=cth.*cthd + sth.*sthd; sdth=sth.*cthd - cth.*sthd;
Eti=Etd.*cdth - Erd.*sdth; % note that Hpi=Hpd
% Computing spherical harmonic coefficients for scattered field
% Ets expansion which minimizes the total sphere surface
% tangential field = Eti+Ets
Nmax = fix(2*B*r);
disp(['Nmax = ',num2str(Nmax)]);
N = input('Enter number of spherical harmonics: ');
Sn=-dth*Eti.*sth; Pn1=legpol2(cth,N); In=(Pn1.)*Sn;
n=(1:N)'; cn=(2*n+1)./(2*n.*(n+1));
Ba=B*a; [Hn,DHn]=shan3(Ba,N);
Hn = Hn.'; DHn = DHn.';
Dn=DHn/Ba; an=(cn.*In)./(j*eta*Dn);
Ets=j*eta*Pn1*(an.*DHn)/Ba; Ett=Eti+Ets; % ideally Ett --> 0
```

```

Hps=Pn1*(an.*Hn)/Ba; Hpt=Hpi+Hps;      % Jtheta=H_pt
Jtheta = -Hpt;
Br=B*r; [Hn,DHn]=shan3(Br,N);
Hn = Hn.'; DHn = DHn.';
Ets=j*eta*Pn1*(an.*DHn)/Br; Hps=Pn1*(an.*Hn)/Br;
    numring = Nth; % number of rings
    inc = input('Enter number of face segments: ');
    ppoints = input('Enter phipoints - wavelength factor: ');
% Field Point Inputs
    % Input the Field Point in terms of theta.
    radius = r; % radius of field point
    numFP = length(Hps);
    thetaFP = linspace(0,pi,numFP);
    thetaFPd = 180*thetaFP/pi;
    rho = radius.*sin(thetaFP);
    z = radius.*cos(thetaFP);
% It is the tangential surface current at the nodes.
% The nodes are defined by rhop & zp.
    Jt = Jtheta;
% Determine the thetas for the sphere
    dtheta = pi/numring; % gives the delta theta
    theta = 0:dtheta:pi; % gives numring +1 values of theta.
    thetad = theta.*180/pi; % theta in degrees
% Determine (rhoprime,zprime) pairs on the sphere
    rhop = a*sin(theta);
    zp = a*cos(theta);
% Find the length "s" of each face.
    s = sqrt(rhop(2)^2 + (zp(1)-zp(2))^2);
% Find the angle associated with each face
    alpha = acos(rhop(2)/s) + theta(1:numring); % radians
    alphad = alpha*180/pi; % degrees
    talpha = tan(alpha);
    alpha1 = ones(inc+1,1)*alpha;
    alpha = reshape(alpha1,numring*(inc+1),1);
    dzf = (zp(1:numring)-zp(2:numring+1))/inc;
    phipoints = round(pi.*a*ppoints/lambda)+1;
    dphi = pi./phipoints;
    phi = 0:dphi:pi;
    cp = cos(phi);
for n = 1:numring; % loops through rings
    zf(:,n) = (zp(n):-dzf(n):zp(n+1)).';
    rhof(:,n) = (linspace(rhop(n),rhop(n+1),inc+1)).';
    JT(:,n) = Jt(n)*(zf(1:inc+1,n)-zp(n+1))/(zp(n)-zp(n+1))+...
        Jt(n+1)*(zf(1:inc+1,n)-zp(n))/(zp(n+1)-zp(n));
end

```

```

% Reshape the matrices to column vectors
zf = reshape(zf,numring*(inc+1),1);
rhof = reshape(rhof,numring*(inc+1),1);
JT = reshape(JT,numring*(inc+1),1);
for FP = 1:numFP; % loops through field points
    R1 = 2*rho(FP)*rhof*cp;
    R2 = (rho(FP)^2+rhof.^2+(z(FP)-zf).^2)*ones(1,length(cp));
    R = sqrt(R2-R1);
    [Fcs,F1s] = fcsfls2(cp,dphi,R);
    Ha = rhof.*sin(alpha);
    Hb = (z(FP) - zf).*cos(alpha);
    Hc = (Ha-Hb).*Fcs;
    Hd = rho(FP).*sin(alpha).*F1s;
    H = (Hc-Hd).*JT;
    H = reshape(H,inc+1,numring);
    H1 = a*((1/(4*pi))*(trapz(H)));
    H1 = dzf.*H1;
    HH(1:numring,FP) = H1.';
end
Hphi = sum(HH);
%% RMS Error Calculations
E = 100*sqrt((Hps - Hphi.').*(Hps - Hphi.'))./sqrt(Hps'*Hps);
figure
plot(thdeg,abs(Hphi),'ko',thdeg,abs(Hps),'k')
title(['Hps (exact: -, integrated: o): ',eval('case'),', RMS Error= ',num2str(E),'%'])
xlabel('Theta (degrees)');
ylabel('|Hscattered|');
figure
plot(thdeg,real(Hphi),'k*',thdeg,imag(Hphi),'k+',thdeg,real(Hps),...
    'k',thdeg,imag(Hps),'ko');
title(['Hexact(real: -, imag: o) & Hint(real: *, imag: +): ',eval('case')])
xlabel('Theta (degrees)')
ylabel('Hps (Amps/meter)')
%text(.55,.95,['Frequency= ',num2str(f0),'Mhz'],'color',...
% 'g','units','normalized');
%text(.55,.90,['Wavelength= ',num2str(lambda),'meters'],'color',...
% 'g','units','normalized');
%text(.55,.85,['Dipole Offset= ',num2str(z01),'*lambda'],'color',...
% 'g','units','normalized');
%text(.55,.80,['Radius of Sphere= ',num2str(a1),'*lambda'],'color',...
% 'g','units','normalized');
%text(.55,.75,['Radius of Field Point= ',num2str(r1),'*lambda'],'color',...
% 'g','units','normalized');
%text(.55,.70,['Number Rings= ',num2str(numring)],'color',...
% 'g','units','normalized');

```

```

%text(.55,.65,['Face Segments= ',num2str(inc)],'color',...
% 'g','units','normalized');
%text(.55,.60,['Phi-Wavelength Factor= ',num2str(ppoints)],'color',...
% 'g','units','normalized');
%text(.55,.55,['Field Points= ',num2str(numFP)],'color',...
% 'g','units','normalized');
%text(.55,.50,['Field Points per wl= ',num2str(ppwl)],'color',...
% 'g','units','normalized');
%text(.55,.45,['Number modes= ',num2str(N)],'color',...
% 'g','units','normalized');
%text(.55,.40,['RMS Error= ',num2str(E),' %'],'color',...
% 'r','units','normalized');
%%%%%%%%%%%%%%%%%%%%%%%%%%%%%%%%%%%%%%%%%%%%%%%%%%%%%%%%%%%%%%%%%%%%%%%%
% Computes Hphi incident at the field point radius due to the dipole.
% This result is added to the Hphi scattered computed using Dan's
% integration program
dth=pi/Nth; th=(0:dth:pi)'; thdeg=180*th/pi;
sth=sin(th); cth=cos(th);
% computing rd, sin(thd), and cos(thd) for sphere surface (r=a)
rd=sqrt(r*r+z0*z0-2*r*z0*cth); sthd=r*sth./rd; cthd=(r*cth-z0)./rd;
% computing field components in dipole centered coordinates
Fth=Idl*exp(-j*B*rd)/(4*pi*rd);
Hpi=Fth.*sthd.*(j*B + 1./rd);
    Hphi = Hphi.'; % make Hphi a column vector
%%%%%%%%%%%%%%%%%%%%%%%%%%%%%%%%%%%%%%%%%%%%%%%%%%%%%%%%%%%%%%%%%%%%%%%%
% This program loads the transfer function Hs from femdat.mat
% and created by FEM2.M and dots it with Hphi stored in
% source.mat from Dan's integration program SOURCE.M.
%
% The result is the current on the surface of the sphere
% arrived at through the back propagation of the scattered
% H field.
%
% The result (Jback) is compared to the surface current used in
% Dan's program (Jtheta, stored in jtheta.mat).
%
% The surface current is generated by DIPSPHR2.M
%
load femdat.mat
% Add Hphi scattered from sphere and Hpi incident from dipole
    Hphitot = -(Hphi + Hpi);
% Determine Surface current due to back-propagation of Hphi
% Hphi is UNFILTERED
    Jback = Hs*Hphitot;
% Determine Surface current due to back-propagation of Hphi

```

```

% RMS Error Calculations
E = 100*sqrt((Jtheta - Jback)*(Jtheta - Jback))./sqrt(Jtheta'*Jtheta);
figure
plot(thdeg,abs(Jtheta),'k',thdeg,abs(Jback),'ko')
title(['Jexact (-) & Jback (o): ',eval('case'),' ', RMS Error= ',...
      num2str(E),'%'])
xlabel('Theta (degrees)')
ylabel('Jtheta')
%legend('Jtheta - dipsphr2.m','Jback: no filtering - fem2.m')
figure
plot(thdeg,real(Jtheta),'k',thdeg,imag(Jtheta),'ko',thdeg,real(Jback),...
      'k*',thdeg,imag(Jback),'k+')
title(['Jexact(real: -, imag: o) & Jback(real: *, imag: +): ',eval('case')]);
xlabel('Theta (degrees)')
ylabel('Jtheta (Amps/m*m)')
yn = input('Save data from this run? (Y/N): ','s');
if ~isempty(yn)
    if yn == 'y' | yn == 'Y'
        clear eta Idl B a z0 dth th sth cth rd sthd cthd Fth Etd Erd cdth sdth ...
            Eti r Sn Pn1 In n cn Ba Hn DHn Ets Br Dn Ett F1s FP Fcs E
        clear H H1 HH Ha Hb Hc Hd JT Jt R R1 R2 alpha alpha1 alphad an cp dphi...
            dtheta dzf rb fho rhof rhop rs s talpha yn z zb zf zp zs
        clear Hpt Nmax Nth f phi phipoints...
            radius rho theta thetaFP thetaFPd thetad
        save (eval('case'))
    %save f0 lambda a1 z01 r1 Nth N inc ppoints Hs Hps numring ppoints numFP...
    % ppwl name thdeg Hps Jback Hphi Hphitot
end
end

```



```

function [Fc_s,F1_s] = fcsf1s2(cp,dphi,R)
% For use with HPHIERR2.M
%
% This function does the integration to find Fc(s) & F1(s)
% updated 4/19/79 at home Dan Wawrzyniak
lambda = 1;
beta = 2*pi/lambda;
phase = exp(-i*beta.*R);
same = (1+i*beta.*R)./R.^3;
F1 = same.*phase;
F1_s = (2*dphi*(trapz(F1.'))).';
Fc = ones(size(F1_s))*cp.*same.*phase;
Fc_s = (2*dphi*(trapz(Fc.'))).';

```

```

% DipSpr2.M computes scattered fields due to an elemental z-axis
% dipole positioned above the north pole of a metallic sphere.
% Mod-2 by M.A. Morgan 3/14/97
% shan3.m & legpol2.m loaded 5/2/97
clear all;
eta=120*pi; % free-space Z_0
Idl=1; % dipole moment
f0=300; % 300 MHz
B=2*pi*f0/300; % wavenumber
z0=input('Enter z-position of elemental dipole in meters: ');
a=input('Enter metal sphere radius in meters: ');
Nth=input('Enter number of theta segments: ');
dth=pi/Nth; th=(0:dth:pi); thdeg=180*th/pi;
sth=sin(th); cth=cos(th);
% computing rd, sin(thd), and cos(thd) for sphere surface (r=a)
rd=sqrt(a*a+z0*z0-2*a*z0*cth); sthd=a*sth./rd; cthd=(a*cth-z0)./rd;
% computing field components in dipole centered coordinates
Fth=Idl*exp(-j*B*rd)/(4*pi*rd);
Hpi=Fth.*sthd.*(j*B + 1./rd);
Etd=eta*Fth.*sthd.*(j*B + 1./rd - j./(B*rd.*rd));
Erd=2*eta*Fth.*cthd.*(1./rd - j./(B*rd.*rd));
% translating incident field spherical components
cdth=cth.*cthd + sth.*sthd; sdth=sth.*cthd - cth.*sthd;
Eti=Etd.*cdth - Erd.*sdth; % note that Hpi=Hpd
% Computing spherical harmonic coefficients for scattered field
% Ets expansion which minimizes the total sphere surface
% tangential field = Eti+Ets
N=input('Enter number of spherical harmonics: ');
Sn=-dth*Eti.*sth; Pn1=legpol2(cth,N); In=(Pn1.)*Sn;
n=(1:N); cn=(2*n+1)/(2*n.*(n+1));
Ba=B*a; [Hn,DHn]=shan3(Ba,N);
Hn = Hn.'; DHn = DHn.';
Dn=DHn/Ba; an=(cn.*In)/(j*eta*Dn);
Ets=j*eta*Pn1*(an.*DHn)/Ba; Ett=Eti+Ets; % ideally Ett --> 0
Hps=Pn1*(an.*Hn)/Ba; Hpt=Hpi+Hps; % Jtheta=H_pt
Jtheta = -Hpt;
save dipsphr2 Jtheta thdeg
% Plotting expansions on sphere surface
clf reset; plot(thdeg,abs(Eti),thdeg,abs(Ett),'');
xlabel('theta (deg)');
ylabel('|E_theta|: Incident (solid); Total (dots)');
title(['Dipole at z0=',num2str(z0),', Sphere Radius=',num2str(a),...
', No. Modes=',int2str(N)]);
figure(1);
hcpy=input('Enter 1 for Hard Copy: ');

```

```

if hcpy == 1, print; end;
clf reset; plot(thdeg,abs(Hpi),thdeg,abs(Hps),'.',thdeg,abs(Hpt),'--');
xlabel('theta (deg)');
ylabel('|H_phi|: Incident (solid); Scattered (dots); Total (dashed)');
title(['Dipole at z0=',num2str(z0),'; Sphere Radius=',num2str(a),...
'; No. Modes=',int2str(N)]);
figure(1);
hcpy=input('Enter 1 for Hard Copy: ');
if hcpy == 1, print; end;
% Now compute scattered fields at specified radius
r=input('Enter radius in meters to field point: ');
Br=B*r; [Hn,DHn]=shan3(Br,N);
Hn = Hn.'; DHn = DHn.';
Ets=j*eta*Pn1*(an.*DHn)/Br; Hps=Pn1*(an.*Hn)/Br;
% Plotting scattered field expansions
clf reset; plot(thdeg,abs(Ets),thdeg,eta*abs(Hps),'.');
xlabel('theta (deg)');
ylabel('|E_theta| (solid); eta*|H_phi| (dots)');
title(['Scattered Fields at r=',num2str(r), ' m; Dipole at z0=',...
num2str(z0),'; Sphere Radius=',num2str(a),'; No. Modes=',int2str(N)]);
figure(1);
hcpy=input('Enter 1 for Hard Copy: ');
if hcpy == 1, print; end;
end;

```

```

% FEM2.M provides finite-element solution for user-specified
% metallic body of revolution using VARELA algorithm.
% By M.A. Morgan 3/20/97- 4/17/97
clear all
% Generating surface and boundary points then mesh topology
sgen=input('Enter name of surface generation program: ','s');
eval(['[rs zs rb zb]=',sgen,'];');
[rho zee nd elnd]=mesh2(rs,zs,rb,zb); % Computing mesh
% Computing Mesh Parameters
N=length(rho);      % Number of Nodes in Mesh
L=length(elnd(:,1)); % Number of Elements in Mesh
Ns=length(nd);      % No. of Surface or Boundary Nodes
Nm=N-nd(1)-nd(Ns)-Ns+2; % Number of Nodes for Unknown Hphi
disp(' ')
disp('Finite Element Mesh Parameters: ')
disp([' Number of Nodes: ',int2str(N)])
disp([' Number of Elements: ',int2str(L)])
disp([' Number of Unknowns: ',int2str(Nm)])
disp(' ')
disp('Press a Key to Display Mesh or <Ctl> C to Abort');
pause
% Plotting Mesh Nodes and Elements
%clf reset
figure('PaperPosition',[1.5 0.5 5 3.75])
if Ns <=19, plot(rho,zee,'go');
    else, plot(rho,zee,'k. '); end
hold on
for l=1:L
    nds=elnd(l,:);
    rl=[rho(nds); rho(nds(1))]; zl=[zee(nds); zee(nds(1))];
    plot(rl,zl,'k');
end
v=axis; v(1)=0; v(2)=v(4)-v(3); axis(v); axis square;
title('2-D Axisymmetric Shape with mesh')
xlabel('meters')
ylabel('meters')
text(2.7*v(2)/5,5*v(4)/6,'Mesh Parameters: ')
text(3*v(2)/5,3*v(4)/4,['Nodes: ',int2str(N)])
text(3*v(2)/5,2*v(4)/3,['Elements: ',int2str(L)])
text(3*v(2)/5,7*v(4)/12,['Unknowns: ',int2str(Nm)])
yn=input('Print Hard Copy ? (Y/N): ','s');
if ~isempty(yn), if yn == 'y' | yn == 'Y', print; end; end
% Loading System Matrices By Indexing Through Elements
disp('Sparse Matrix Loading Using Element Contributions Can Now Begin')
f=input('Enter Frequency in MHz to Start Loading; <Ctl> C to Stop: ');

```

```

k2=(pi*f/150)^2; T=zeros(3,3);
A=sparse(Nm,Nm); B=sparse(Nm,Ns-2);
l2=0; nf=cumsum(nd); ns=nf-nd+1; % node finish/start per row
for i=2:Ns;
    l1=l2+1; l2=l1+nd(i)+nd(i-1)-3; % start/finish elements
    for l=l1:l2
        nds=elnd(l,:); rp=rho(nds); zp=zee(nds);
        T=varela(k2,rp,zp);
        disp(['Loading Element ',int2str(l),' of ',int2str(L)])
        % Loading sparse matrix contributions
        for m=1:3;
            ma=0;
            if nds(m) ~= nf(i-1) & nds(m) ~=nf(i), % m not on boundary
                if nds(m) > nf(i-1) & i < Ns,
                    ma=nds(m)-ns(2)-i+3; end
                if nds(m) < ns(i) & i > 2,
                    ma=nds(m)-ns(2)-i+4; end
            if ma > 0, % m is a solution node
                for n=1:3;
                    na=0;
                    if nds(n) ~= nf(i-1) & nds(n) ~=nf(i),
                        if nds(n) > nf(i-1) & i < Ns,
                            na=nds(n)-ns(2)-i+3; end
                        if nds(n) < ns(i) & i > 2,
                            na=nds(n)-ns(2)-i+4; end
                    if na > 0,
                        A(ma,na)= A(ma,na)+T(m,n); end
                    end % n not on boundary end
                    if nds(n) == nf(i-1) & i > 2,
                        B(ma,i-2)=B(ma,i-2)-T(m,n); end
                    if nds(n) == nf(i) & i < Ns,
                        B(ma,i-1)=B(ma,i-1)-T(m,n); end
                    end % n-loop end
                end % ma > 0 end
            end % m not on boundary end
        end % m-loop end
    end % l-loop end
end % i-loop end
disp('Matrices Loaded, Now Solving System ... Be Patient')
% Solve sparse matrix system to construct transfer function
% array relating internal Hphi to Ns-2 nodal boundary values
H = A\B; % clear A B C D % freeing memory
% Extract rows to form transfer array relating Ns nodal values
% of Hphi (including two z-axis Hphi=0 BC's) to Ns nodal values
% of Hphi on the PEC surface. Note that the PEC surface output

```

```

% column vector has Hphi(1)=Hphi(Ns)=0 since these correspond
% to nodes on the z-axis.
Hs=zeros(Ns,Ns);
row=1; Hs(2,2:Ns-1) = H(row,:);
for n=3:Ns-1;
    row=row+nd(n-1)-1; Hs(n,2:Ns-1) = H(row,:);
end
n=1:Ns; clf; plot(n,diag(Hs),'r')
v=axis; axis([1 Ns v(3) v(4)])
xlabel('row(n)'); ylabel('Real diag[Hs]')
title(['Diag[Hs] for ',sgen,', Ns=',int2str(Ns),', N=',int2str(N),...
    ', Nm=',int2str(Nm),', L=',int2str(L)]); figure(1)
yn=input('Print Hard Copy ? (Y/N): ','s');
if ~isempty(yn), if yn == 'y' | yn == 'Y', print; end; end
% Saving Needed Parameters and Hs Transfer Function Array
save femdat f rs zs rb zb Hs

```

```

% Program FEMCHK4.M compares exact and FEM2.M computed
% nodal values for spherical harmonic single mode solutions
% of an offset metal sphere. By M.A. Morgan 4/21/97
% Mod-2a (4/30/97) uses MatLab Bessel and Hankel Functions in shan3.m
% Mod-3 (5/2/97) uses Wronskian to simplify  $r=a$  "exact" solution
% and computes and plots errors for applied modes
% Mod-4 (5/3/97) uses real mode BC's  $P_n^1(\cos(\theta))$  on  $r=b$ 
% which produces a real internal solution
clear all;
case = input('What case are you running? ','s');
load femdat; % loading f rs zs rb zb Hs
k=pi*f/150; Ns=length(rs);
d=(zs(1)+zs(Ns))/2 - (zb(1)+zb(Ns))/2; % computing offset
a=zs(1)-d; b=zb(1); Ra=k*a; Rb=k*b; % reset sphere centers
zbd=zb-d; r_b=sqrt(rb.^2+zbd.^2); b=zb(1);
th=linspace(0,pi,Ns)'; c_a=cos(th); th_a=linspace(0,180,Ns)';
c_b=zbd./r_b; th_b=180*acos(c_b)/pi;
N=input('Enter Upper Spherical Harmonic Mode to Check: ');
[hna,Dhna]=shan3(Ra,N); [hnb,Dhnb]=shan3(Rb,N);
DJna=real(Dhna); Jnb=real(hnb);
DNna=-imag(Dhna); Nnb=-imag(hnb);
Dn=(Jnb.*DNna-DJna.*Nnb); An=ones(Ns,1)*DNna; Bn=ones(Ns,1)*DJna;
[Hn,DHn]=shan3(k*r_b,N); Jn=real(Hn); Nn=-imag(Hn);
pna=legpol2(c_a,N); pnb=legpol2(c_b,N); pct=zeros(N,1);
Ha=b*pna./(a*ones(Ns,1)*Dn); % "exact"  $r=a$ 
Hb=b*pnb.*(An.*Jn-Bn.*Nn)./(r_b*Dn); % "exact"  $r=b$ 
Hc=Hs*Hb; % Computed solution on  $r=a$ 
for n=1:N;
pct(n)=100*sqrt((Ha(:,n)-Hc(:,n))*(Ha(:,n)-Hc(:,n)))/...
sqrt(Ha(:,n)*Ha(:,n)));
end
[tseg1,tseg2] = size(Hs);
figure('PaperPosition',[1.5 0.5 5 3.75])
bar(1:N,pct,'k'), v=axis; v(1)=0; v(2)=N+1; v(3)=0; axis(v);
xlabel('Mode Index "n"'); ylabel('Percent');
title(['Single Mode RMS Error for Centered PEC Sphere: ',eval('case')])
yn=input('Print Hard Copy ? (Y/N): ','s');
if ~isempty(yn), if yn == 'y' | yn == 'Y', print; end; end
while 1,
n=input(['Enter n <= ',int2str(N),...
' for Spherical Harmonic (0 to stop): ']);
if isempty(n), break;
elseif n == 0, break;
elseif n > N, disp('n exceeds N'); break; end
figure('PaperPosition',[1.5 0.5 5 3.75])

```

```

plot(th_b,Hb(:,n),'k')
xlabel('Theta (deg)'); ylabel('Hphi (A/m)');
title(['Single Mode Hphi at Outer Boundary: ',eval('case'),...
      ', n=',int2str(n)]);
v=axis; axis([0 180 v(3) v(4)]);
yn=input('Print Hard Copy ? (Y/N): ','s');
if ~isempty(yn), if yn == 'y' | yn == 'Y', print; end; end
if length(th_a) < 38,
figure('PaperPosition',[1.5 0.5 5 3.75])
plot(th_a,Ha(:,n),'k',th_a,Hc(:,n),'k.')
title(['Exact (line), FEM (dots): ',eval('case'),...
      ', n=',int2str(n),', RMS Error=',num2str(pct(n)), '%']);
else,
figure('PaperPosition',[1.5 0.5 5 3.75])
plot(th_a,Ha(:,n),'k',th_a,Hc(:,n),'k.');
title(['Exact (line), FEM (dots): ',eval('case'),...
      ', n=',int2str(n),', RMS Error=',num2str(pct(n)), '%']);
end
xlabel('Theta (deg)'); ylabel('Hphi (A/m)');
v=axis; axis([0 180 v(3) v(4)]);
yn=input('Print Hard Copy ? (Y/N): ','s');
if ~isempty(yn), if yn == 'y' | yn == 'Y', print; end; end
end

```



```

% hsphere1.m
% Program Hsphere.M uses spherical harmonics to compute
% the Hs array for a centered PEC sphere. Saves in same
% format as FEM2.m and can be used in FEMCHKxx.m programs
% By M.A. Morgan 5/2/97
% 5/10/97 modified by Dan Wawrzyniak
% Nmax = 2*k*b
clear all
f=input('Enter frequency in MHz: '); k=pi*f/150; lambda = 3e2/f;
a=input('Enter metal sphere radius "a" in meters: ');
b=input('Enter outer mesh radius "b" in meters: ');
Ns1=input('Enter number of theta points per wavelength: ');
Ns = fix(pi*b*Ns1/lambda);
disp(['Total theta points = ',int2str(Ns)])
th=linspace(0,pi,Ns); thd=linspace(0,180,Ns); dth12=pi/(12*(Ns-1));
Ra=k*a; Rb=k*b; cth=cos(th); sth=sin(th); Nmax=2*fix(Rb);
disp(' '); disp(['Estimated Nmax=integer[2*k*b] is ',int2str(Nmax)])
N=input('Enter Upper Mode Order to Use in Computing Hs: ');
disp(' ')
[Hna,DHna]=shan3(Ra,N); [Hnb,DHnb]=shan3(Rb,N);
Pn1=legpol2(cth,N); n=1:N; Cn=(2*n+1)/(2*n.*(n+1));
Qn=(b/a)/(real(DHna).*imag(Hnb)-real(Hnb).*imag(DHna));
n=1:N; A=zeros(N,Ns); Hs=zeros(Ns,Ns);
% Numerical integration of up(th)*Pn1(cth)*sth
for p=2:Ns-1;
fn=Pn1(p-1:p+1,:); g=sth(p-1:p+1);
Inp=dth12*(fn(1,:)*g(1)+6*fn(2,:)*g(2)+fn(3,:)*g(3)+...
fn(1,:)*g(2)+fn(2,:)*g(1)+fn(2,:)*g(3)+fn(3,:)*g(2));
A(:,p)=(Cn.*Qn.*Inp).';
end
Hs=Pn1*A;
n=1:Ns; clf; plot(n,diag(Hs),'r')
v=axis; axis([1 Ns v(3) v(4)])
xlabel('row(n)'); ylabel('Real Hs Diagonal')
title(['Diag[Hs] using Hsphere.m for Ns=',int2str(Ns),...
'; Nmax=',int2str(N),]);
figure(1)
yn=input('Print Hard Copy ? (Y/N): ','s');
if ~isempty(yn), if yn == 'y' | yn == 'Y', print; end; end
rs=a*sth'; zs=a*cth'; rb=b*sth'; zb=b*cth';
% Saving Needed Parameters and Hs Transfer Function Array
save femdat f rs zs rb zb Hs

```

```

function [Hn,DHn] = shan3(X,N)
% Riccati Spherical Hankel Function  $H_n^{(2)}(X) = J_n(X) - jY_n(X)$ 
% and Derivative. Using MatLab cylindrical functions of order  $n+1/2$ .
% Function returns:  $H_n(n)=H_n^{(2)}(x)$  and  $DH_n(n)=dH_n^{(2)}(x)/dx$ 
% for  $n=1$  to  $N$ . Input  $N$  is a positive integer.  $X$  is an array
% of real or complex values  $[x_1 \ x_2 \ \dots \ x_M]$ . Output  $H_n(x_m)$  and
%  $DH_n(x_m)$  are  $M$  by  $N$  complex arrays. By M.A. Morgan.
% Mod-3 (5/1/97) allows  $X$  to be either row or column array.
[m1 m2]=size(X); M=max(m1,m2); Hn=zeros(M,N); DHn=Hn;
if m1==1, x=X'; else, x=X; end
Nu=(1:N)+0.5; xn=x*ones(1,N);
J0=sqrt(pi*x/2).*besselj(0.5,x);
Jn=sqrt(pi*xn/2).*besselj(Nu,x);
N0=sqrt(pi*x/2).*bessely(0.5,x);
Nn=sqrt(pi*xn/2).*bessely(Nu,x);
Hn=Jn-j*Nn; H0=J0-j*N0; DHn(:,1)=H0-Hn(:,1)./x;
if N > 1, DHn(:,2)=Hn(:,1)-2*Hn(:,2)./x; end
if N > 2,
for n=3:N; DHn(:,n)=Hn(:,n-1)-n*Hn(:,n)./x; end
end

```

```

function Pn1 = legpol2(X,N)
% Computing a matrix of associated Legendre polynomials
%  $P_n^m(x)$  with  $m=1$ , for  $n=1, 2, \dots, N$  where  $N$  is a positive integer
% and  $X$  is an  $M$ -element array of real values  $[x_1 \ x_2 \ \dots \ x_M]$ .
% Computed real array  $Pn1(x_m)$  has  $M$  rows and  $N$  columns.
% Using upward recurrence formula from page 953 of Balanis -
% Advanced EM Engineering, Wiley, 1989. Program by M.A. Morgan
% Mod-2 (5/1/97) allows either row or column input  $X$  array
[m1 m2]=size(X); M=max(m1,m2); Pn1=zeros(M,N);
if m1==1, x=X'; else, x=X; end
Pn1=zeros(M,N); Pn1(:,1)=-sqrt(1-x.*x);
if N > 1, Pn1(:,2)=3*x.*Pn1(:,1); end
if N > 2,
for n=2:N-1;
n1=1/n; Pn1(:,n+1)=(2+n1)*x.*Pn1(:,n)-(1+n1)*Pn1(:,n-1);
end
end

```

```

function [rs,zs,rb,zb] = osphere
% Computing meridian surface coordinates for offset sphere
% (rs,zs) with a=radius and d=z-axis offset. Outer
% mesh boundary is centered b=radius sphere (rb,zb).
% Returning coordinates in Ns x 4 array.
% By M.A. Morgan 3/24/97
disp('Offset Sphere Surface and Mesh Boundary Program');
a=input('Enter sphere radius (meters): ');
d=input('Enter sphere offset (meters): ');
b=input('Enter mesh radius (meters): ');
Ns=input('Enter number of surface points: ');
tha=linspace(0,pi,Ns)'; sta=sin(tha); cta=cos(tha);
rs=a*sta; zs=a*cta+d;
thb=tha-asin(d*sin(pi-tha)/b); stb=sin(thb); ctb=cos(thb);
rb=b*stb; zb=b*ctb;
clf reset; plot(rs,zs,rs,zs,'g',rb,zb,rb,zb,'g')
v=axis; v(1)=0; v(2)=v(4)-v(3); axis(v); axis square;
xlabel('Press a Key to Display Mesh or <Ctrl> C to Abort')
figure(1)

```

```

function [rs,zs,rb,zb] = cone
% Computing meridian surface coordinates for centered cone
% (rs,zs) with h=height and b=base radius . Outer
% mesh boundary is centered a=radius sphere (rb,zb).
% Returning coordinates in Ns x 4 array.
% By M.A. Morgan 3/27/97
disp('Conical Surface and Spherical Mesh Boundary Program');
h=input('Enter cone height (meters): ');
b=input('Enter cone base radius (meters): ');
a=input('Enter outer mesh spherical radius (meters): ');
Ns=input('Enter number of surface points: ');
rs=zeros(Ns,1); zs=rs; th=rs;
S=b+sqrt(b*b+h*h); % total surface length on cone
Nb=fix(Ns*b/S)+1; if Nb>Ns-2, Nb=Ns-2; end; db=b/Nb; Nz=Ns-Nb;
rs(1:Nz)=linspace(0,b,Nz); zs(1:Nz)=linspace(h/2,-h/2,Nz);
rs(Nz+1:Ns)=linspace(b-db,0,Nb); zs(Nz+1:Ns)=(-h/2)*ones(Nb,1);
% distort boundary node positions to improve mesh near corner
a2=atan(h/b)/2; gm=a2+pi/2; c=(h/2)-b*tan(a2);
dl=asin(c*sin(gm)/a); thc=gm+dl; dtb=(pi-thc)/Nb;
th(1:Nz)=linspace(0,thc,Nz); th(Nz+1:Ns)=linspace(thc+dtb,pi,Nb);
st=sin(th); ct=cos(th); rb=a*st; zb=a*ct;
clf reset; plot(rs,zs,rs,zs,'r.','rb,zb,rb,zb','g.')
v=axis; v(1)=0; v(2)=v(4)-v(3); axis(v); axis square; figure(1)
xlabel('Press a Key to Display Mesh or <Ctrl> C to Abort')

```

INITIAL DISTRIBUTION LIST

1. Defense Technical Information Center.....2
8725 John J. Kingman Rd., STE 0944
Ft. Belvoir, VA 22060-6218

2. Dudley Knox Library.....2
Naval Postgraduate School
Monterey, CA 93943-5101

3. Director, Training and Education.....1
MCCDC, Code C46
1019 Elliot Road
Quantico, VA 22134-5027

4. Director, Marine Corps Research Center.....2
MCCDC, Code C40RC
2040 Broadway Street
Quantico, VA 22134-5107

5. Director, Studies and Analysis Division.....1
MCCDC, Code C45
3300 Russell Road
Quantico, VA 22134-5130

6. Marine Corps Tactical Systems Support Activity.....1
Technical Advisory Branch
Attn: Maj J.C. Cummiskey
Box 555171
Camp Pendleton, CA 92055-5080

7. Marine Corps Representative.....1
Naval Postgraduate School
Code 037, Bldg. 234, HA-220
699 Dyer Road
Monterey, CA 93940

8. Department Chairman, Code EC.....1
Naval Postgraduate School
833 Dyer Road, Rm. 433
Monterey, CA 93943-5121

9. Professor Michael A. Morgan, Code EC/Mw.....2
Naval Postgraduate School
833 Dyer Road, Rm. 433
Monterey, CA 93943-5121
10. Professor David C. Jenn, Code EC/Jn.....1
Naval Postgraduate School
833 Dyer Road, Rm. 433
Monterey, CA 93943-5121
11. Dr. Ronald Radlinski.....1
Ship Structures & Systems S&T Division, Code 334
Office of Naval Research, Balston Centre Tower One
800 North Quincy Street
Arlington, VA 22217-5660